POLITECNICO DI TORINO

Master's in Electronic Engineering

Masters's Degree Thesis

Modeling, design and fabrication of a surface acoustic waves based sensor for oral cancer detection

Supervisors

Prof. DEMARCHI DANILO

Ing. FERRARA FRANCESCO

Candidate

TRUCCO MATTIA

July 2020

Abstract

In this thesis a sensor based on Surface Acoustic Waves with a Molecularly Imprinted Polymer as sensing element is designed, fabricated and simulated. This work is part of the SMILE project on which STMicroelectronics works beside CNR Nanotec, whose aim is to develop a diagnostic platform able to analyze saliva sample in order to detect IL-10 molecules, a biomarker involved in the inflammatory processes of the Oral Squamous Cell Carcinoma. OSCC screening requires invasive and expensive methods that lead to a low amount of early diagnosed patients. The high influence of the diagnostic timing on the life quality of the patients makes the realization of a new detection system very attractive. STMicroelectronics and CNR Nanotec propose a diagnostic tool which combines SAW and MIP technologies, that can be compact, portable, easy of use and low cost. SAW delay lines are chosen among acoustic devices for their fast response and for the easiness to be integrated with receptor materials, that makes them suitable for biosensing applications. Design choices such as substrate material and orientation and transducers geometric parameters are made according to their influence towards device characteristics. The patterns to be transferred on the substrate surface are drew in CleWin, to be employed in the photolithographic process. The behaviour of the devices is investigated by implementing a mathematical model in Matlab, that allow to test the design parameters and to monitor the relative figures of merit. A Finite element modelling of the devices is performed in COMSOL, in order to obtain a model compliant with experimental data. Eigenfrequency, frequency domain and time domain analyis are carried out to characterize the model while different key parameters are varied within the simulations. Several settings and boundary conditions are investigated in order to obtain models whose behaviour is close as possible to the experimental one. The delay lines along with MIP structures are fabricated in clean room at CNR Nanotec facility. The metallic electrodes are obtained by means of a maskless photolithography and a subsequent metal deposition. MIP and NIP structures are formed on the surface of an electrode through a cyclic voltammetry process. The devices obtained through the fabrication processes are measured by a Vector Network Analyzer, that compute their transmission characteristics. The experimental results are then compared to the simulation outputs. In particular, the similarity level between real devices and FEM models is evaluated by comparing measured and simulated frequency responses.

Table of Contents

List of Figures

Chapter 1

Introduction

1.1 SAW history

Lord Rayleigh demonstrated the existence of the surface acoustic waves in anisotropic material in 1885. Today this kind of wave is named after him, the Rayleigh wave. It propagates along the plane surface, moving the particles in the sagittal plane, while decaying with depth. These waves were discovered by observing the seismic signals caused by earthquakes. Rayleigh understood that some late signals, which could also be relatively strong, could be explained by slower surface waves [1]. Later, other geophysicists worked on this subject. In particular in 1911, Augustus E. H. Love published a treatise that includes an investigation on the shear surface waves [2]. This wave, called Love wave, is characterized by having the particle motion perpendicular to the sagittal plane. It exists when the substrate is coated with a layer of lower bulk shear velocity material. The interest of electronics applications in surface waves is quite recent. It is during the World War II that it grew. The driving force was the radar technology, in which the SAW was used for the pulse compression. In this period much research was done. After the war this work was revealed by Klauder et al. [**3**] and the first SAW based pulse compression filter was presented by Tancrell et al. in 1969 [**4**]. Several type of acoustic waves and transducer wee investigated [3]. In 1963, Rowen and Mortley suggested the first planar SAW transducer, simplifying both its beahviour and its fabrication [4]. In 1965, White and Voltmer [5] demonstrated the generation and the reception of waves of an interdigital transducer (IDT), a structure made up of metal electrodes connected to bus bars in an alternated fashion on quartz substrate. Because of the IDT fabrication simplicity, its introduction was a key development for SAW technology. Since the solutions depend on the material and on its orientation, many papers about SAW propagation in anisotropic material have been published.
In 1968, Campbell et al. [6] showed a numerical method to find SAW solutions

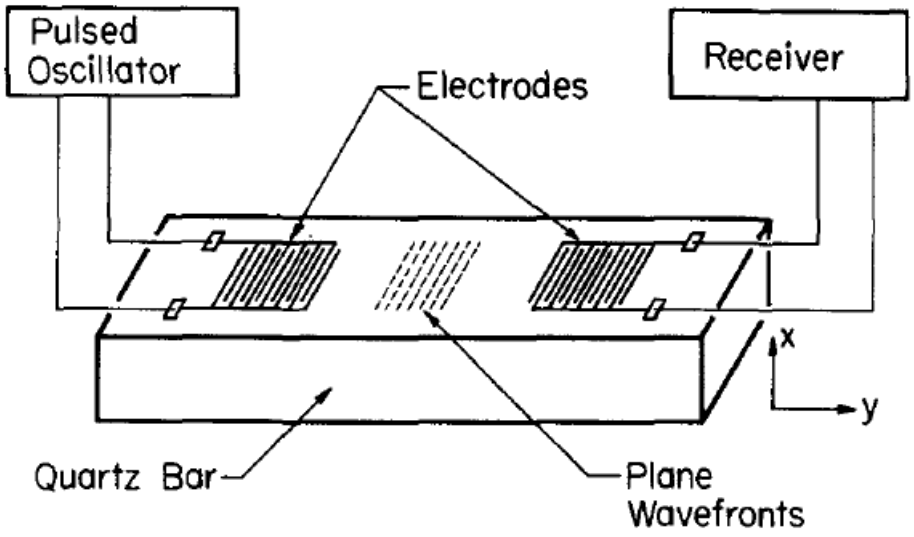

Figure 1.1: "Arrangement for surface wave transduction by electrodes on crystalline quartz bar"

by using measured elastic constant on Y-Z Lithium Niobate. For quartz, besides AT and BT cuts, the ST cut was investigated because of its good temperature coefficient of delay (TCD) by Schulz et al. in 1970 [7].

In 1971, Chauvin et al. [8] showed the first example of a SAW device used as TV IF filter, a bandpass filter on Y-Z Lithium Nobiate. In the same year Marshall and Paige [9][10] introduced the multistrip coupler consisting is an array of parallel unconnected electrodes. The two transducers are placed on different tracks, coupled by the MSC, so only surface waves are transferred while bulk waves are not. An alternative to Y-Z Lithium Nobiate is the 128°Y-X orientation which is characterized by having has less unwanted bulk waves excitation [11]. This means that MSC was not needed anymore. Moreover it allowed an area reduction. Other popular materials are Lithium Tantalate [**14**] and Zinc Oxide. The planar structure simplicity and the semiconductor-based fabrication made possible the production of SAW devices in high volume, reducing the cost. Because of this reason TV manufacturers started using these devices in volume in the next years. Also different structures were investigated. In 1970 Ash [12] proposed the use of gratings to provide reflectivity. By using metal strips or grooves at a proper pitch to form gratings, good reflectivity over a certain bandwidth was obtained. Resonators were built creating a resonant cavity by combining two gratings and two IDT's. Staples et al. [13] in 1974 showed first examples of these kind of resonators. Another device which was developed during the 70s is the convolver, employed

in signal processing. In this device, waves are generated at both ends and they overlap in the centre. The outptut waveform is the convolution of the inputs.

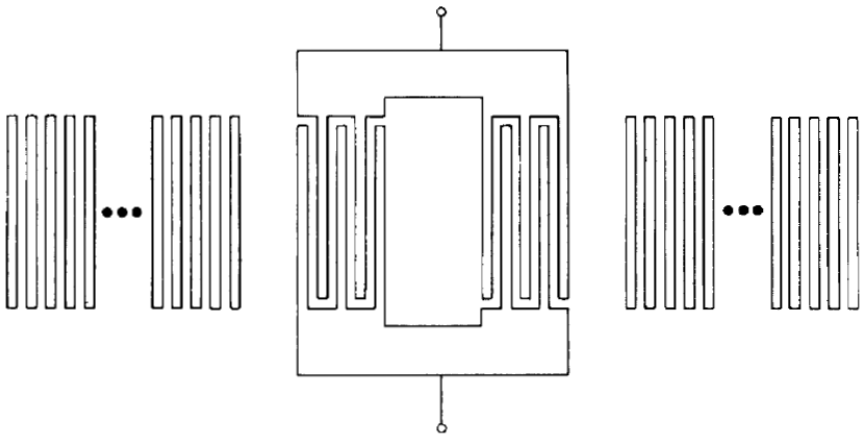

Figure 1.2: One-port SAW resonator

Later new types of waves were proposed. Leaky wave solutions, so called because of their complex wavenumber were identified by Engan et al. in 1967 [14] on X-cut quartz. In 1977, Lewis [15] demonstrated the Surface-Skimming Bulk Waves (SSBW), in rotated Y-X quartz. Then Auld et al. [16] introduced the Surface Transverse Waves (STW). These waves could be generated and confined close to the surface by gratings.

In 1982 Hartmann [**20**] introduced the Single-Phase Unidirectional Transducer (SPUDT) with the aim to reduce the insertion loss and reduce the unwanted multiple-transit effect. This asymmetric device generates waves in one preferential direction. In 1986 the Distributed Array reflection Transducer (DART) [**21**] was developed.

If before the 1985 the developments were in response to military and communications requirements (with the TV filter exception), later they were consumer driven, in particular for mobile phones, pagers, cordless phones and VCR's where cost and size were more important.

In particular in mobile phone applications were demanding for low loss compact IF filters. These requirements were met by multi-track DART filters [17][18] and by the Z-path filters [19][20]. Moreover, several novel SAW techniques were developed such as the Interdigitated Interdigital Transducer (IIDT) [21], the Double-Mode SAW filter (DMS) [**27**] and the Impedance Element Filter (IEF) [**28**][22].

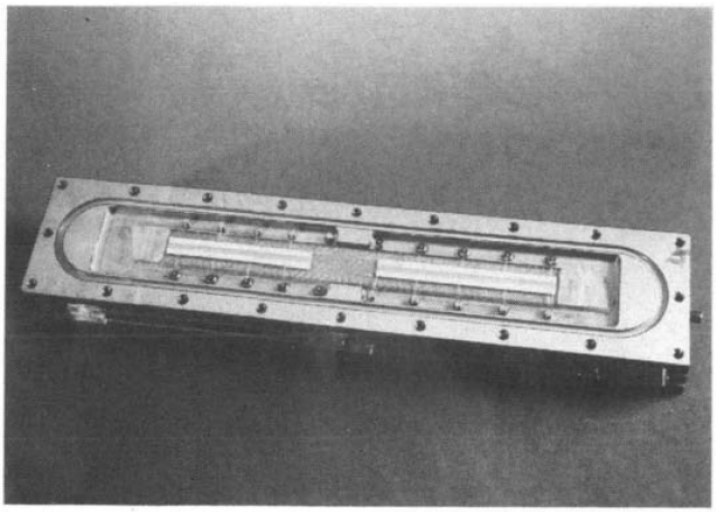

Figure 1.3: Typical SAW delay line fabricated on ST-cut quartz (1981)

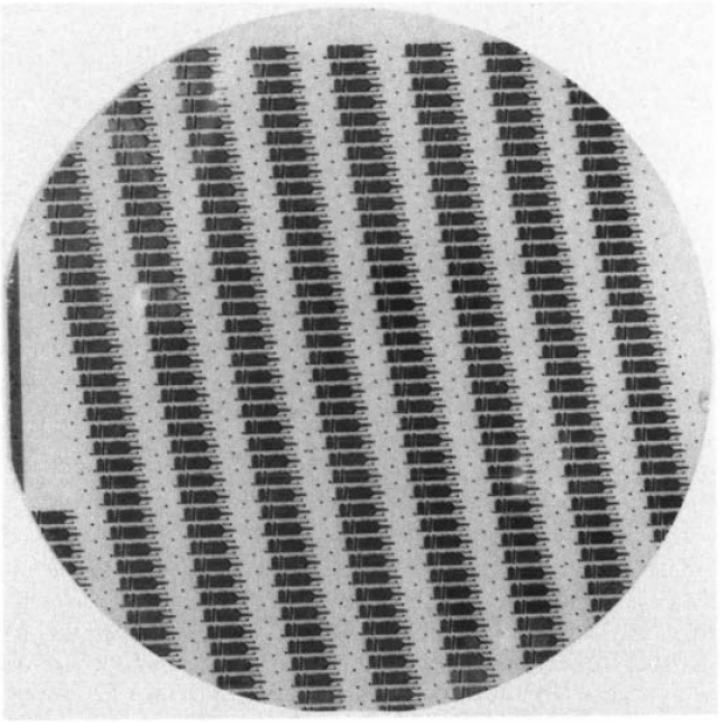

Figure 1.4: 260 TV IF filters fabricated on 128°YX $LiNbO_3$(1984)

1.2 History of SAW devices in biological applications

SAW devices have been found to be suitable for many technical applications in diverse fields, especially in electronics, in data processing and in high-frequency technology [23]. By the early 1980s, these devices became mass-produced thanks to the increasing demands of the products, especially in the telecommunication area. Lately, because of their characteristics such as their high working frequencies, small size, fast response and integration ability with different receptor materials, they became attractive for sensing applications. It was in 1979 when the first application as sensor of a SAW device occurred [24]. Wohltjen presented a Rayleigh surface acoustic waves based sensor. The device was coated with a sensitive polymer layer to be employed as organic gas detector.

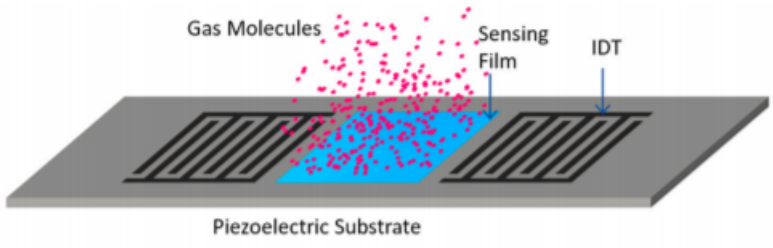

Figure 1.5: SAW gas sensor schematic

Since then several SAW sensors have been developed for different gas sensing applications [**32**]. However, initial attempts to convert SAW based gas sensors into a biosensors able to detect proteins were not convincing [25][26]. The critical issue was the operation in contact to liquid media. When immersed in aqueous buffer solutions, the Rayleigh waves devices suffer high attenuation. This is originated by the vertical displacement which radiates compressional waves into the liquid. The first successful approaches were achieved in 1987. Shiokawa et al. [27] used different crystal cuts of Lithium Niobate ($LiNbO_3$) and Lithium Tantalate ($LiTaO_3$) as substrate materials. The generated waves were called Shear Horizontal (SH) SAW. They introduced the use of a dual line configuration in order to evaluate the potential application as biosensor. In 1992, another kind of SH SAW device which exploit the Love wave effect was found to be even more suitable. By using a layer of material in which the wave velocity is lower than the sound speed in the liquid, the wave results guided through the layer, so the attenuation is kept under control. Gizeli et al. [28] presented this device based on a quartz substrate and a PMMA guiding layer. Immunoglobulin G (IgG) was adsorbed at the surface to capture two analytes, anti-IgG and protein A.

In 1993 Rapp et al. [29] presented an immunosensor based on $LiTaO_3$ substrate,

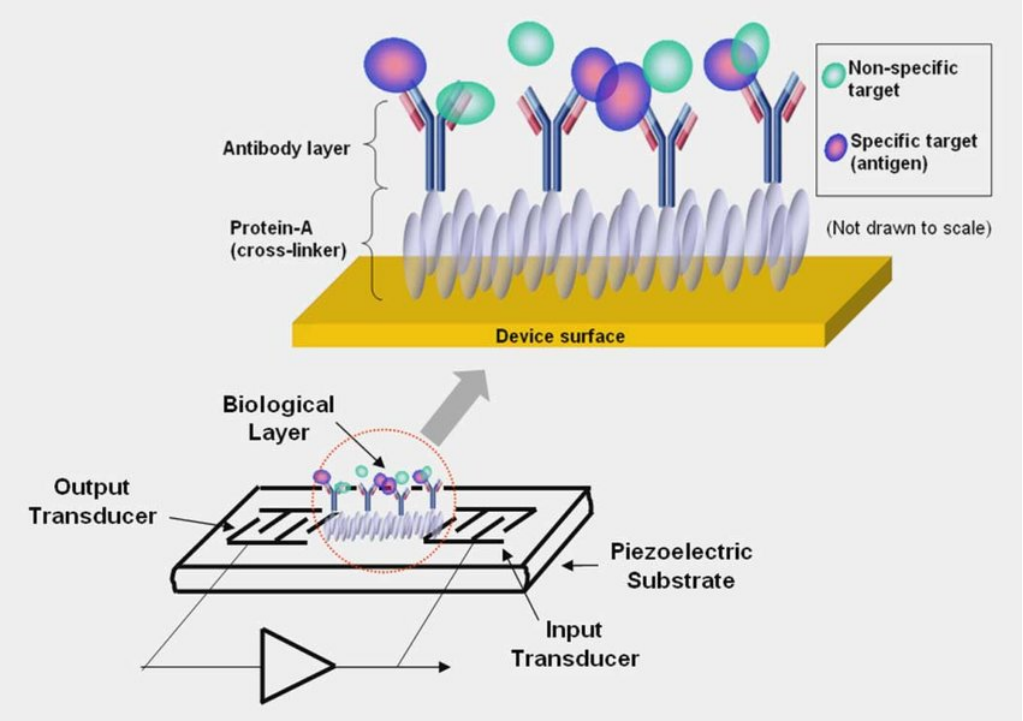

Figure 1.6: SAW immunosensor schematic

which employed Surface Transverse Waves (STW). Few years later Tom-Moy et al. [**38**] used a STW device to detect a low molecular weight compound, the pesticide Atrazine. In the early 2000s, Howe et al. [30] and Moll et al. [31] employed immunosensors to detect bacteria such as E.coli and Legionella. Stubbs et al. developed an immunossay RSAW device based on quartz, used to detect of analytes in a gas phase. By means adsorbed anti-bodies covered with a hydrogel layer, the main metabolite of cocaine (Benzoylecgonine) was detected. Later, in 2004 Schlensog et al. [**41**] proposed a Love wave SAW device for the detection of thrombin enzyme. The device was made up of a quartz substrate coated with a SiO_2 layer and a gold film. Self-assembled monolayer (SAM) were used to couple the Thrombin DNA aptamers on the sensor surface. More recently, (2005-2007) Roh et al. [32][33] proposed a SH SAW sensor built on a $LiTaO_3$ substrate with a thin gold film coating to detect 15-mer oligonucleotide DNA, a mutant part of an exon which cause Hunter syndrome.

1.3 State of the art

During the last few years some results which show the potential of these devices as biosensors have been published. Recent studies investigated the employment of SAW devices to detect various analyte, such as proteins, enzymes, bacteria and many others.

Crivianu-Gaita et al. [34] in 2015 proposed a SAW biosensor able to detect parathyroid hormone-related peptide (PTHrP), a breast and prostate cancer biomarker. The device was based on a electromagnetic piezoelectric acoustic device, characterized by a shear wave propagation on quartz substrate. Self-assembled monolayers of PFP were formed on the surface and fragment antigen-binding units were employed as biorecognition elements. Frequency shift of the pre-injection signal and the post-injection signal was measured,with respect to the operating frequency of 1.02 GHz.

Maria Gianneli et al. [35] in 2016 developed a nanostructured surface to enhance the molecular interaction with the sensor. They created nanopillars with a diameter of 35 nm of various heigth on top of a PMMA film, which acted as a waveguide for a Love wave sensor. The sensor was made to operate at 155 MHz and it employed a PMMA coated Y-cut z-propagating quartz substrate and a 192 pairs gold IDT, with a periodicity of 32 μm. In order to explore the improved binding capability of the sensor, phase and amplitude signals were measured during the adsorption of bovine serum albumin protein.

G. Moreau et al. [36] in 2016 presented a SAW biosensor aimed to investigate the binding between tumor necrosis factor α and the SPD-304, its inhibitor and to quantify their affinity. A dual delay line was fabricated on a 36°LiTaO3 substrate, whose IDTs were patterned with a 40 μm periodicity, to obtain an operating frequency of 104 MHz. Because of its thiol protein content, the TNF-α can bind covalently to the gold coated recognition layer. After that SPD-304 solutions are injected and phase shifts are measured with respect to the reference line.

Kordas et al. [37] in 2016, presented a work in which a DNA amplification method called isothermal Rolling Circle Amplification method is combined with a Love wave biosensor device to detect the Salmonella bacteria. The employed SAW devices operated at 155 MHz, using a 1 um thick S1805 photoresist layer as a waveguide. Initially Salmonella DNA template is incubated with padlock probe and the RCA is performed. Binding is provided by neutravidin protein which is pre-adsorbed on the surface of the polymer and by the biotin molecules which were incorporated in the amplified DNA. Variations of amplitude and phase of the waves were real-time monitored.

Xianhao Le et al. [38] in 2017, proposed a SAW humidity sensor made up of an AlN thin film deposited on a higly-doped Si substrate, with a graphene oxide sensing layer. The device consists in two IDTs composed of 60 pairs of fingers and

two grating of 180 fingers shorted to form a reflector, realized in aluminium. The frequency shift is mainly due to the water molecules adsorption which causes a mass variation of the graphene oxide film. As the relative humidity increases, the resonant frequency shift increases as well.

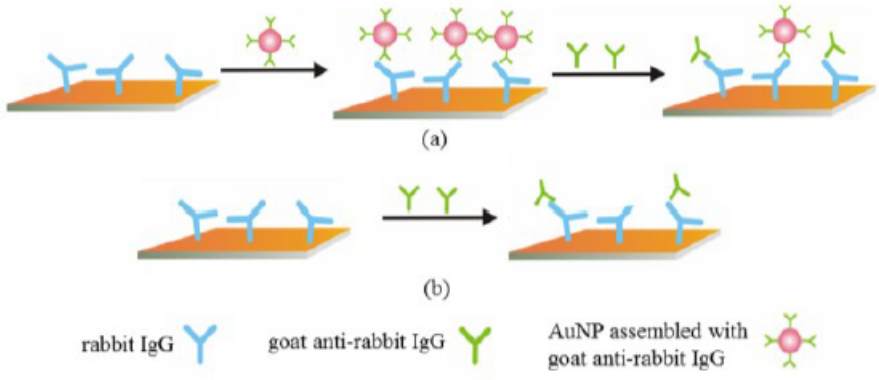

Figure 1.7: Detection strategy for IgG molecules using nanoprobes

A Love wave biosensing platform to detect carcinoembryonic antigen was proposed by Shuangming Li et al. [**49**] in 2017. The sensor is based on a ST 90°-X quartz substrate with a SiO2 overlay waveguide, operating at 120 MHz. To enhance the mass loading effect, the conjugate antibodies anti-CEA were altered intrducing gold nanoparticles. 60 finger pairs for each Au IDT were employed, each one characterized by a width of 10 μm. Real-time phase variation were measured by the detecting system during the sensing process.

In 2018 Shyam Trivedi et al. [39] simulated and fabricated a SH-SAW resonator to detect biotin, investigating the coupling with polymer S1813 micro-ridges. A 36°-YX LiTaO3 wafer was employed as substrate, while gold IDT and reflector grating were sputtered. The device which is expected to resonate at 200 MHz, consists of a 20 finger pairs IDT and a reflector having 251 electrode of a width of 5 μm. S1813 10 μm width micro-ridges are built along the propagation path. Surfaces of reference and sensing devices are silanized and bovine serum albumin and avidin are immobilized on it. Active areas are then incubated with solutions containing different concentrations of the protein and frequency shift is measured.

Eleanor R. Gray et al. [40] in 2018 proposed a clinical study of a HIV diagnostic device based on a SAW biosensor. They employed SH-SAW dual channel device to detect anti-p24 or anti-gp41 antibodies from plasma samples. The sensors were built on 36°Y-cut 90°X-propagation quartz, with gold IDT consisting of 80 finger pairs, operating at 251.5 MHz. Biochips were functionalized using dithiobis and a capture protein, a non-animal protein on the reference channel and a recombinant gp41 or p24 antigen on the detection channel. Devices were than tested with

plasma samples from patients with HIV and from healthy volunteer.

John J.Taylor et al. [41] in 2019, published a work about a SH-SAW based biosensor aimed to detect enzymes called salivary matrix metalloproteinase-8 (MMP-8). It represents a novel method to monitor periodontitis by means of specific antibodies. The device is a delay line structure with gold electrodes and gold coated sensing area, built on top of a quartz crystal. The biochip is functionalized with anti-Ig antibodies and the antigen/antibody binding reaction causes a perturbation which is detected as a wave phase variation. In 2020, Junwang Ji et al. [**53**] designed

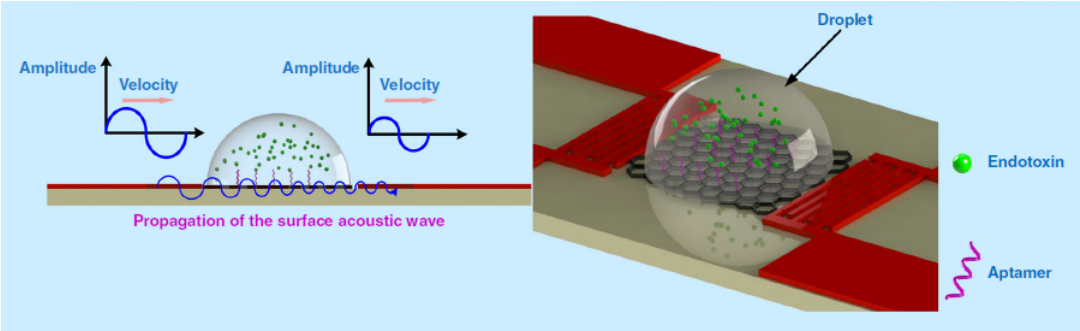

Figure 1.8: Principles illustration of endotoxin detection

a shear horizontal surface acoustic wave (SH-SAW) biosensor which employs a delay line and graphene layers to detect endotoxins. They fabricated it on a 36° Y-90° X quartz substrate, with sputtered Au IDTs and a CVD grown single-layered graphene film. The device operates at base frequency of 246.2 MHz and exploited the phase velocity variation due to mass loading to quantify the analyte. Chitosin was used to provide hyrophilicity and the aptamer was immobilized on the surface of the film by cross-linking with glutaraldehyde. Detection has been tested for Escherichia coli and aflaxotin.

Jandas et al. [42] in 2020 presented a SAW biosensor for label-free detection of carcinoembryonic antigen based on ST-cut quartz. In this work, a delay line consisting of two IDTs made up of Au electrodes of 150 nm thickness and 60 pair of fingers, was designed to operate at a centre frequency of 120 MHz. The sensitive area was coated with a gold layer and subsequently functionalized with thioglycolic acid. After that, an anti-CEA self-assembled monolayer was immobilized on it. Solutions of CEA with various concentrations were then used to evaluate the biosensing capabilities of the device.

Tsougeni et al. [**55**] in 2020 designed a lab on a chip platform for pathogen analysis in food. It combines a microfluidic chamber in which bacteria are captured, they are lysed and their DNA is amplificated. After that they are detected by a 4-acoustic channel SAW biosensor, built on ST-quartz substrate, whose electrodes have a split-fingers geometry, made up of aluminium. The detection of Salmonella,

B. Cereus, Listeria and E. coli in milk is demonstrated.

Chapter 2

Theoretical Background

2.1 Acoustic Waves

Sound is a mechanical wave generated by the motion of the sound vibration through a medium in which the mechanical wave travels [**56**]. It arises from a longitudinal movement of the medium's particles. Medium particles are set in motion by a vibrating source, which makes them to move around their relaxation point at a certain frequency. During the movement, particles push the adjacent ones creating a chain effect. This process generates travelling high and low pressure areas, whose interchange forms the sound waves. Acoustic waves need a medium to propagate their energy, so they can't travel over a vacuum. They are characterized by some key quantities such as frequency, wavelength, amplitude, phase and velocity.

An elastic material acts as a mass-spring system, in which the displacement of its elements results propagate through the medium. Elastic waves originates from the interaction between inertial and elastic forces. Since surface particles are constrained only from one side, surface disturbances behave differently with respect to interior ones, giving rise to unique modes called surface waves. The waves propagation in a solid depends upon solid properties and its boundaries.

A solid is put under stress by applying a force. Stress results in strain, so solid particles are displaced from their original positions in every direction. Displacements generated by a plane wave present a harmonic oscillation in the wave propagation direction [43].

$$u(x, y, z, t) = (u_1 x + u_2 y + u_3 z) e^{j(\omega t - kx)} \tag{2.1}$$

where u_i are the particles displacements in the 3 directions, ω is the angular frequency, and k is the wavenumber. The displacement gradient ∇u describes the interparticle distance variation, i.e. the local deformations of the solid. By adding

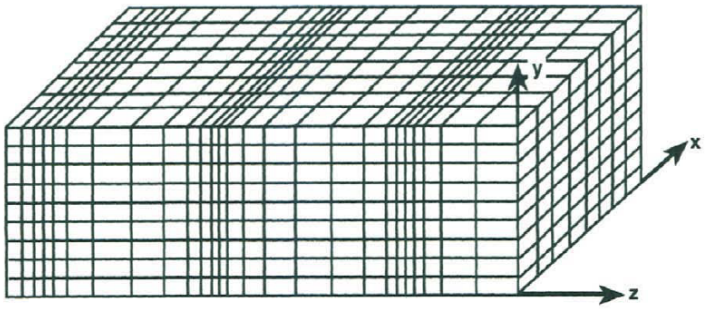

Figure 2.1: Compressional waves propagating in a solid

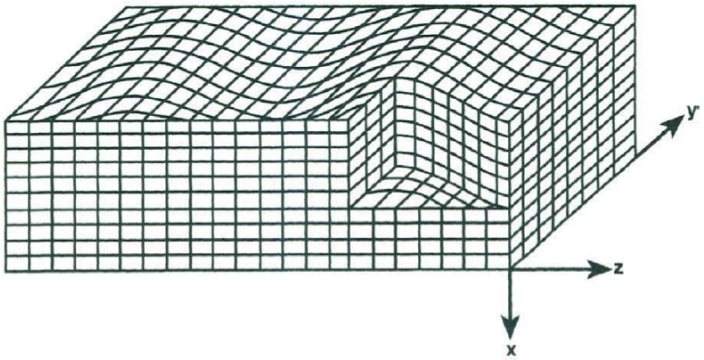

Figure 2.2: Shear waves propagating in a solid

the displacement gradient to the its transpose, the strain matrix S is obtained.

$$S_{ij} = \frac{1}{2}(\partial u_i/\partial x_j + \partial u_j/\partial x_i) \tag{2.2}$$

Strain is the length variation per unit length, in response to applied stress. To complete the description, the stress tensor definition is required. Its elements T_{ij}, represent the i-th force per area component of applied to the j-th face of an infinitesimal volume element.

Stress and strain definitions allow the derivation of the equation of motion for elastic deformations of a solid, in particular wave motion. It can be written since the net force in the i-th direction, which is the sum of the product of Tij times the area, is equal to the product of the mass time the accelleration, as in the Newton's

law. After dividing by the volume, this equation is obtained,

$$\sum_{j=1}^{3} \frac{\partial T_{ij}}{\partial x_j} = \rho \frac{\partial^2 u_i}{\partial t^2} \tag{2.3}$$

generalized to all three directions i = 1, 2, 3. For small deformations in a solid, it has been proved that the strain is linearly proportional to the applied stress, as in the Hooke's law [44]. In three-dimensional solids, this principle can be generalized as:

$$T_{ij} = \sum_{k,l=1}^{3} c_{ijkl} S_{kl} \tag{2.4}$$

where the elastic stiffness constants c_{ijkl} act as "microscopic spring constants", relating strain to a given stress. From the equation of motion and the elastic constitutive equation, the wave equation for plane waves in a non-piezoelectric solid is derived.

$$\sum_{j=1}^{3} \frac{\partial T_{ij}}{\partial x_j} = \sum_{j,k,l=1}^{3} c_{ijkl} \frac{\partial^2 u_k}{\partial x_j x_l} \tag{2.5}$$

for i = 1, 2, 3. Its solution is made up of different propagating wave modes: a quasi-compressional wave, which is characterized by a displacement along the propagation direction, and two quasi-shear waves, with displacement perpendicular to the propagation direction.

2.2 Piezoelectricity

Acoustic waves can be electrically generated in many crystals by exploiting the coupling between strain and electrical. In crystal structures which lack a center of inversion symmetry [45] the charge distribution can be altered by a strain application, causing an electrical polarization. This effect is known as direct piezoelectric effect. Conversely, in the inverse piezoelectric effect, an electric field application induces a strain in the crystal. By properly modifying the elastic and the electromagnetic constitutive relations, equations which govern the relation between electric field and strain are obtained.

$$T_I = c_{IJ}^E S_J - e_{IJ} E_j \tag{2.6}$$

$$D_I = \epsilon_{ij}^S E_j + e_{iJ} S_J \tag{2.7}$$

They are called piezoelectric constitutive relations, in which e_{Ij} are the piezoelectric stress constants, E_i are the electric field components, D_i are the electrical displacement components, and ϵ_{ij} are the permittivity constants. Reduced notation has been employed in such a way that the subscript I replaces two lower-case subscripts (I, J = 1,.., 6).

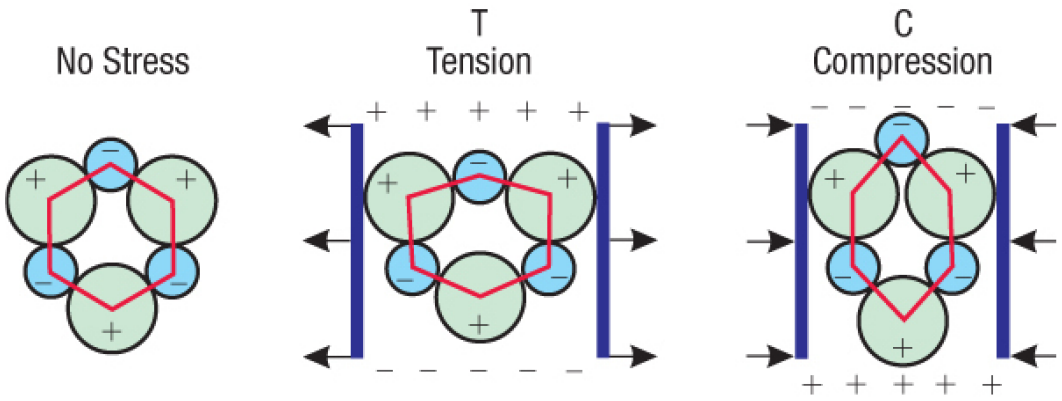

Figure 2.3: Effects of tension and compression on piezoelectric material

The piezoelectric wave equation is derived from the piezoelectric constitutive relations. Typically it is expressed in terms of displacements u_i and electric potential ϕ. Substituting the first piezoelectric constitutive relation into the equation of motion yields to

$$\sum_{j,k,l=1}^{3} c_{ijkl} \frac{\partial^2 u_l}{\partial x_k x_j} + \sum_{j,k=1}^{3} e_{ijk} \frac{\partial^2 \phi}{\partial x_k x_j} = \rho \frac{\partial^2 u_i}{\partial t^2} \tag{2.8}$$

Differently from the non-piezoelectric media case, it is evident the presence of an additional term related to the electric potential, which can be considered as a source term. Conversely, the wave displacements generate an electrical potential which allow to electrically detect the piezoelectric wave.
Acoustic-wave sensors typically detect the change of wave velocity and/or attenuation due to the interaction with the environment. These changes are related to wave energy density and power dissipation variations. In particular, the wave velocity variation is equal to the wave energy density variation with opposite sign.

$$\frac{\Delta v}{v_0} = -\frac{\Delta U}{U_0} \tag{2.9}$$

where U_0 and v_0 are the unperturbed energy density and propagation velocity. Because of the relation between mass density and energy density changes, the wave velocity variation is also linked to the medium mass density variation:

$$\frac{\Delta v}{v_0} = -\frac{\Delta \rho}{\rho_0} \tag{2.10}$$

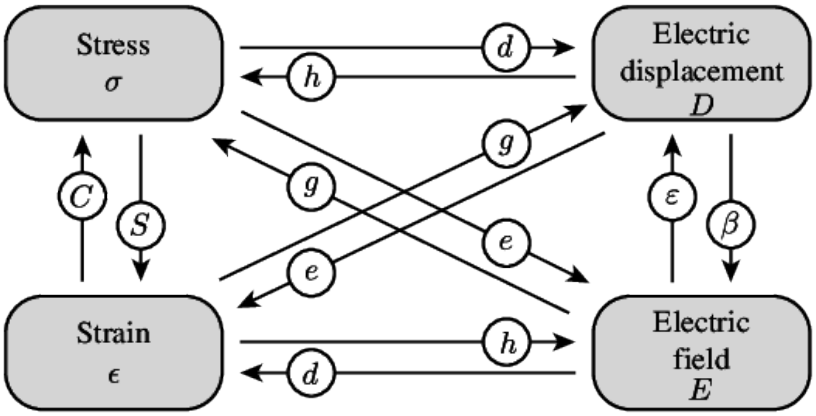

Figure 2.4: Relations between piezoelectric quantities

2.3 SAW excitation, parameters and responses

Acoustic wave devices show sensitivity to several kinds of perturbations. This capability is typically achieved by coupling the device to a sensitive element, which acts as a transducer between acoustic and chemical domains. In order to detect perturbations, the sensing element must vary its properties in response to them. A generic z-propagating surface acoustic wave, is characterized by such displacement profile

$$u(x, y, z, t) = (u_x(y)e^{j\Phi_1\hat{x}} + u_y(y)e^{j\Phi_2\hat{y}} + u_z(y)e^{j\Phi_3\hat{z}})e^{j\omega t-\gamma z} \tag{2.11}$$

where ω is the angular frequency, γ is the propagation factor u_x, u_y and u_z are the displacement components and Φ_i are the phases of the components. Amplitude decays along y direction into the substrate as $e^{-2\pi y/\lambda}$. As a consequence the superficial confinement of the acoustic energy close to the surface occurs, enhancing the sensitivity.

Imposing the inexistence of the transverse component, $u_x = 0$, (2.11) becomes the displacement profile of a Rayleigh wave. In this propagation mode, u_y and u_z are perpendicular and the particles describe an elliptic orbit in the sagittal plane.

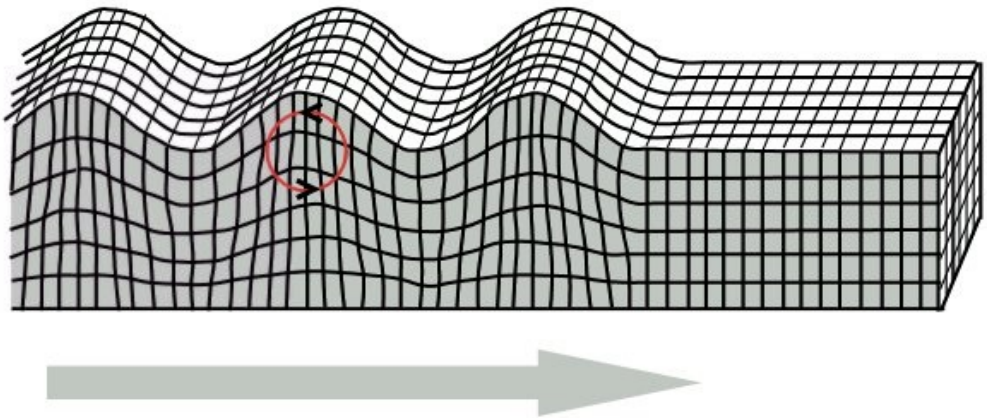

Figure 2.5: Rayleigh wave particles motion

SAW are typically excited on a piezoelectric material by a lithographically patterned interdigital electrodes or interdigital transducers (IDT). An alternated voltage application to the opposite electrodes induces a periodic electric field in the substrate, producing a periodic strain and a consequently standing surface wave. IDT generates propagating waves in both directions, whose fronts are parallel to

the electrodes. Transducer periodicity or pitch p, which is the distance between opposite polarization fingers, defines the synchronous frequency,

$$f_0 = \frac{v_0}{p} \tag{2.12}$$

where v_0 is the SAW propagation velocity. The best efficiency is reached by exciting the transducer at this frequency value, which corresponds to the condition in which the periodicity matches the wavelength lambda. A wave potential Φ is associated to the mechanical wave. When it reaches the receiving IDT, it induces a current flow in each fingers, which combine into the detected output current.

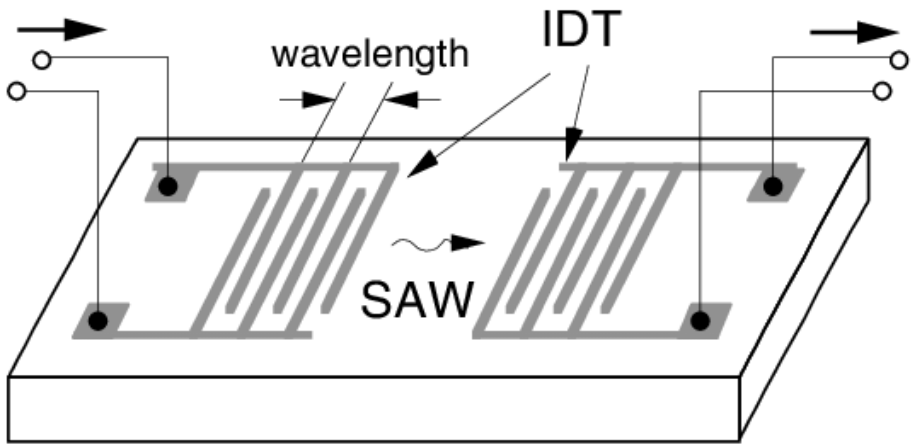

Figure 2.6: Interdigital transducers

Each finger can be considered as a discrete source of SAW. When a continuous wave voltage is applied, an electric potential can be associated to each finger. The IDT frequency response is consequence of the interference between fingers contributions and the wave potential of a propagating wave is the vector sum of these contributions.

$$\Phi^+(z) = \mu_s \sum_{n=0}^{N_f-1} V_n e^{jk(z-z_n)} \tag{2.13}$$

where V_n is the voltage exciting the n-th finger, located at $z = z_n$ and N_f represents the fingers number. The device frequency response will be proportional to the Fourier transform of the contributions [46]. Applying alternating voltages to the fingers, $V_n = (-1)^n V_o$, (6.13) becomes

$$\Phi^+(0) = \mu_s V_0 \sum_{n=0}^{N_f-1} (-1)^n e^{-jnkd/2} \tag{2.14}$$

which is a geometric series. At the synchronous frequency, when the waves wavelength λ is equal the fingers periodicity, the sum elements add constructively. Away from f_0, the addition is not coherent leading to a frequency response

$$\Phi^{+}(f) = \left| \frac{sin(X)}{X} \right| \tag{2.15}$$

in which

$$X = \frac{N_p \pi (f - f_0)}{f_0} \tag{2.16}$$

and $N_p = N_f/2$ When the detuning parameter X is a multiple of π, it gives rise to a complete cancellation between between finger contributions. As a consequence the frequency response shows nulls on sides of f_0, creating an interval B which is the transducer bandwidth, inversely proportional to the number of fingers

$$B = \frac{2 f_0}{N_p} \tag{2.17}$$

The IDT bandwidth B becomes narrower as the number of finger pairs N increases, however there are some limitations. Practically, when N overcomes 100 the IDT impedance increases and the advantages are nuetralized since losses from scattering and from mass loading become too high [47].

In SAW-based sensors, perturbations influence wave propagation parameters, such as velocity and attenuation. Numerous interactions between SAW and surface film which give rise to these variations have been investigated. Coupling between surface waves and sensitive layer can be either mechanical or electrical, thanks to the piezoelectric nature of the medium. Interactions arising from mechanical deformation include mass loading and viscoelastic effects.

In the SAW mass loading effect, the travelling wave causes the harmonic motion of the surface which puts the superficial particles into movement in an elliptical orbit. The reason for the characteristics variations is that the surface displacement makes the kinetic energy density U_k to increase.

$$\Delta U_k = \frac{\rho_s}{4} (v_{x0}^2 + v_{y0}^2 + v_{z0}^2) \tag{2.18}$$

where ρ_s is the surface mass density and V_i are the superficial particle velocities at the surface. Recalling (6.9), it is possible to derive the relation between velocity change and mass loading

$$\frac{\Delta v}{v_0} = \frac{-\omega v_0 \rho_s}{4} \left(\frac{v_{x0}^2}{\omega P} + \frac{v_{y0}^2}{\omega P} + \frac{v_{z0}^2}{\omega P} \right) \tag{2.19}$$

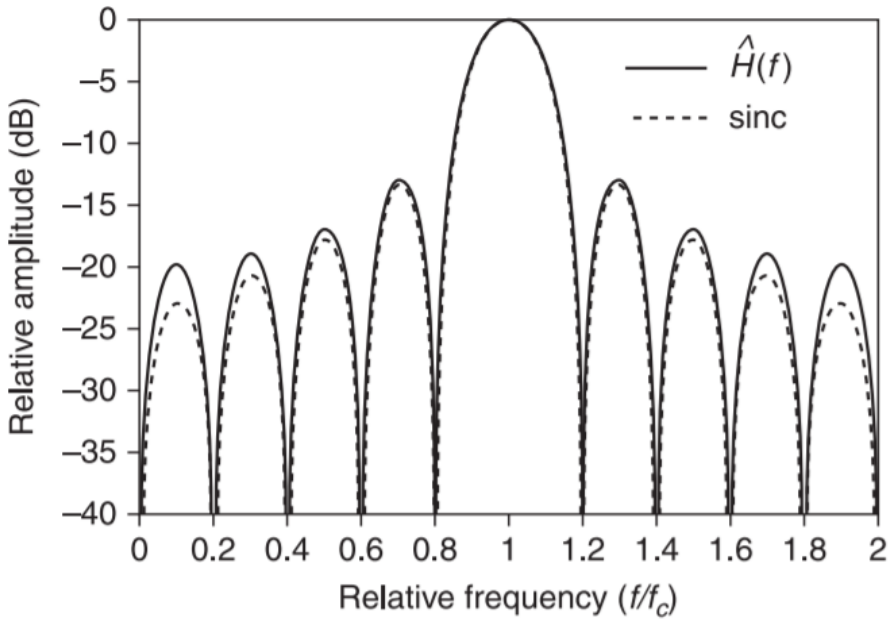

Figure 2.7: Delay line frequency response

where the term in the parentheses depends only on the substrate. Quantities which are not depending on the material can be grouped, leading to the expression

$$\frac{\Delta v}{v_0} = -c_m f_o \rho_s \tag{2.20}$$

in which c_m is the mass sensitivity.

2.4 Piezoelectric Materials

Piezoelectric materials are commonly classified into four major categories such as single crystals, ceramics, polymers, and polymer composites. Single crystal materials have a structure characterized by regularly ordered ions, which lead to the proper dipoles alignment and to the piezoelectric behaviour [48]. Lithium Niobate ($LiNbO_3$), Lithium Tetraborate ($Li_2B_4O_7$) and Quartz are the most known. Piezo-ceramic materials structure is made up of many single crystal grains, whose orientations are various. Lead Zirconate-Titanate (PZT), Barium Titanate ($BaTiO_3$), Potassium Niobate ($KNbO_3$) belong to this class [49]. Piezoelectric polymers are carbon-based materials made up of long polymer chains. This feature make them flexible and suitable for applications where high strain is required. Polyvinylidene Fluoride (PVDF), Polyamides (PA), Polylactic Acids (PLA) lie in this category. Piezoelectric polymer composites are materials made of piezoelectric ceramic nano particles combined with polymers. The combination enhances the materials electromechanical properties, exploiting the good features of both the categories. Regarding crystalline piezo-materials, a key role is played by the crystallographic

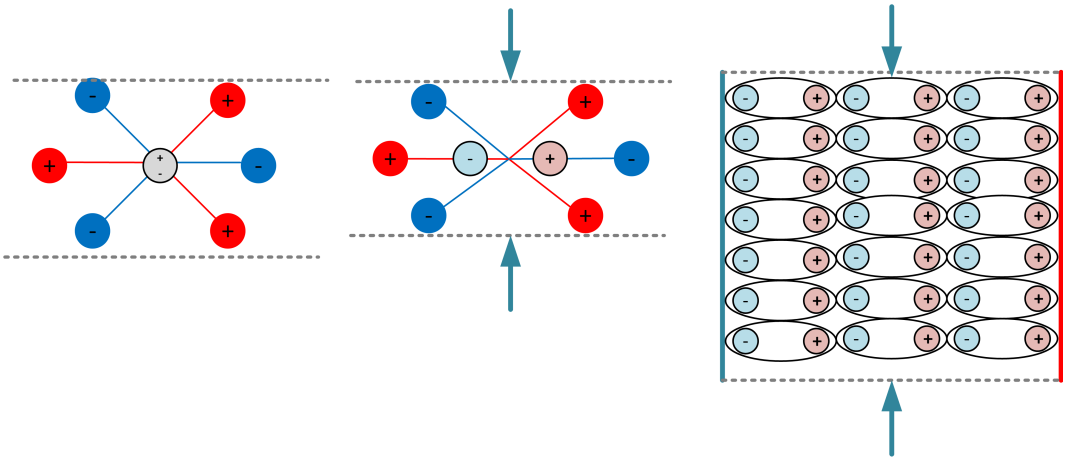

Figure 2.8: Piezoelectric material behaviour

symmetry. The absence of a centre of symmetry is a mandatory requirement for the piezoelectric effect existence. Among the crystallographic classes, only the 21 noncentrosymmetric ones allow this effect. Seven crystal systems belong to this category: triclinic, monoclinic, orthorhombic, tetragonal, trigonal, hexagonal and cubic [50].

Piezoelectric constitutive relations (6.6) and (6.7) can be written in matrix form as

$$\begin{pmatrix} T_1 \\ T_2 \\ T_3 \\ T_4 \\ T_5 \\ T_6 \end{pmatrix} = \begin{pmatrix} c_{11}^E & c_{12}^E & c_{13}^E & c_{14}^E & c_{15}^E & c_{16}^E \\ c_{21}^E & c_{22}^E & c_{23}^E & c_{24}^E & c_{25}^E & c_{26}^E \\ c_{31}^E & c_{32}^E & c_{33}^E & c_{34}^E & c_{35}^E & c_{36}^E \\ c_{41}^E & c_{42}^E & c_{43}^E & c_{44}^E & c_{45}^E & c_{46}^E \\ c_{51}^E & c_{52}^E & c_{53}^E & c_{54}^E & c_{55}^E & c_{56}^E \\ c_{61}^E & c_{62}^E & c_{63}^E & c_{64}^E & c_{65}^E & c_{66}^E \end{pmatrix} \begin{pmatrix} S_1 \\ S_2 \\ S_3 \\ S_4 \\ S_5 \\ S_6 \end{pmatrix} - \begin{pmatrix} e_{11} & e_{21} & e_{31} \\ e_{12} & e_{22} & e_{32} \\ e_{13} & e_{23} & e_{33} \\ e_{14} & e_{24} & e_{34} \\ e_{15} & e_{25} & e_{35} \\ e_{16} & e_{26} & e_{36} \end{pmatrix} \begin{pmatrix} E_1 \\ E_2 \\ E_3 \end{pmatrix} \tag{2.21}$$

$$\begin{pmatrix} D_1 \\ D_2 \\ D_3 \end{pmatrix} = \begin{pmatrix} e_{11} & e_{12} & e_{13} & e_{14} & e_{15} & e_{16} \\ e_{21} & e_{22} & e_{23} & e_{24} & e_{25} & e_{26} \\ e_{31} & e_{32} & e_{33} & e_{34} & e_{35} & e_{36} \end{pmatrix} \begin{pmatrix} S_1 \\ S_2 \\ S_3 \\ S_4 \\ S_5 \\ S_6 \end{pmatrix} + \begin{pmatrix} \epsilon_{11}^S & \epsilon_{12}^S & \epsilon_{13}^S \\ \epsilon_{21}^S & \epsilon_{22}^S & \epsilon_{23}^S \\ \epsilon_{31}^S & \epsilon_{32}^S & \epsilon_{33}^S \end{pmatrix} \begin{pmatrix} E_1 \\ E_2 \\ E_3 \end{pmatrix} \tag{2.22}$$

where c^E is the elastic stiffness or tensor of the elastic constants at constant electric field, e is the piezoelectric stress tensor and ϵ^S is the dielectric tensor at constant strain.

This matrices are the key properties to define a piezoelectric material. The number of the independent components of the tensors is related to the symmetry level of the crystal. Crystals characterized by higher symmetry have a lower number of them.

In particular, trigonal crystal system has 6 independent components for a third-rank tensor. Lithium Niobate belongs to this category. $LiNbO_3$ is a trigonal 3m ferroelectric material at room temperature. In the last few decades, Lithium Niobate gained much interest. Thanks to its physical properties, such as the large electromechanical coupling coefficient and large electro-optic coefficients, it became one of the most important piezoelectric material. It is employed for elastic, elasto-optic, acoustic and acousto-optics devices [51].

Its elastic and piezoelectric parameters have been investigated by many researchers. However, discrepancies exist among the magnitude of some coefficients. The reasons can be related to the different crystals qualities [52].

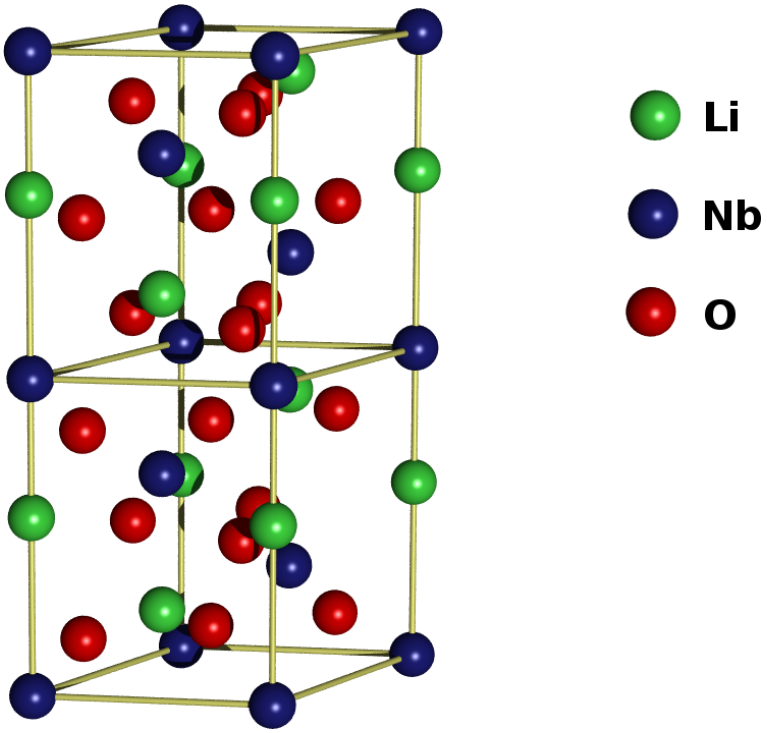

Figure 2.9: $LiNbO_3$ elementary cell

In this work, $LiNbO_3$ has been modeled by using these data [51]:

$$c_{ij}^E = \begin{pmatrix} c_{11}^E & c_{12}^E & c_{13}^E & c_{14}^E & 0 & 0 \\ c_{12}^E & c_{11}^E & c_{13}^E & -c_{14}^E & 0 & 0 \\ c_{13}^E & c_{13}^E & c_{33}^E & 0 & 0 & 0 \\ c_{14}^E & -c_{14}^E & 0 & c_{44}^E & 0 & 0 \\ 0 & 0 & 0 & 0 & c_{44}^E & c_{14}^E \\ 0 & 0 & 0 & 0 & c_{14}^E & \frac{(c_{11}^E - c_{12}^E)}{2} \end{pmatrix} =$$

$$= \begin{pmatrix} 203 & 57.3 & 75.2 & 8.5 & 0 & 0 \\ 57.3 & 203 & 75.2 & -8.5 & 0 & 0 \\ 75.2 & 75.2 & 242.4 & 0 & 0 & 0 \\ 8.5 & -8.5 & 0 & 59.5 & 0 & 0 \\ 0 & 0 & 0 & 0 & 59.5 & 8.5 \\ 0 & 0 & 0 & 0 & 8.5 & 72.85 \end{pmatrix} \left[10^9 \frac{N}{m^2}\right]$$

$$e_{ij} = \begin{pmatrix} 0 & 0 & 0 & 0 & e_{15} & -e_{22} \\ -e_{22} & e_{22} & 0 & e_{15} & 0 & 0 \\ e_{31} & e_{31} & e_{33} & 0 & 0 & 0 \end{pmatrix} =$$

$$= \begin{pmatrix} 0 & 0 & 0 & 0 & 3.76 & -2.43 \\ -2.43 & 2.43 & 0 & 3.76 & 0 & 0 \\ 0.23 & 0.23 & 1.33 & 0 & 0 & 0 \end{pmatrix} \left[\frac{C}{m^2}\right]$$

$$\epsilon_{ij}^S = \begin{pmatrix} \epsilon_{11}^S & 0 & 0 \\ 0 & \epsilon_{11}^S & 0 \\ 0 & 0 & \epsilon_{33}^S \end{pmatrix} = \begin{pmatrix} 44.3 & 0 & 0 \\ 0 & 44.3 & 0 \\ 0 & 0 & 27.9 \end{pmatrix} \left[\frac{C}{m^2}\right]$$

2.5 Molecularly Imprinted Polymer

Antibodies are proteins characterized by unique functionalities and tasks. They are involved in several processes regarding the regulation of the immune system. These biomolecules identify and target their antigens, binding specifically to them when they come in contact. The massive use of biomolecules receptors is limited, mainly because of their instability and their costs. Bioinspired synthetic materials such as MIPs represent an interesting surrogate due to their relatevely low cost, their mechanical and chemical stability and their robustness to environtmental conditions. Molecularly imprinted polymers (MIPs) are synthetic materials which can imitate natural receptors, recognizing and trapping the analytes. In this technology, functional monomers and cross-linkers are co-polymerized in presence of the target molecule, which act as a template. The removal of the template molecules results in the creation of cavities which are their complementar replicas in terms of shape, size and functional groups orientation. Thanks to these characteristics they act as binding sites for the template molecules, being able to selectively rebind them [53].

Initial investigations on molecular imprinting technology were performed in the

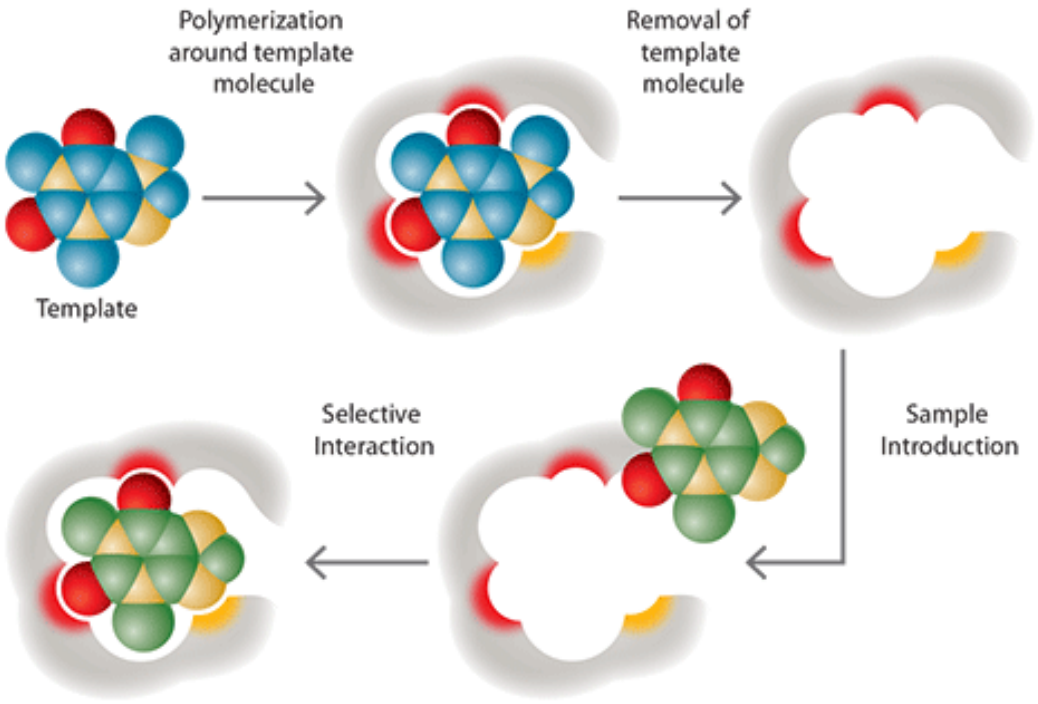

Figure 2.10: MIP synthesis and interaction

1930s by Polyakov, whose research was focused on chromatography applications [54]. He reported the effects of the presence of some hydrocarbons in silica polymer,

during its drying [55]. In 1942, the production of antibodies in vitro was achieved [56] and their selectivity was investigated, opening the way to new applications. In 1949, Pauling described a method which involved the polymerisation of silica in presence of different dye molecules. After that the additives were removed, the resulting silica matrix showed the capability to rebind to them [57]. During the following decade, selectivity theory, association mechanism and polymerisation processes were reinvestigated. Molecular imprinted silica was employed in chromatography [58], structure elucidation [59], catalysis and other applications. After the 1960s, the interest in these kind of materials decreased until the 1972, in which Klotz and Wulff introduced molecular imprinting in synthetic organic polymers [60]. This work inspired several following studies during the 1970s and 1980s. Introduction of molecular imprinting of metal ions [61] and non-covalent approaches [62] increased the range of potential applications of the technology. Arshady and Mosbach introduced the molecular imprinting by self-assembly, in which template and monomers show weak interactions [63]. Later, the idea of employing MIPs as antibody mimics in immunoassays was demonstrated. Vlatakis and Mosbach in 1993 [**78**] proposed a revolutionary work, in which drugs levels determination in human serum were performed. This reasearch opened the way to several new applications along the following years and established the role of MIP technology as recognition materials. From the beginning of the new millenium applications such as immunoassays [64], biosensor [65], affinity separation [66] and catalysis [67] employ MIPs consistently.

The process to prepare the MIP consists of three steps: the association, the polymerization and the elution. During the associating step the template molecules, the functional monomer and the cross-linker bind into a complex, which can be covalent or non-covalent. After that, a polymerization reaction such as electropolymerization, photopolymerization or thermal polymerization, cross-links copolymer entrapped with template molecules. A 3D porous polymer network is obtained, in which the functional groups of the monomer combine in an ordered spatial arrangement. The template molecules are subsequently dissociated from polymers through the action of an eluent. Tailor-made cavities matching the imprinted molecules are formed [68].

The techniques for preparing MIPs can be grouped according to the template and functional groups interactions. They can be covalent or non-covalent. In the former types, which is also named pre-assembly method, template molecules covalently bind to monomers, and then cross-linking polymers are created. The latter types are the most commonly used. Template molecules and monomers form a prearranged self-assembly based on weak interactions, such as hydrogen bonds, ionic, or van der Waals forces.

The reagents involved in the preparation of a MIP are the template molecule, functional monomer, cross-linker, initiator, and solvent. The target molecule can

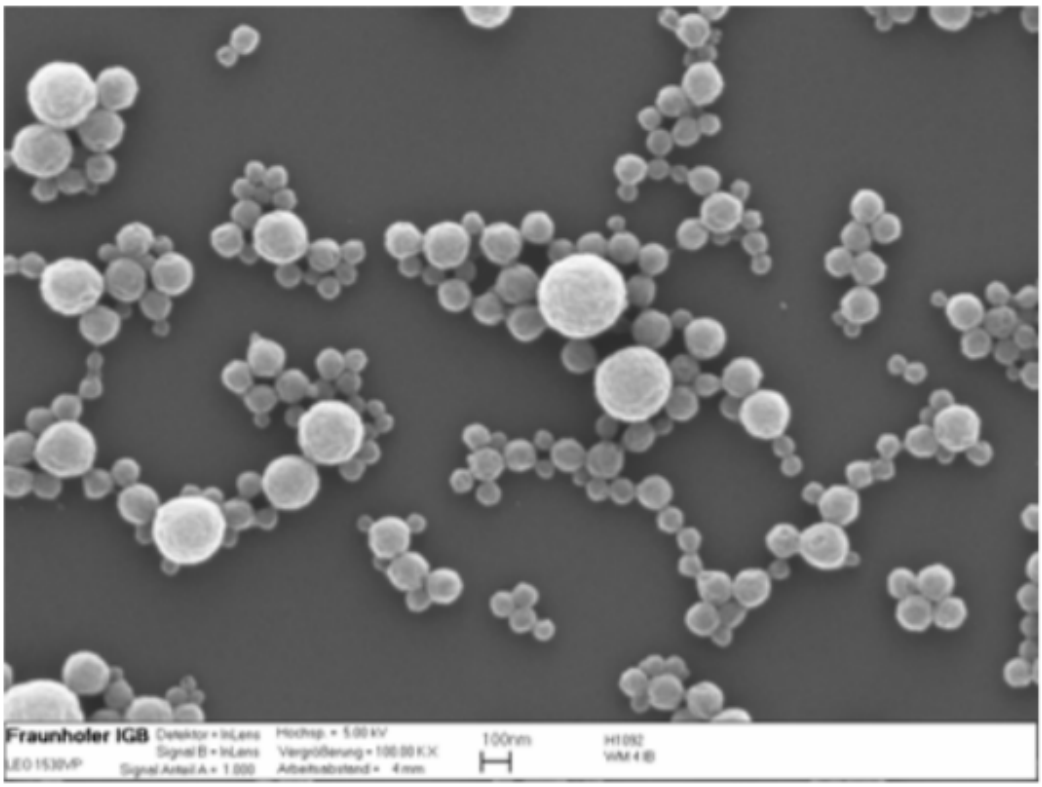

Figure 2.11: MIP SEM micrograph

be of various kinds, such as proteins, amino acids, vitamins and many others. Functional monomer has the role to provide specific functional groups in the polymerization. Its molar ratio with respect to the imprinted molecule influences the selectivity of the binding sites. Cross-linkers bridge the molecules to establish a network among each other, regulating the polymer chain formation. Their ratio affects the stability of the cavities and so the recognition ability. The initiators are the compounds which provide free radicals, employed into polymer cross-linking reaction. The solvent provides the polymer porosity and promote the interactions among the molecules.

Main MIP polymerization methods are bulk polymerization, suspension polymerization, precipitation polymerization and in situ polymerization which comprehends electropolymerization methods [69].

Electrochemically synthesized polymers are a class of polymers prepared by electrochemical polymerization of electroactive functional monomers, which can be either conducting or nonconducting. Because of their properties, they gained a great interest* for chemical sensors and biosensors applications. Electropolymerization is characterized by many advantages. It allows to finely control the polymer nucleation

rate and its growth, the thickness of the structure by controlling the amount of charge passed during the deposition and the polymer morphology by selecting proper solvent and electrolyte. Several different polymers have been stably synthesized, such as Polyacetylene, Polyphenylene Polypyrrole (PPy), Polythiophene (PTh), Polyaniline (PANI), Poly(1,2-Phenylenediamine). Moreover, these materials have been used extensively to develop sensors based on MIPs. In particular we are interested into 1,2-Phenylenediamine, also known as o-Phenylenediamine (OPD), an organic compound having the formula $C_6H_4(NH_2)_2$. The Phenylenediamine (PD) functional monomer is particularly suitable for molecular imprinting. It forms rigid and compact polymer films, which can be made thin and continuous, guaranteeing a short response time and it can be applied to MIP-based sensors targeting either low or high molecular weight substances, such as drugs, pesticides, proteins and enzymes [70].

o-PD has been employed in many applications as recognition element in the last years, such as a QCM biomimetic sensor for glucose, a bulk acoustic wave (BAW) sensor for atropine, a paracetamol voltammetric microsensor, dopamine sensor and many others.

2.6 Finite Element Method

Differential equations are used to model most of the natural physical phenomena and they represent an essential tool to analyze and understand them. In general, the analytical resolution of these boundary value problems is extremely complex and sometimes it is unavailable. Numerical methods leading to approximate solutions are employed to overcome this difficulty. Finite element analysis is a technique which represent a valid approach to the problem. In the Finite Element Method a continuum problem is solved by dividing the solution domain into smaller ones. These elements are called finite elements. Each of them is a simple unit whose behaviour can be readily analysed. The possibility to apply it to complicated geometry systems makes this method attractive to several applications. The complexity of the problem can be reduced by employing a large number of simple individual elements. The price of this simplification is the increase of the numerical computations that must be done.

A FEM algorithm consists in a number of steps. Initially, the weak formulation of the partial differential equation (PDE) must be derived. The second step consist in a finite dimensional discretization of the problem weak formulation, in which the integration domain is partitioned (meshing) and a proper interpolation function is chosen as approximant. Then the weak formulation is translated into an algebraic equations valid for each element, called element stiffness equations. These latter ones are then assembled into an algebraic equations system called global stiffness system governing the entire domain. Finally, the obtained system is solved, so unknown nodal parameters are computed [71].
FEM label first appeared in 1960 [72], but the idea of functional minimization over sub-regions was older [73]. It was initially used to solve structural analysis problems. During the 1950s and 1960s, it was exploited in the aerospace industries and later in civil and aeronautical engineering. Only later this method started to be employed in the resolution of problems in several application fields, such as electromagnetism and wave phenomena.In 1964, first commercial finite element software was released. Each element and each node was represented on a keypunched IBM card. Later these softwares started to be run on corporate computers. In 1980, workstation was introduced, bringing many advantages among which the interactive graphics. Finally with the PCs introduction, FEM became an extremely cost effective solution. Today several commercial softwares are available, such as CADs which allows to easily generate complex geometry [74].

)

PDEs can be expressed as

$$Lu = f \tag{2.23}$$

where, L is the differential operator, u is the unknown field quantity and f is the source term. These terms are defined over a domain Ω, with boundary conditions

assigned on $\Gamma = \partial\Omega$.

The weak formulation (or variational) is an integral formulation derived from the initial strong formulation. To establish the weak formulation, the original equation is multiplied by an arbitrary function called test function, and it is integrated over the domains [75]. By doing it, following canonical representation is obtained,

$$a(u, v) = F(v), \qquad \forall v \in V \tag{2.24}$$

where u is the unknown solution and v is a test function. $a(u, v)$ is called bilinear form and $F(v)$ is the linear form (or linear functional).

The meshing operation concerns the discretization of the problem space. The domain is divided into a finite number of elements, in such a way to minimize the discretization error. According to the domain characteristics, different element shapes can be used. Hexahedral, prismoidal and pyramidal in the 3D case and triangular and tetrahedral in the 2D case. The quality of the mesh strongly influences either the convergence and the accuracy of the solution. Elements aspect ratio and angle widths are some of the factors which must be taken under control to guarantee an optimal subdivision [76]. The numerical method must provide an approximation

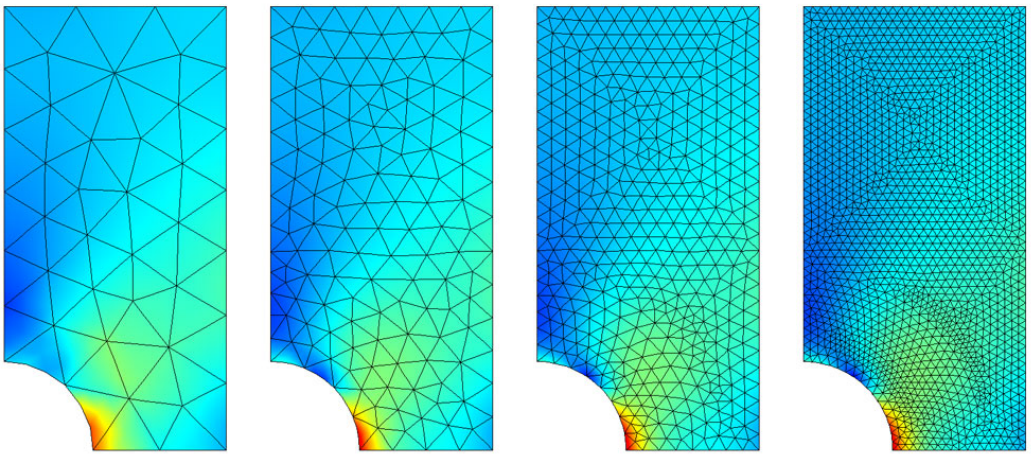

Figure 2.12: Triangular mesh refinement

u_h of the exact solution u. The discretization depends on a real parameter $h > 0$, $h \to 0$, which is a measure of the grid fineness. By taking it sufficiently small, the error $u - u_h$ will be small enough to guarantee the required accuracy. In particular, the numerical method is said convergent when $\|u - u_h\| \to 0 \quad$ as $h \to 0$.

In FEM, a weighted residual method is commonly used to derive the approximated equations, such as the Galerkin method. By discretizing both the unknown

and the test functions (6.12) becomes

$$a(u_h, v_h) = F(v_h), \qquad \forall v_h \in V_h \tag{2.25}$$

Moreover by denoting as $\varphi_j, \quad j = 1 : N_h$ a basis of V_h, (6.13) becomes

$$a(u_h, \varphi_i) = F(\varphi_i), \qquad i = 1 : N_h \tag{2.26}$$

The unknown function u_h can be written in the form

$$u_h(x) = \sum_{j=1}^{N_h} c_j \varphi_j(x) \tag{2.27}$$

where the coefficients c_j represent the new discrete unknowns.

Therefore, since $a(u_h, v_h)$ and $F(v_h)$ respectively are equivalent to:

$$\sum_{j=1}^{N_h} c_j a(\varphi_j, \varphi_i) = F(\varphi_i), \qquad i = 1 : N_h \tag{2.28}$$

that is

$$\begin{pmatrix} a(\varphi_1, \varphi_1) & a(\varphi_2, \varphi_1) & \cdots & a(\varphi_{N_h}, \varphi_1) \\ a(\varphi_1, \varphi_2) & a(\varphi_2, \varphi_2) & \cdots & a(\varphi_{N_h}, \varphi_2) \\ \vdots & \vdots & \ddots & \vdots \\ a(\varphi_1, \varphi_{N_h}) & a(\varphi_2, \varphi_{N_h}) & \cdots & a(\varphi_{N_h}, \varphi_{N_h}) \end{pmatrix} \begin{pmatrix} c_1 \\ c_2 \\ \vdots \\ c_{N_h} \end{pmatrix} = \begin{pmatrix} F(\varphi_1) \\ F(\varphi_2) \\ \vdots \\ F(\varphi_{N_h}) \end{pmatrix} \tag{2.29}$$

or

$$Ac = F \tag{2.30}$$

where $(A)_{ij} = a(\varphi_j, \varphi_i)$

Lagrangian basis functions represent a common choice as FEM basis $\varphi_i(x)$. These basis functions are characterized by a very small support. Each $\varphi_i(x)$ has null value everywhere, except in a small subset of the PDE domain. The choice of this kind of basis leads to a sparse final linear system, so the majority of the integrals must not be computed, decreasing computational cost and memory storage.
They are so defined

$$\varphi_i(x_j) = \delta_{ij} \tag{2.31}$$

where

$$\delta_{ij} = \begin{cases} 1 & i = j \\ 0 & i \neq j \end{cases} \tag{2.32}$$

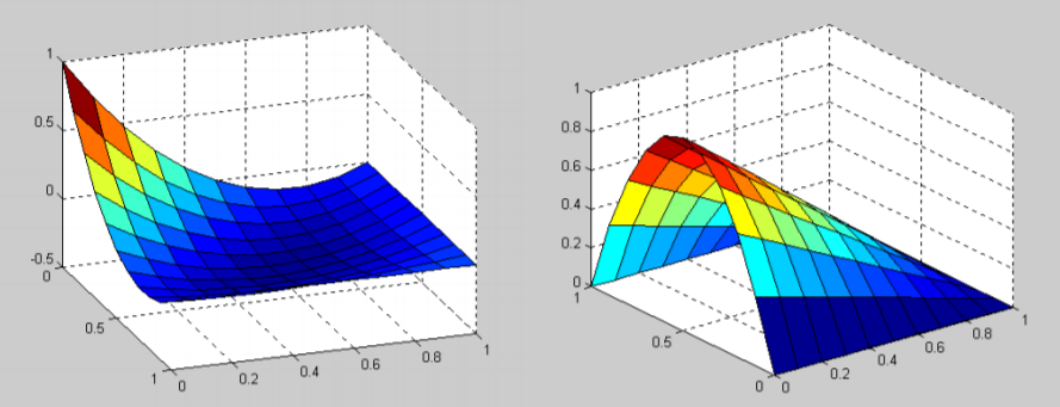

Figure 2.13: FEM quadratic basis functions

Moreover, since

$$u_h(x) = \sum_{i=0}^{N} c_i \varphi_i(x) \tag{2.33}$$

hence

$$c_j = u_h(x_j) \tag{2.34}$$

Finally the problem is reduced to a system of linear equations of the form

$$Ac = F \tag{2.35}$$

which can be solved either by means of direct or iterative methods. Direct methods are based on the Gauss elimination method, which can be seen as a sequence of multiplications of both members of the system. Following this approach, LU factorization and Cholesky factorization of the A matrix are obtained. These methods are robust but can be inefficient for large scale problems, because of the large amount of data to be stored. On the other hand, in these conditions iterative methods such as Conjugate Gradients method or Generalized Minimum Residual method (GMRES) requires less memory compared to the direct ones.

Chapter 3

SMILE Project

3.1 Introduction

Every year in Europe about 150,000 new patients are affected by head and neck cancers, and about 60% [77] of advanced stage diagnosed cases result in the patient's death within 5 years. Among these cancers, Oral Squamous Cell Carcinoma (OSCC) is the most common. It is estimated that 1.7 million people worldwide are diagnosed with neck squamous cell carcinoma and more than 330.000 patients die every year. OSCC is a cancer which occurs at the lips, at the junction of the palates or the posterior region of the tongue. The main risk factors are smoking, alcohol use and oncogenic viruses (such as papillomavirus HPV). This disease is usually diagnosed at an advanced stage, which results in the necessity of highly invasive surgery and postoperative chemotherapy, heavily compromising quality of life. On the contrary the cases which are diagnosed at the initial stages of the disease are characterized by a quite high survival rate (>85%). It is for this reason that the early diagnosis becomes crucial and strongly needed [78]. However screening methods such as biopsy, endoscopy, chest X-ray and contrast tomography have some critical issues. They can be invasive, non-accurate, complex, expensive and stressfull fo the patients.

To improve the quality and the compliance of these tests many biomarkers have been investigated. In particular the cytokines, a class of biomolecules which are involved in the inflammatory processes. Because of their role, they can be employed as markers for cell proliferation. It has been demonstrated that in the patients with oral cancer, also at early stage, a particular salivary cytokine called the interleukin-10 (IL-10) shows an increased concentration. If traditional diagnostic tests has some drawbacks, on the other hand collecting saliva is non-invasive, simple and rapid.

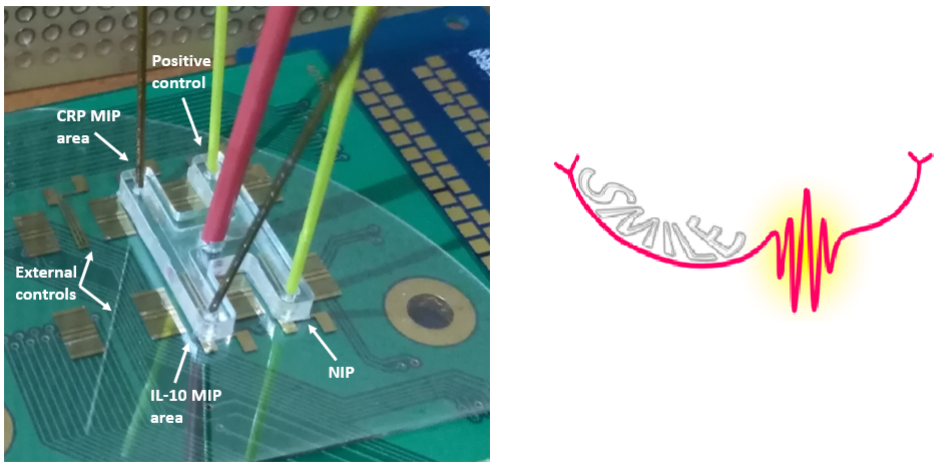

Figure 3.1: SMILE: a SAW-MIP Integrated device for oraL cancer Early detection.

Embracing this philosophy, CNR NANOTEC and STMicroelectronics collaborate on SMILE project, a joint project aiming at developing a diagnostic tool for the analysis of the saliva. The proposed diagnostic platform is based on electrosynthesized Molecularly Imprinted Polymer (MIP) working as synthetic receptors for IL-10, integrated with Surface Acoustic Wave (SAW) transducers, promising high sensitivity and selectivity of the assay. The device will be a microfluidic platform characterized by compact size, portability, easy of use and low cost. Moreover its simplicity will allow to be used also by a minimal trained personnel. Because of these benefits, it will possible to provide a large-scale screening in order to reduce the OSSC incidence and preserve the patients health.

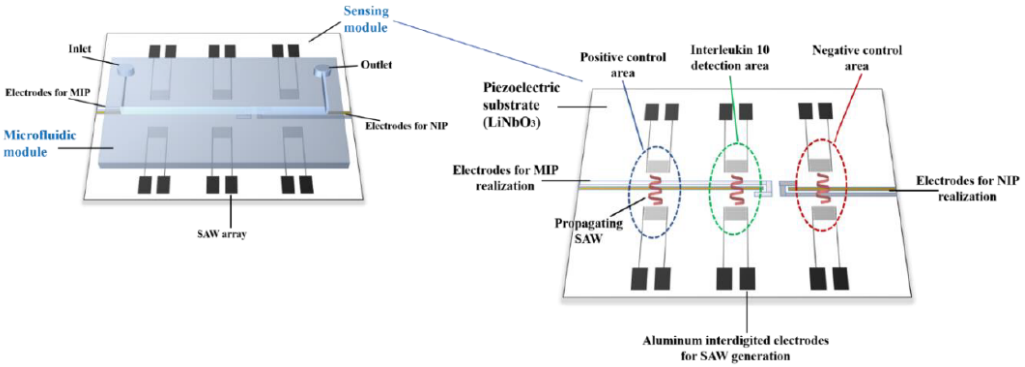

Figure 3.2: Device schematic with the microfluidic module, SAW and MIP/NIP lines for detection and control

The preliminary steps of the project are:

- The realization of the SAW transducers. Surface acoustic waves (SAW)-based devices represent a well-established technology in electronics and telecommunication fields. Recently they have been employed also in sensing platforms because of their sensitivity to changes at propagating surface [79]. These can affect the travelling waves in terms of frequency, amplitude and phase, which are measurable quantities. This, along with the possibility to functionalize the propagation surface in order to capture the analyte of interest, makes the biodetection possible [80]. The SAW transducers will be created by fabricating metal interdigitated electrodes above a Lithium Nobiate ($LiNbO_3$) piezoelectric substrate, through optical lithography.

- The realization of the sensing element such as the electrosynthetized MIP and their mutual integration Molecularly Imprinted Polymer (MIP) are smart materials which can act as artificial antibodies. They are polymerized in presence of the analyte of interest, which acts as template molecule. Once these molecules are washed away, they leave cavities in the polymer, which can selectively rebind the analytes when they get into contact. Moreover the possibility to directly polymerize MIP at the surface of electrodes from electroactive monomers by electrochemical methods [81], makes them particularly suitable for integration in miniaturized microfluidic sensor platforms. The choice of the MIPs as sensing element allow to overcome the problem of the antibodies storage conditions, which represent a critical issue affecting thr shelf life of the bioassay. Moreover the sensor can be regenerated simply by washing it with a proper buffer solution (i.e. ammonium/methanol 70:30) [82]. A set of SAW/NIP (non-imprinted polymer) is used as negative control, while a set of SAW/ non-washed MIP is used as reference. Finally a microfluidic module, made up of inlets, outlets and a channel through which the saliva sample will be pumped, will be mounted after the polymerization.

- The device calibration for detection of the IL-10 The presence of the Interleukin 10 (IL-10) in the saliva has been associated with the OSCC. Moreover its concentration increases already in the initial stages of the disease, while it is very low in healthy patients [83]. Because of this reasons, the use of this molecule as marker for the inflammation process represents an attractive diagnostic solution. In order to optimize the sensing platform, a calibration is required. It consists in a fine tuning of the concentration of the analyte as template during the MIP electrosynthesis. In such a way the amount of active sites of the final structure will be known, a quantity which will affect its sensitivity. Initially, known concentrations of IL-10 will be dissolved in PBS solution. This will provide information about the sensor working condition.

Considering that IL-10 concentrations in saliva are around 30 pg/ml in patients and below 10 pg/ml in healthy cases [84], a limit of detection (LOD) of limit of few picograms/ml is expected. In order to deliver the samples over the sensing surface in an orderly fashion, a microfluidic channel is going to be integrated.

- The analysis of real saliva sample to test and validate the device To validate the SMILE platform, the performances in presence of the real samples will be simulated and tested. Saliva samples spiked with selected IL-10 concentrations will be incubated over the MIP and SAW measurments will be carried out. In such a way the platform will be validated.

Nowadays, biomarkers of pathologies in biological fluids are identified and quantified by means of biochemical assay techniques, such as ELISA. These methods are time-comsuming, they need complex instrumentation and higly trained operators. Among these, applications which employs saliva biomarkers are mainly based on colorimetric assays [85], such as pH control, HIV selfdiagnosis and hormone dosing and they need examinations to confirm diagnosis.

SMILE aims to be a compact and easy-to-use "sample-in/answer-out" technology, in order to reach as many people as possible. The developing platform will integrate SAW transducers with MIP technologies, whose combination promises a performance improvement in term of sensing capabilities with respect to antibody-based assays. Moreover, the imprinting and subsequent rebinding of a polymer allows [86] to selectively identify small analytes, such as low molecular weight protein like IL-10.

The well consolidated partnership between CNR NANOTEC, a nanotechnologies-focused research institute active in many fields such as smart materials and precision medicine, and STMicroelectronics, a company which has the development of smart technologies among its objectives, gives rise to this project. They share the same research area in Lecce, where the micro- and nanofabrication facility allows the realization of the devices. The joint publications about SAW sensing device, materials [87], Lab on Chip [88] and immunosensing biochip show that the consortium owns the skills and the experience to deal with the proposed topics.

Number of patients involved, dangerousness of the disease and difficulties in the traditional screening tests lead to the necessity of new cost-effective diagnostic tools, in order to increase the survival rate and improve the clinical treatment. SMILE's aim is to accomplish these requirements, providing a high sensitivity/high specificity sensing platform to detect biomarkers in saliva samples. Moreover SAW-based biosensors require minimal additional instrumentation and power supplier can be integrated with microfluidic module. Because of the MIP benefits such as the capability to perform repeated operations, its mechanical strength and its resistance to heat, pressure and chemical, this biosensor can represent a breakthrough into

near-the-bed tests. Besides the reduction of mortality rate, the project will help to optimize the resources usage and to decrease the impact of the disease on health costs. The technology optimized for this biomarker can be applied to several other molecules of diagnostic interest and could be also integrated into smartphones or personal computers. SMILE system could be used for wide-ranging screening, to obtain information and knowledge, which can improve the understanding of the risk-factors influence and the population health for the next years.

3.2 Acoustic wave sensors

Electroacoustic sensors based on piezoelectric crystals have been built in several different configurations. They can be one-port or two-port devices. In the former ones, the single port act as input as well as output port. The charges generated on the electrode by the input signal cause an impedance variation which can be sensed. In the latter, the input port generates an acoustic wave that propagates toward the output port. Here a receiving transducer regenerates the signal. Amplitude and phase delay can be sensed as responses. The most common are the thickness shear mode (TSM) resonator, the surface acoustic wave (SAW) device, the acoustic plate mode (APM) device, and the flexural plate wave (FPW) device. The TSM resonator, also called Quartz Crystal Microbalance (QCM), is made up of a thin disk of quartz in which acoustic waves are excited by electrodes on both sides. Applied voltage produces a shear deformation of the material and its surface displacement which is maximum at the surface, makes it sensitive to superficial perturbations. The surface acoustic wave (SAW) devices, which are characterized by an acoustic propagation confined close to the surface. Their good energy confinement allows them to be generated by surface electrodes, mainly by interdigital transducer (IDT). It also results in a high sensitivity to surface perturbations.

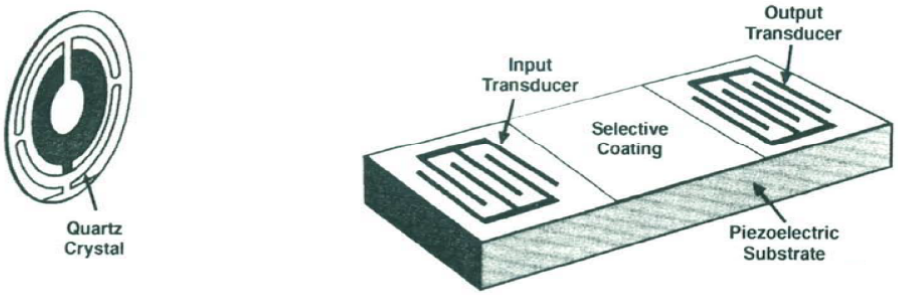

Figure 3.3: TSM and SAW devices

The shear horizontal Acoustic Plate Mode (APM) devices show a predominantly surface parallel displacement, perpendicular to the propagation direction. They are mostly employed in liquid applications because of their low attenuation when in contact with it. Quartz confines the acoustic energy between the two surfaces, working as an acoustic waveguides. imposing a resonance condition. Detection can occur at both lower and upper surfaces.

In Flexural Plate Wave (FPW) devices, waves excitement occurs in a thin membrane few micrometers thick. Phase velocity can be imposed to be lower than that in the liquid, allowing to not radiate into the liquid. This feature makes them suitable for liquid applications. Because of the large generated displacement, these

devices can either be employed as actuators.
Among acoustic devices, SAW devices are characterized by high operating frequency, compactness, ruggedness, fast response. These properties make them particularly suitable for biosensing applications. Moreover they can be integrated with several different receptor materials, having the capability to target various analytes, such as chemical agents, toxic gases, organic compounds and biomolecules. The variety of sensitive interfaces which can be employed includes carbon nanotubes, molecular coatings, self-assembled monolayers and molecularly imprinted polymers.

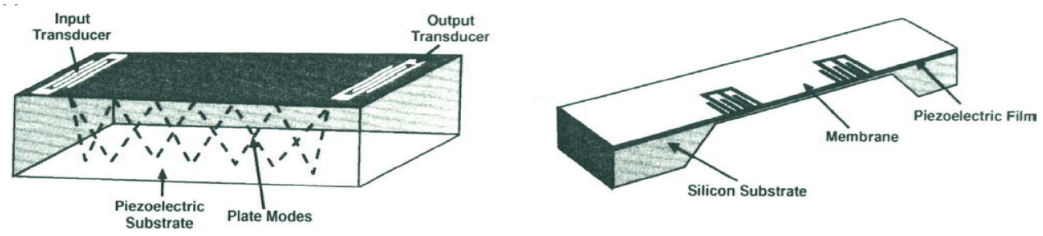

Figure 3.4: APM and FPW devices

3.3 Design Criteria

In this section, design parameters and their influence on the SAW devices behaviour are investigated. After their definition, they are used as input parameters in a mathematical model that has been implemented in Matlab, in order to test their effects on the frequency response of the devices. Delay lines employed in the SMILE sensing platform are made up of two identical unapodized IDTs, a transmitter and a receiver. The IDTs are separated by a region which hosts the sensing area, where two extra electrodes needed to form the MIP are present. SAW delay lines present many advantages with respect to other acoustic devices, including simple design and fabrication processes. Because of their high surface confinement capability, good sensitivity can be accomplished. They have been fabricated on several piezoelectric materials, such as quartz, $LiNbO_3$, $LiTaO_3$, ZnO, AlN and many others. Among

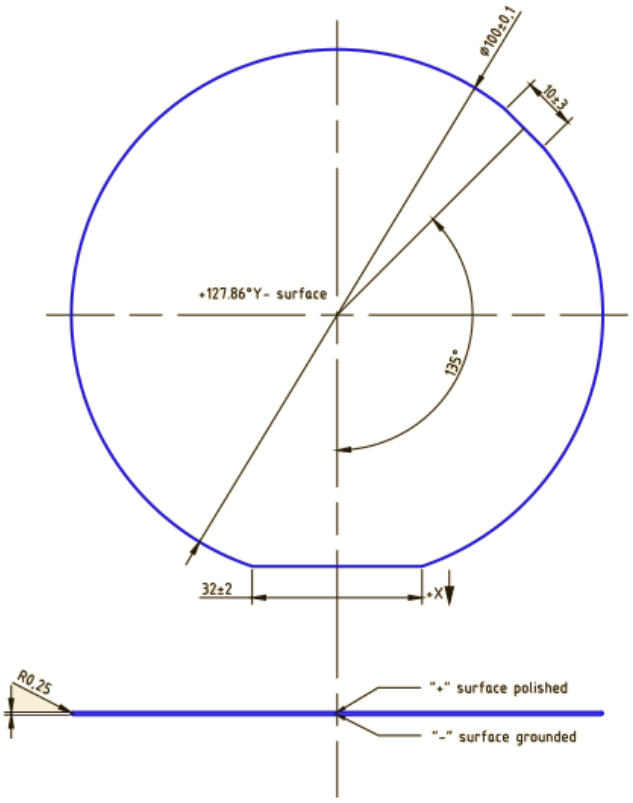

Figure 3.5: $LiNbO_3$ 128°YX wafer orientation

these, $LiNbO_3$ is a well established substrate material in SAW technology. It provides high electromechanical coupling coefficient (up to 15%) and quite high

acoustic wave velocity (from 3488 to 4750 m/s) [89]. Moreover this material shows a good stability and low acoustic loss. Substrate cut and orientation is an important factor, which leads to different piezoelectric properties. In particular, devices have been fabricated on 128°Y-cut X-propagation $LiNbO_3$ wafers, a cut which provides low bulk wave excitation, eliminating the need of multistrip couplers, decreasing the device area [90].

Precedently, lines have been built with IDTs fingers either parallel that perpendicular to X-axis. The second configuration showed a lower wave velocity but also a higher peak amplitude response and a higher amplitude variation in response of surface mass loading. Reasons which made this orientation attractive for the application, so X-axis perpendicular propagation has been chosen.

Gold has been selected as metal for IDTs electrodes. Its resistance to corrosion and good conductivity makes it suitable to operate in these conditions. Its inertness prevents it to adhere to the substrate, thus a nanometric layer of Cr has been employed to promote the adhesion.

As stated before, the device synchronous frequency depends only on the acoustic waves velocity in the substrate and on the pitch of the fingers. Thus after the substrate selection, the operating frequency f_0 is imposed by the choice of the spacing between fingers.

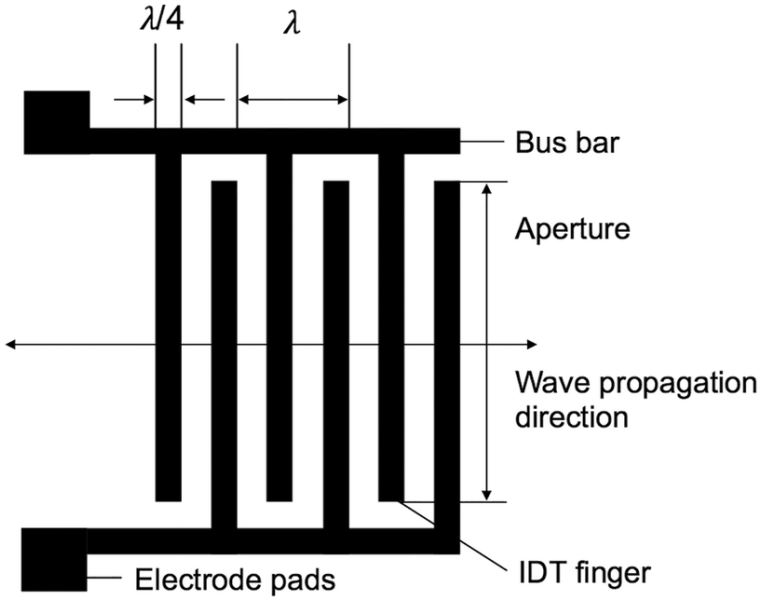

Figure 3.6: IDT geomentry

Photolithography resolution limits the minimum electrode width, since below a certain dimension the quality of the fabrication process becomes poor, leading to a lower yield. Another issue is represented by the instrumentation needed to perform

the measurements: if the synchronous frequency is too large, it becomes harder to test it under the proper operating conditions. On the other hand, the sensibility of the device is a parameter which strongly depends on f_0, so it is important to guarantee that this value doesn't drop too much. Evaluating these considerations, fingers width has been chosen to be 8 width, with a 50% metallization ratio. It means that also the spacing among opposite polarization fingers has the same dimension. This choice leads to a frequency value of about 114 MHz, which guarantees a good sensibility and compliance with standard measurement system. Also the choice the number pairs of fingers has been investigated. This number is responsible of the bandwidth of the device, i.e. the width of the main peak in the frequency response. Higher number of fingers leads to narrower bandwidth, but it will affect the impedance of the IDTs increasing the losses. Practically this number should not overcome 100. In this work, devices have IDTs with 80 pairs of fingers, leading to a bandwidth of 2.85 MHz. Another parameter of interest is the so called acoustic aperture, which represents the length of the overlap of opposite polarized fingers. Aperture is related to diffraction: if this length is too little (below 30λ), distorsions take place. In particular far from the transducer, beam diverges with a certain angle which depends on this parameter. A 1.2 mm aperture has been employed. The number of fingers, along with their height and the aperture influence the capacitance of the fingers. The capacitance is strictly related to the electrostatic force generated by the transducer and consequently to the surface displacement [91].

The height of the electrodes should be lower than 0.01λ in order to properly excite Rayleigh waves. Moreover, it can't overcome by three times the value of the resist thickness. A value of 50 nm has been selected for this parameter.

Finally the distance between the two IDTs has been designed to be 3.5 mm, in order to have room enough to place two extra electrodes, that will be employed in the electrosynthesis of the MIP/NIP structures.

These values are summed up in Table 3.1.

Finally, CleWin has been used to design photolithographic masks. CleWin is a powerful layout editor designed to draw photolithographic mask tool.

Table 3.1: Delay line parameters

Parameter	**Value**	**M.U.**
# Fingers pair	80	
Finger width	8	μm
Finger height	50	nm
Finger length	1.35	mm
Spacing	8	μm
Path length	3.5	mm
Aperture	1.2	mm
Frequency f_0	114	MHz
Bandwidth B	2.85	MHz

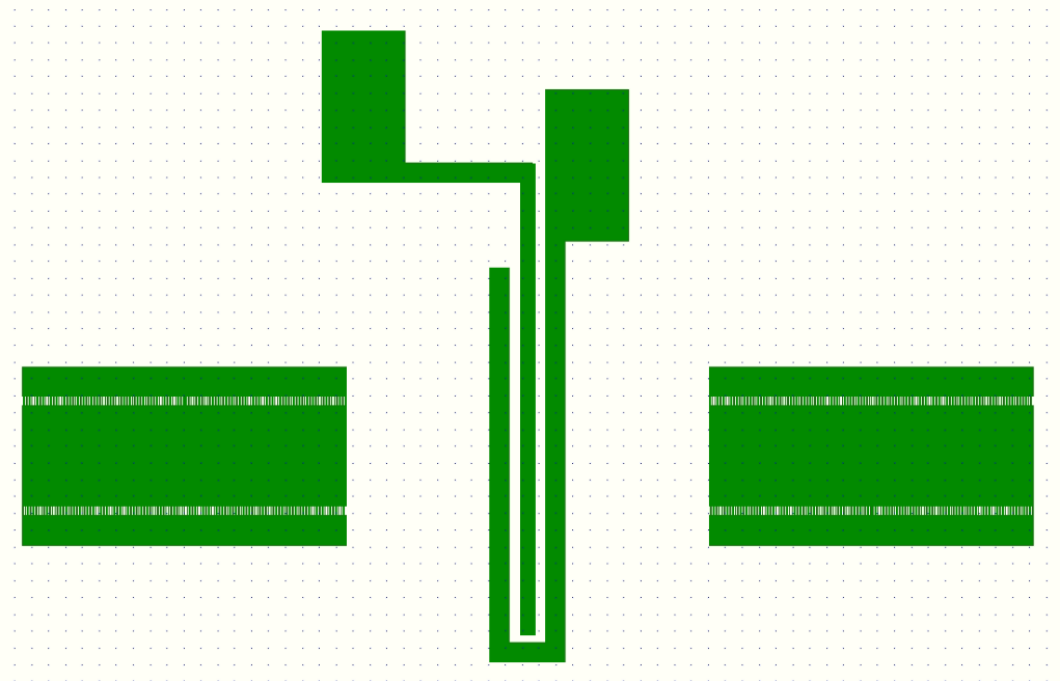

Figure 3.7: Delay line mask design

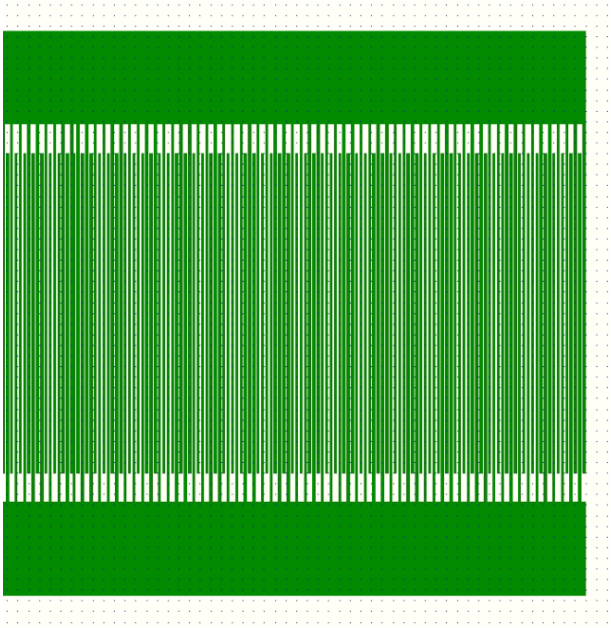

Figure 3.8

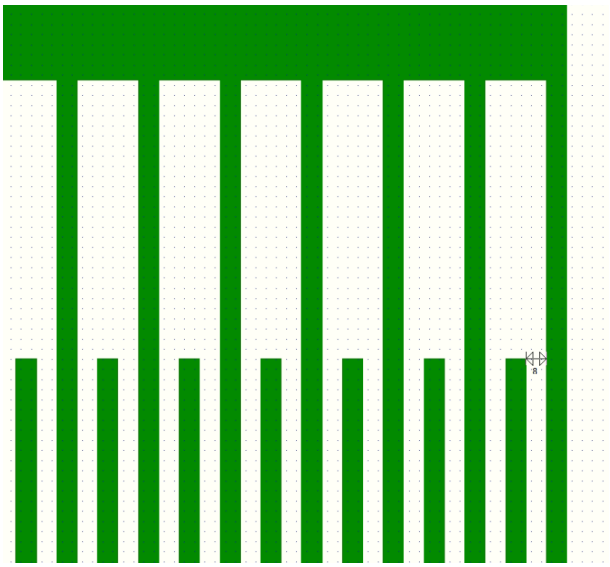

Figure 3.9: IDT zoom view

After the parameters definition, in order to predict the device behaviour, a delay line mathematical model has been implemented on Matlab. This model was proposed by Waldemar Soluch [92][93]. Starting from the equivalent circuit transfer function, admittances expressions are obtained and written in terms of the geometrical parameters of the line.

Figure 3.10: SAW delay line circuit schematic

Delay line transfer function can be written as

$$\frac{u_2}{V} = \frac{y_1 y_{12}}{y_{12}^2 - (y_1 + y_{11})(y_2 + y_{22})}$$

where y_1 and y_2 are respectively source and load admittances, y_{11} and y_{22} are the IDTs admittances and y_{12} represents the transfer admittance. Commonly the ratio $A_{12} = u_2/u_2^{'}$ is measured, where $u_2^{'}$ is the load voltage when the load is shorted with the source.

$$\frac{u_2^{'}}{V} = \frac{y_1}{y_1 + y_2}$$

By combining the latter equations A_{12} is obtained.

$$A_{12} = \frac{(y_1 + y_2) y_{12}}{y_{12}^2 - (y_1 + y_{11})(y_2 + y_{22})}$$

Insertion loss and group delay τ can be defined as

$$IL = -20\ log\,|A_{12}|$$

$$\tau = -\Phi\omega$$

A_{tt} can be defined as the ratio between triple transit signal TTS represented by y_{12}^2 and the product between admittances sum

$$A_{tt} = \frac{y_{12}^2}{(y_1 + y_{11})(y_2 + y_{22})}$$

and its logarithm is called suppression S_{tt},

$$S_{tt} = -20\ log\,|A_{tt}|$$

Employing some results from [4], the transfer admittance can be derived

$$y_{12} = 2Y_0 A_1 A_2 e^{-jkd}$$

where

$$A_i = \left[\frac{Y_{12}Y_{13} - Y_{23}(Y_0 + Y_{11})}{(Y_0 + Y_{11})^2 - Y_{12}^2} \right]_i$$

are the transfer admittance elements of IDT1 and IDT2, Y_0 is the SAW characteristic equivalent admittance, Y_{ij} are the elements of the admittance IDTs matrices and d is the distance between them. Y_{ij} can be derived by considering an IDT as a

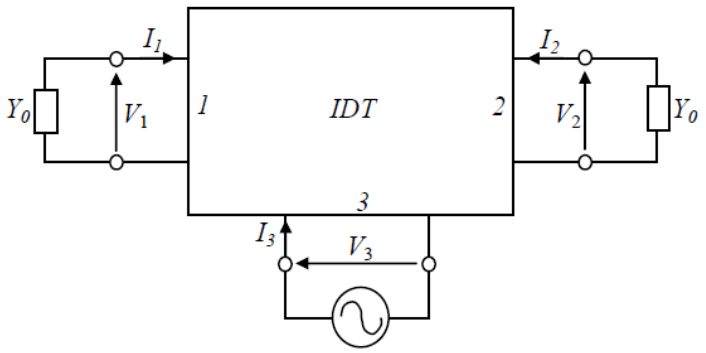

Figure 3.11: SAW delay line as a 3-port system

3-port system, two acoustic and one electrical port. Acoustic ports 1 and 2 are assumed to be located at the first ($x = -1/2$) and the last ($x = 1/2$) gap between electrodes, Applying a voltage V3 to the electrical port 3, equivalent voltages V^+ and V^- propagating in the positive and negative directions are generated. They can be written as

$$V^- = \sum_{n=1}^{N} v_n e^{jk(x-x_n)} \qquad for\ x \leq -1/2$$

$$V^+ = \sum_{n=1}^{N} v_n e^{-jk(x-x_n)} \qquad for\ x \geq 1/2$$

where v_n is the equivalent SAW voltage amplitude, generated by the n-th source, x_n is the n-th gap position and N is the number of gaps. Voltages V_1 and V_2 can be obtained evaluating V^- and V^+ at $x = \pm 1/2$

$$V_1 = \sum_{n=1}^{N} v_n e^{-jkx_n} e^{-jkl/2}$$

$$V_2 = \sum_{n=1}^{N} v_n e^{jkx_n} e^{-jkl/2}$$

Voltages v_n are then normalized to $\overline{V_0}$, becoming

$$V_1 = \overline{V_0} H e^{-jkl/2}$$

$$V_2 = \overline{V_0} H^* e^{-jkl/2}$$

where

$$H = \sum_{n=1}^{N} a_n e^{-jkx_n}$$

with $a_n = v_n/\overline{V_0}$ and H^* being H complex conjugate.

Equivalent port currents can be determined through

$$I_1 = Y_{11}V_1 + Y_{12}V_2 + Y_{13}V_3$$

$$I_2 = Y_{21}V_1 + Y_{22}V_2 + Y_{23}V_3$$

$$I_3 = Y_{31}V_1 + Y_{32}V_2 + Y_{33}V_3$$

When the electrical port 3 is shorted ($V_3 = 0$, the IDT can be considered a uniform lossless transmission line of length l, leading to $V_2 = V_1 e^{-jkl}$. Since port 1 and port 2 are loaded by an impedance $1/Y_0$, $V_1 = I_1/Y_0$ and $V_2 = -I_2/Y_0$, moreover

$$Y_{11} = -jY_0/tan(kl)$$

$$Y_{12} = -jY_0/sin(kl)$$

Instead when ($V_3 \neq 0$, $V_1 = -I_1/Y_0$ and $V_2 = -I_2/Y_0$, which lead to

$$Y_{13} = -\frac{V_1(Y_0 + Y_{11})}{V_3} - \frac{Y_{12}V_2}{V_3}$$

$$Y_{23} = -\frac{Y_{12}V_1}{V_3} - \frac{V_2(Y_0 + Y_{11})}{V_3}$$

Going back to the transfer admittance y_{12} definition, it can be rewritten as

$$y_{12} = G_0 H(\omega)$$

G_0 is a conductance which can be expressed as

$$G_0 = 2Y_0(\overline{V_0}/\overline{V_3})^2$$

and $H(\omega)$ is defined as

$$H(\omega) = H_1^*(\omega) H_2(\omega) e^{-j(k_t(l_1+l_2)/2 + k_f d)}$$

and

$$H_1^*(\omega) = \sum_{n=1}^{M_1} a_{1n} e^{jk_t x_{1n}}$$

$$H_2(\omega) = \sum_{n=1}^{M_2} a_{2n} e^{-jk_t x_{2n}}$$

M_i are IDTs gaps number, a_{in} are the transversal filter coefficients and x_{in} are the positions of the gaps. Wavenumbers k_f and k_t are the ratios between angular frequency and SAW velocities. However the description can be simplified employing infinite array approximation [94]. The conductance G_1 at synchronous frequency and the static capacitance C_0 can be derived.

$$G_1 = G_0 N_s^2 = \omega_0 W(\epsilon_0 + \epsilon_p^T) F(s) K^2 N_s^2$$

where

$$F(s) = \left[\frac{sin(\pi s)}{P_{-s}(cos\Delta)} \right]$$

.

$s = 1/S_e$, where S_e is the electrodes number per electrical period, $\Delta = \pi a/L$ where a is the the electrodes width and L is the period. $P_{-s}(cos\Delta)$ is known as Legendre function. K^2 is the SAW electromechanical coupling coefficient, W is the aperture length, ϵ_0 is the vacuum dielectric constant, ϵ_p^T is the substrate effective dielectric constant, R_s is acoefficient depending on s and N_s is the number of gaps in which $a_n \neq 0$. In the single electrode IDT case, $s = 1/2$, $R_s = 1/2$ and $N_s = N$.

The equations

$$G_0 = \omega_0 W(\epsilon_0 + \epsilon_p^T) F(s) K^2 =$$

$$= 2Y_0(\overline{V_0}/\overline{V_3})^2$$

lead to

$$Y_0 = \omega_0 W(\epsilon_0 + \epsilon_p^T)/2$$

and

$$(\overline{V_0}/\overline{V_3})^2 = F(s)K^2$$

Assuming constant period p and gaps width equal to $a = p/2$, G_0 can be written as [4]

$$G_0 = 2.443 f_0 W(\epsilon_0 + \epsilon_p) K^2$$

with ϵ_p effective dielectric permittivity

The static capacitance C_s can be computed as

$$C_s = 0.707 W(\epsilon_0 + \epsilon_p)$$

The SAW velocity in the IDT area v_t is

$$\frac{v_f}{1 + 0.85(v_f - v_m)/v_m}$$

in which f and m subscripts mean free and metallized.

y_{11}, y_{22} and y_{12} expressions are

$$y_{11} = G_1 + j(B_1 + \omega C_{01})$$

with

$$G_1 = G_0 N_1^2 \left[sin(X_1)/X_1\right]^2$$
$$B_1 = G_0 N_1^2 \left[sin(2X_1) - 2X_1\right]/(2X_1^2)$$
$$C_{01} = N_1 C_s$$

Similarly for y_{22}, G_2, B_2 and C_{02}. While

$$y_{12} = G_0 N_1 N_2 \left[sin(X_1)/X_1\right] \left[sin(X_2)/X_2\right] e^{-j\omega\tau_0}$$

where

$$X_i = \pi N_i (f - f_0)/2f_0$$

and the time delay between IDTs τ_0 is

$$\tau_0 = \frac{(l1 + l2)}{2v_t} + \frac{d}{v_f}$$

Finally

$$G_0 = G_p W/\lambda$$

where

$$G_p = 2.443 v_t (\epsilon_0 + \epsilon_p) K^2$$

This procedure has been implemented in a Matlab script, using the design parameters as input data. Frequency response and admittances plots are then reported.

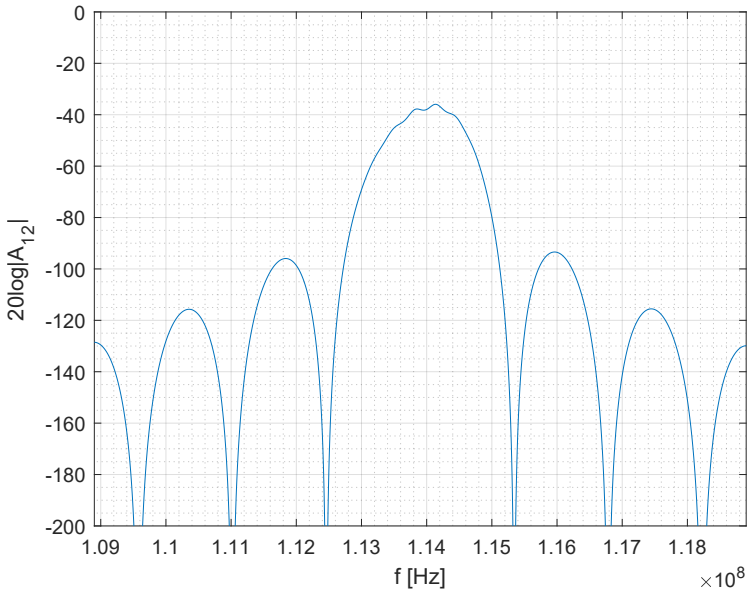

Figure 3.12: Delay line frequency response

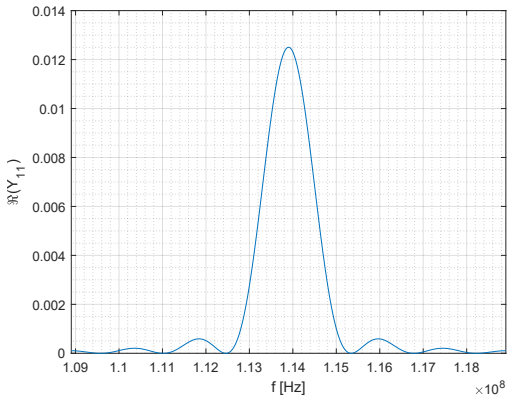

Figure 3.2 : Real part of Y11 admittance

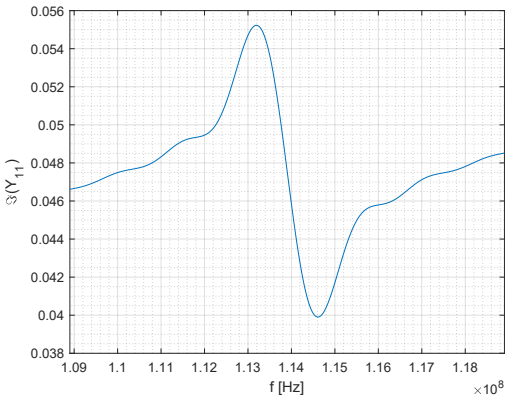

Figure 3.3 : Imaginary part of Y11 admittance

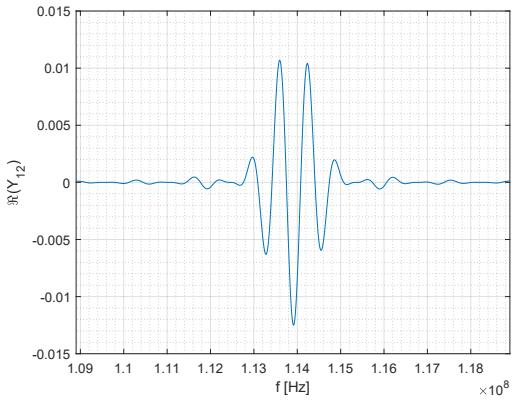

Figure 3.4 : Real part of Y12 admittance

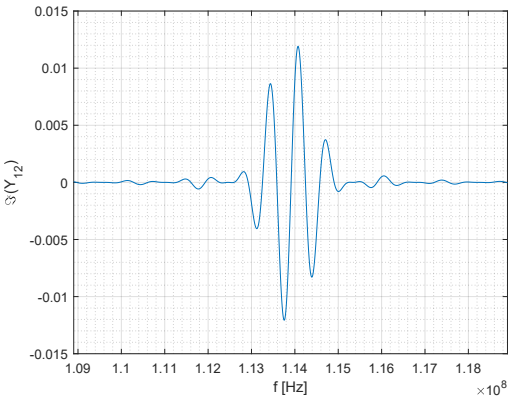

Figure 3.5 : Imaginary part of Y12 admittance

Chapter 4

Simulations, Experimental and Results

4.1 Simulations

4.1.1 COMSOL Multiphysics

COMSOL Multiphysics is a finite element based software, useful to solve complex physics problems, generally involving PDEs. It consists of several modules which allow to model various physical phenomena. Moreover, these modules can be coupled together to create a multiphysics environment. Thanks to preset physics interfaces, governing equations can be automatically included into the model. Following steps are required to create a COMSOL model:

- definition of the number of spatial dimension and the choice of physics modules and study types.
- geometry definition, either by creating it using predefined building blocks or by importing it.
- domains assignation to the various interfaces.
- boundary conditions definition.
- materials assignation, which can be either predefined or custom.
- mesh definition, which can be accomplished by using different shaped elements and size settings.
- studies settings definition, such as the operating range and the solver settings.

- post-processing and visualization of the results.

Piezoelectric materials can be simulated in COMSOL by using Structural Mechanics module, MEMS module or acoustic module. The predefined Piezoelectric Devices interface, provided by each of these modules, can be used to model systems including both piezoelectric and structural materials. By selecting Piezoelectric Devices interface, its constituent physics Solid Mechanics and Electrostatics become available. Moreover, the Piezoelectric Effect branch is added to the Multiphysics node, coupling the latter nodes.

All domains must be assigned to Piezoelectric Material branch or to Linear Elastic Material, according to their nature. Similarly, the former ones are assigned to Charge Conservation Piezoelectric branch, while the latter ones to the Charge Conservation branch.

The Solid Mechanics node provides high flexibility into modeling systems which involve piezoelectric, linear and nonlinear structural materials. Even if these different domains get into contact, the software takes into account continuity conditions across them automatically. This model allows also to assign mechanical constraints and loads to the model parts.

The Electrostatics node contains all the electrical inputs and boundary conditions of the model. They can be voltage or charge sources, electric terminal, added capacitances and others.

The Multiphysics - Piezoelectric Effect branch imposes the coupling of the equations belonging to both nodes, which are solved together for every domain assigned Piezoelectric Material branch [95].

4.1.2 Model Description

Delay lines on $LiNbO_3$ 128°YX have been modeled in COMSOL Multiphysics. Several structures with different geometrical parameters such as number of finger pairs, distance between electrodes, acoustic aperture, substrate and fingers dimensions have been simulated. Also mesh structures have been varied, along with the boundary conditions. Analysis in time and frequency domain have been conducted and data have been post-processed to obtain outputs comparable with experimental device measurements.

It has been chosen to model the device in 2D because when the ratio between fingers length and the wavelength is large enough, the bidimensional approximation well describe the problem. This choice comes with the advantage of an extreme simplification of the model [96].

In this work, Au IDTs have been built with a 50% metallization ratio and two pitch dimensions: 4 μm and 8 μm. Fingers have been modeled as 50 nm thick rectangular blocks. The acoustic aperture which is not visible in the 2D view has been specified as 1.2 mm inside the Solid Mechanics and Electrostatics physics nodes.

Geometries

Structures have been built within the COMSOL software using rectangular blocks Three geometries are presented in this work:

- dummy delay line: a structure built to be practical and simple. It is characterized by having only a transmitter IDT and a receveir IDT, a distance between IDTs of 1 mm, a substrate thickness of 100 μm and only 10 finger pairs. These choices heavily reduce nodes number and so the degrees of freedom of the problem, leading to lower complexity.

- dual delay line: a structure mainly designed to observe the symmetric superficial propagation and eventually to obtain differential results by modifying the characteristics of one path. It consists of three IDTs: the central one which transmits the signal and the side ones which receive it. This structure has been simulated in its 10-finger pairs version, due to its high number of nodes which derives from its length. Each IDT is separated by 3 mm from the others, resulting in a long substrate.

- single delay line: it is the structure which is more similar to the experimental devices. It employs two IDTs, each one having 80 pairs of fingers placed at a distance of 3.5 mm or 4.3 mm.

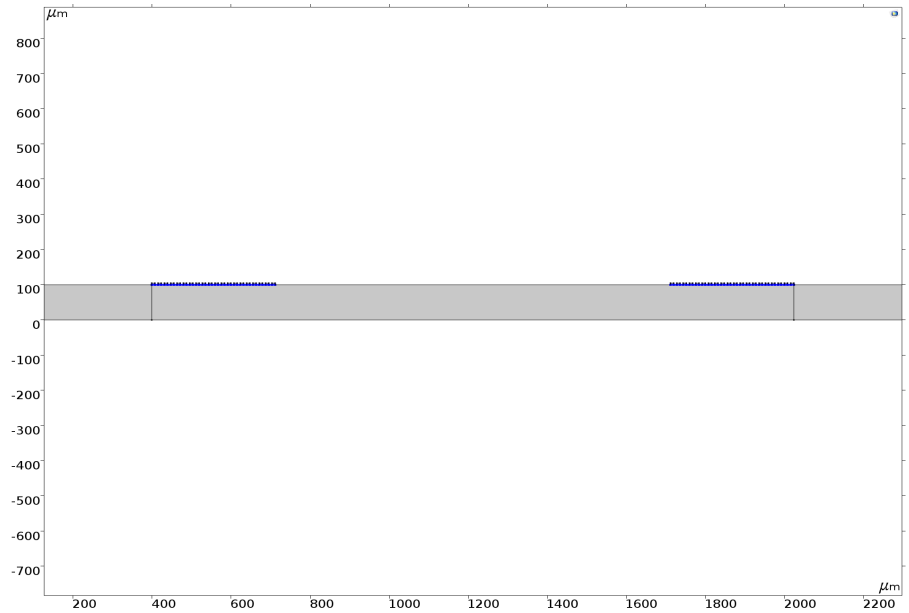

Figure 4.1: Dummy delay line structure

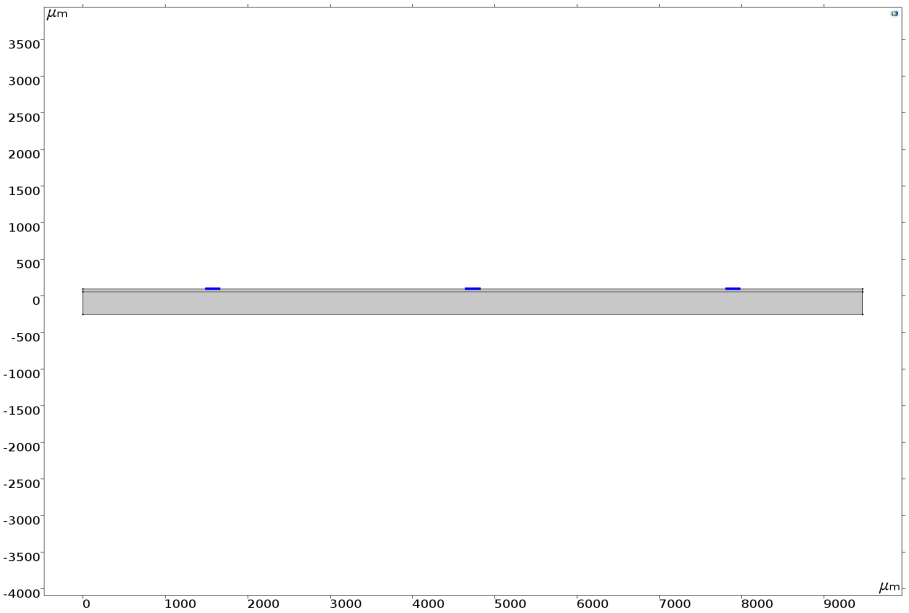

Figure 4.2: Dual delay line structure

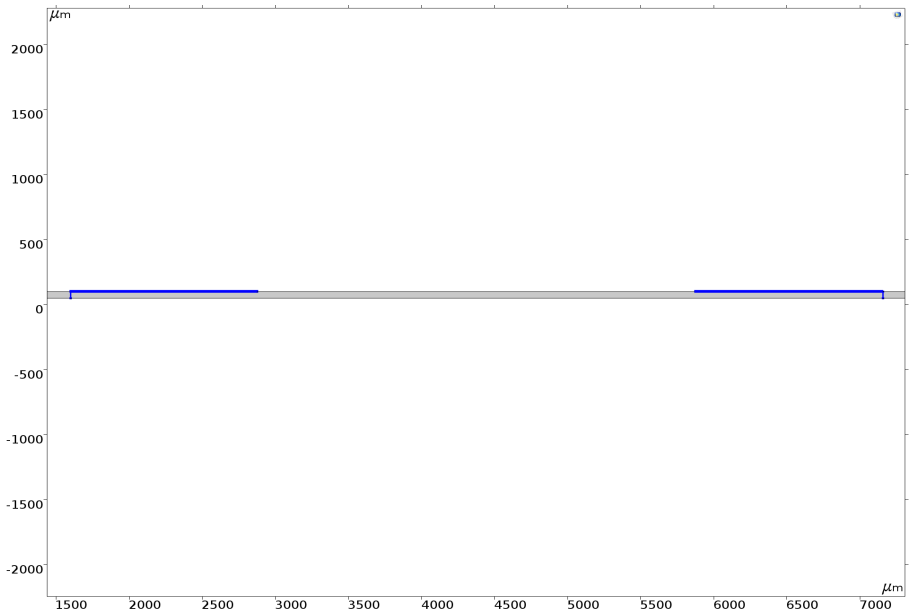

Figure 4.3: Single delay line structure

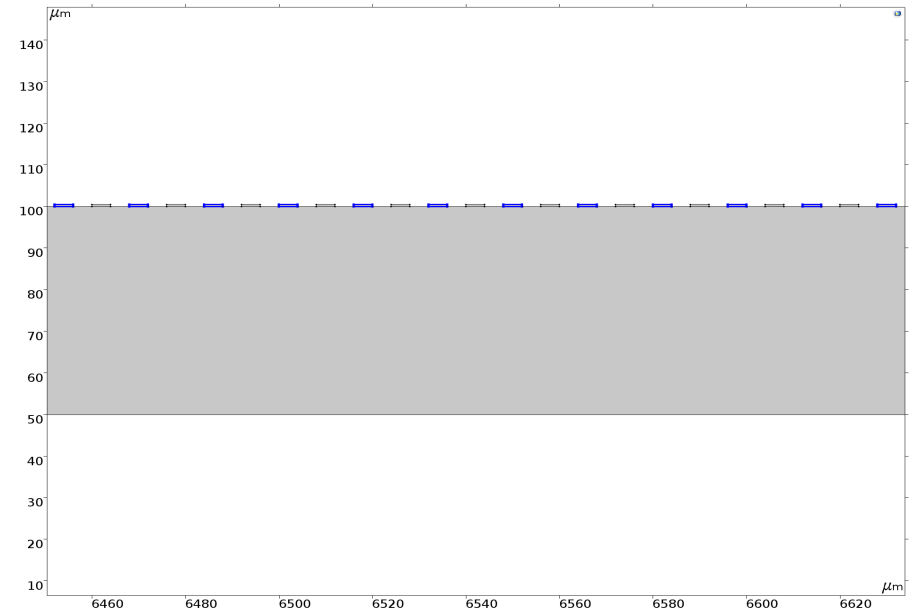

Figure 4.4: Zoom on the IDT of the single delay line structure

Materials

Materials employed in this work are the $LiNbO_3$128°YX as substrate and Gold as IDTs metal. In particular for the $LiNbO_3$, two different orientation have been modeled: the x-parallel and the x-perpendicular one, each one defined by their Euler Angles. A set of Euler angles(Φ, Θ, Ψ) uniquely define a crystal cut. By denoting the crystal axis as (X,Y,Z) and following the XYX notation, the first angle Φ represents a rotation about the X axis, the second angle Θ a rotation about the rotated y' axis and the third angle Ψ a final rotation about the rotated x' axis. In this notation, Euler angles are (38°, 180°, 0°) for the x-parallel orientation and (38°, 0°, 0°) for the x-perpendicular one [96].

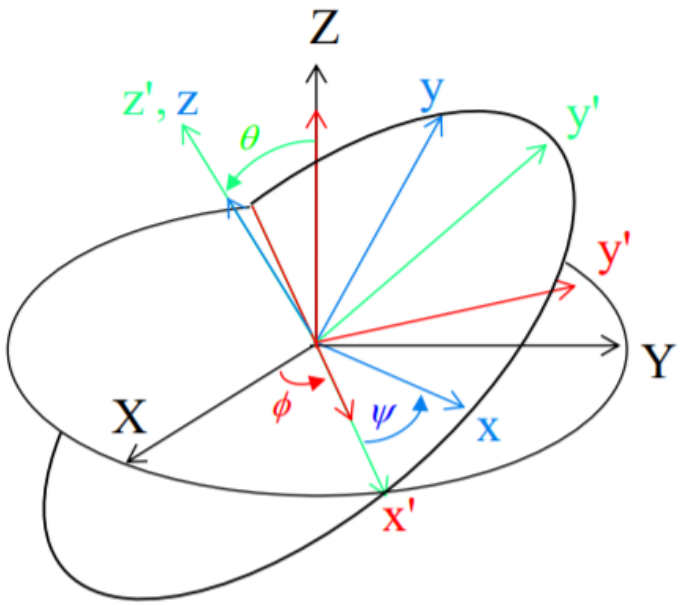

Figure 4.5: ZXZ rotation by Euler angles (Φ, Θ, Ψ)

To define on COMSOL an anisotropic piezoelectric material such as the $LiNbO_3$128°YX, elasticity matrix c^E, coupling matrix e^{ES} and relative permittivity matrix ϵ^S must be provided. In literature these data are reported for the "unrotated" (0°, 0°, 0°) substrate. In order to obtain the parameters for the two orientations, the Bond transformation must be applied to the original matrices. Bond transformation is a technique in which rotated matrices are obtained through multiplication of the original matrices by rotation matrices, generated according to the wanted Euler angles. For each orientation, two matrices a and M are created and then original matrices c^E, e^{ES} and ϵ^S are multiplied from left and right by them [97][98].

$$c' = M\ c\ M^T$$

$$e' = a\ e\ M^T$$

$$\epsilon' = a\ \epsilon\ a^T$$

where

$$\mathrm{M} = \begin{pmatrix} a_{xx}^2 & a_{xy}^2 & a_{xz}^2 & 2a_{xy}a_{xz} & 2a_{xz}a_{xx} & 2a_{xx}a_{xy} \\ a_{yx}^2 & a_{yy}^2 & a_{yz}^2 & 2a_{yy}a_{yz} & 2a_{yz}a_{yx} & 2a_{yx}a_{yy} \\ a_{zx}^2 & a_{zy}^2 & a_{zz}^2 & 2a_{zy}a_{zz} & 2a_{zz}a_{zx} & 2a_{zx}a_{zy} \\ a_{yx}a_{zx} & a_{yy}a_{zy} & a_{yz}a_{zz} & a_{yy}a_{zz} + a_{yz}a_{zy} & a_{yx}a_{zz} + a_{yz}a_{zz} & a_{yy}a_{zx} + a_{yx}a_{zy} \\ a_{zx}a_{xx} & a_{zy}a_{xy} & a_{zz}a_{xz} & a_{xy}a_{zz} + a_{xz}a_{zy} & a_{xx}a_{zx} + a_{xx}a_{zz} & a_{xx}a_{zy} + a_{xy}a_{zx} \\ a_{xx}a_{yx} & a_{xy}a_{yy} & a_{xz}a_{yz} & a_{xy}a_{yz} + a_{xz}a_{yy} & a_{xz}a_{yx} + a_{xx}a_{yz} & a_{xx}a_{yy} + a_{xy}a_{yx} \end{pmatrix}$$

and

$$a = \begin{pmatrix} a_{xx} & a_{xy} & a_{xz} \\ a_{yx} & a_{yy} & a_{yz} \\ a_{zx} & a_{zy} & a_{zz} \end{pmatrix} =$$

$$= \begin{pmatrix} cos(\Theta) & sin(\Theta)sin(\Psi) & sin(\Theta)cos(\Psi) \\ sin(\Phi)sin(\Theta) & cos(\Phi)cos(\Psi) - cos(\Theta)sin(\Phi)sin(\Psi) & -cos(\Phi)sin(\Psi) - cos(\Theta)cos(\Psi)sin(\Phi) \\ -cos(\Phi)sin(\Theta) & cos(\Psi)sin(\Phi) + cos(\Phi)cos(\Theta)sin(\Psi) & cos(\Phi)cos(\Theta)cos(\Psi) - sin(\Phi)sin(\Psi) \end{pmatrix}$$

Finally, Gold material has been selected in the COMSOL materials library and it has been applied to fingers domains.

Boundary conditions

The models are defined by the Piezoelectric Devices interface, made up of the Solid Mechanics, the Electrostatics physics and the Piezoelectric Effect Multiphysics node. Each physic node comes with default features but it is possible to personalize them by adding custom subnodes, which can be of different nature such as domain, boundary, edge, point or pairs. In both physics an out-of-plane thickness of 1.2 mm has been defined.

Solid Mechanics interface allows to approach structural analysis problems of various nature, solving motion equations along with solid material constitutive model and computing quantities such as stresses, strains and displacements. Solid Mechanics employed nodes are:

- Linear Elastic Material: node which adds linear elastic solid material equations. It also provides an interface to define materials properties. Several subnodes such as Thermal Expansion, External Stress, Strain and Viscoelasticity can be incorporated to include different effects. When another material property node such as Piezoelectric Material one is added, it is overridden by it.

- Free: node applied by default to all the boundaries where no constraints or load acts. When such nodes are added, this node is overridden by them.

- Initial Values: node that sets initial conditions for displacement and structural velocity fields. It can be used as initial condition in a transient simulation or as initial estimation for particular problems.

- Piezoelectric Material: node applied to the piezoelectric substrate that defines material properties in stress-charge or strain-charge form. Subnodes such as Coupling Loss, Dielectric Loss and Mechanical Damping can be added to model different effects. The latter subnode is included in this work to model mechanical losses in Rayleigh damping form.

- Fixed Constraint: node applied to the bottom boundary of the structure, it makes the entity fully constrained which means that displacements and rotational degrees of freedom will be null in any directions.

- Added Mass: node applied to the sensing layer domain, used to model an inertia that is not part of the material itself. It can be defined as mass density or as total mass.

Electrostatics interface is intended to compute potential distributions, electric and electric displacement fields. It solves the electric field Gauss' law, in which electric potential is the dependent value. Electrostatics employed nodes are:

- Charge Conservation: node which includes in the model the equations for electric displacement field, according to Gauss' law. It comes with an interface that allows to define constitutive relations and associated material properties. It is initially applied to all the domains, then if another charge conservation subnode such as Charge Conservation Piezoelectric one is added, it is overridden by this latter.
- Zero Charge: node that defines the boundary conditions of null electric charge where it is applied. It is applied by default to exterior boundaries but it is overridden by Terminal and Ground subnodes.
- Initial Values: node which sets initial conditions for the electric potential. It can be used as initial condition in a transient simulation or as initial estimation.
- Electric Potential: node that provides a predetermined electric potential to the selected boundaries. It allows to insert an expression which can be time-dependent. Because of this feature, it is applied to the transmitter IDT boundaries in the transient simulations.
- Terminal: node that provides a specified voltage or charge to the selected buondaries or domain. It can also be used for external circuit or transmission lines connections. Terminal types can be selected as Charge, Voltage, Circuit or Terminated. The Charge type Terminal imposes the boundary deposited total charge and when the value is set to zero, it corresponds to an uncharged floating electrode condition. This kind of conditions has been used in this work.
- Ground: node that imposes a zero potential conditions at boundary at which is applied. It is assigned to the grounded electrodes.

Meshes

In COMSOL the geometry discretization into small elements is performed by means of a meshing sequence, made up of meshing operations and attributes. Domains are discretized into triangular o quadrilateral smaller intervals. Mesh can be unstructured, which is also called free mesh and can be used for all kinds of geometries, or structured in which all mesh vertices are in contact with the same number of elements and a more regular structure is required. Different shaped element generator are provided by the software, whose properties can be modified by means of Size and Distribution nodes. Many types of meshing elements and dimensions have been investigated during this work. However it has been reported that in wave-type problems, in order to obtain an acceptable solution there must be at least five mesh elements per wavelength. To fully satisfy this requirement and because of the regularity of the structure, a mapped mesh has been chosen. In particular, it has been used a mapped mesh, that is a quadrilateral structured mesh. This kind of mesh requires that opposite sides of each domain have the same number of edge element. In order to guarantee such a requirement, Distribution subnodes have been applied to the external boundaries to impose the wanted number of elements in each edge [99][100]. The mesher then maps a grid employing a technique called transfinite interpolation. The result is a regular grid made up of perfectly equal squared elements. It has been chosen to use 2 μm as dimension for the size of the squared elements sides for the models in which the wavelength is 16 μm and 4 μm for those models with a 32 μm wavelength.

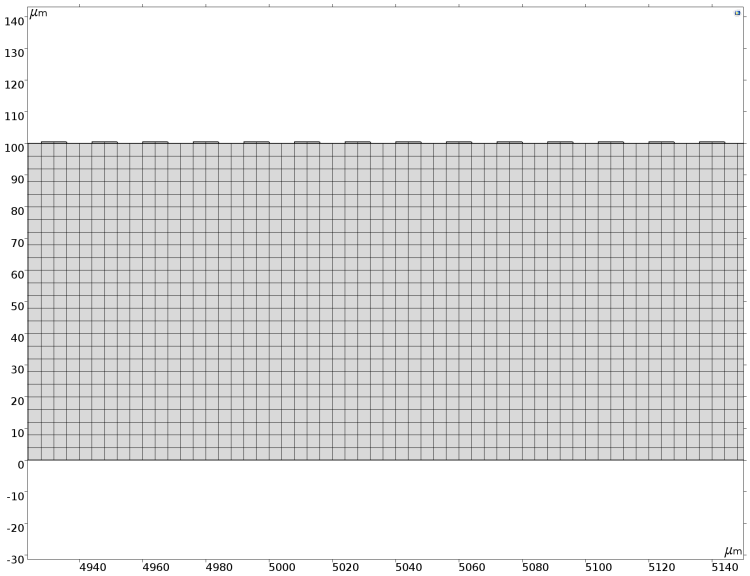

Figure 4.6: Meshed structure

4.1.3 Eigenfrequency study

Eigenfrequencies are discrete natural frequencies at which a system is inclined to vibrate. While ideal infinite solids can freely vibrate at any frequency, finite ones only vibrate freely at these frequencies. These frequency values make the motion equations to be satisfied by the boundary conditions, resulting in standing waves. They are present in many different systems, such as resonant circuits, mechanical structures and acoustic devices. In mechanical structures, it is called eigenmode the shape in which the structure deforms when it is vibrating at the eigenfrequency value [101]. Eigenfrequency analysis has been conducted to ascertain the resonance of the system at the wanted operating frequency, to verify the shape of the deformation in the substrate and to investigate the way in which geometrical parameters affect them.

The analysis has been performed over the elementary cell of the IDT structure, consisting in portion of substrate one wavelength long i.e. 32 μm and 3 wavelength high. Periodic Condition node has been applied to the side edges of the structure in order to provide continuity between the two walls. Two electrodes have been built on top of the substrate portion, one assigned to the Floating Potential node and the other assigned to the Ground node. Both X-parallel and X-perpendicular orientation of the LiNbO3 substrate have been simulated. Eigenfrequencies have been searched around the theoretical operating frequencies. The results show the Rayleigh eigenmodes in both orientations as expected. X-parallel device has a Rayleigh mode at 121.56 MHz, corresponding to a 3889 m/s velocity, and the X-perpendicular one at 113.68 MHz i.e. a velocity of 3637 m/s. Moreover, the eigenfrequency values lead to surface waves velocities which match theoretical and experimental ones, guaranteeing that orientations are correctly defined.

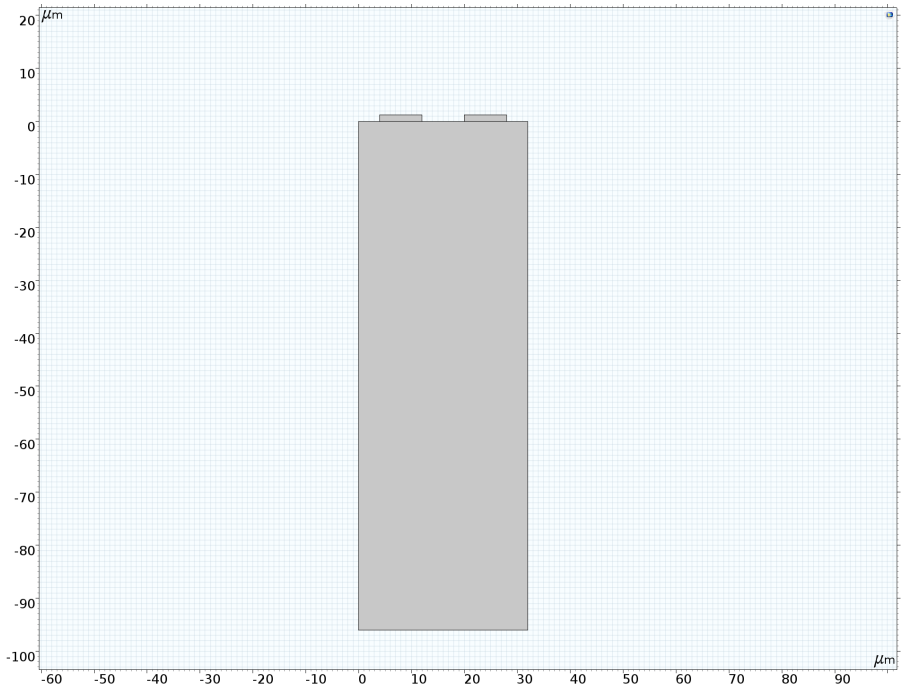

Figure 4.7: Elementary cell structure

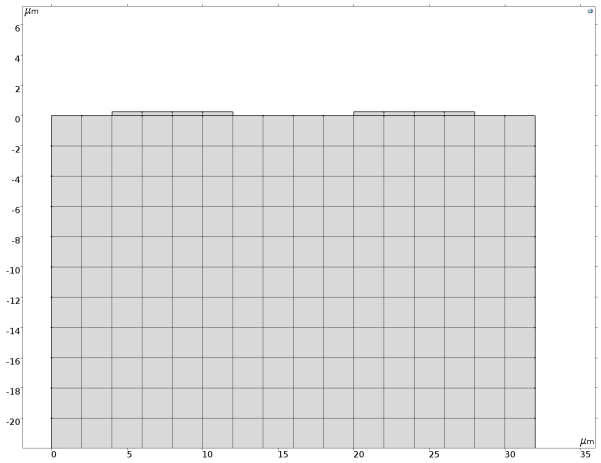

Figure 4.8: Elementary cell mesh

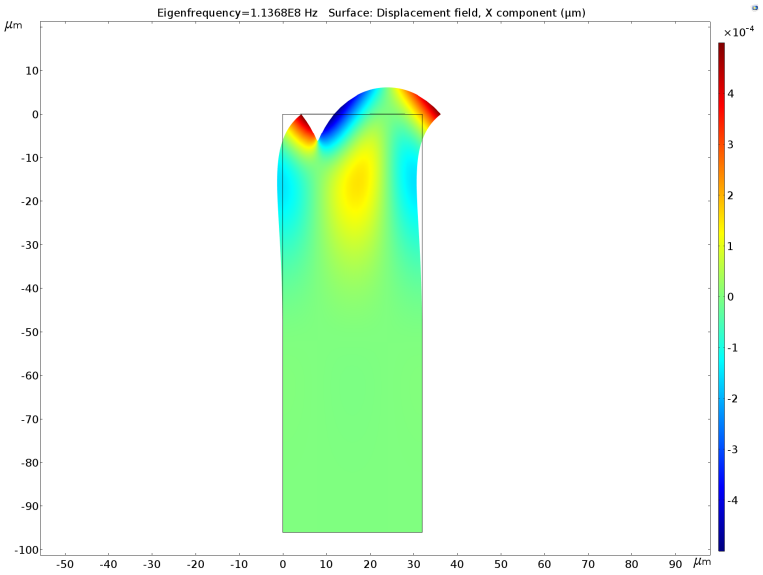

Figure 4.9: Horizontal displacement, X-perpendicular orientation

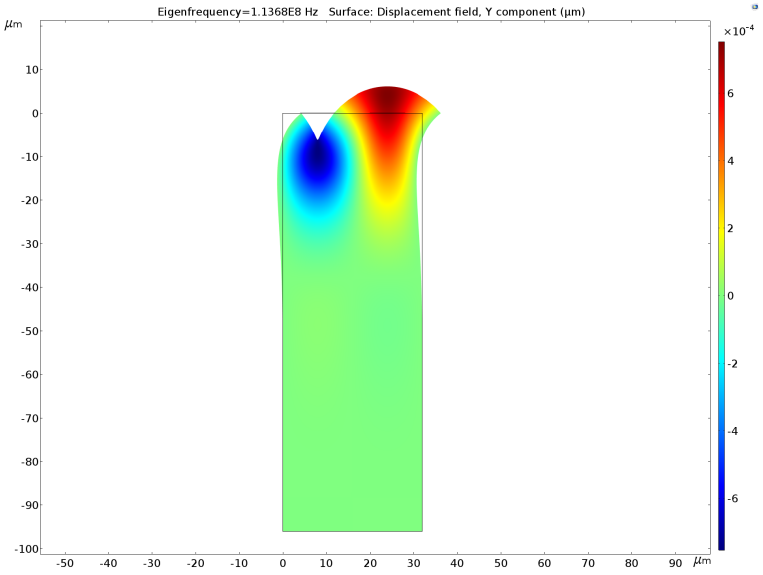

Figure 4.10: Vertical displacement, X-perpendicular orientation

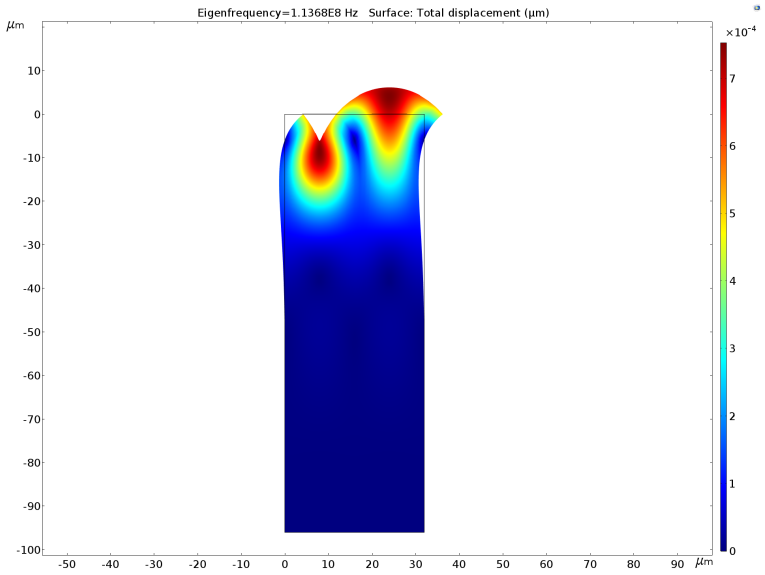

Figure 4.11: Global displacement, X-perpendicular orientation

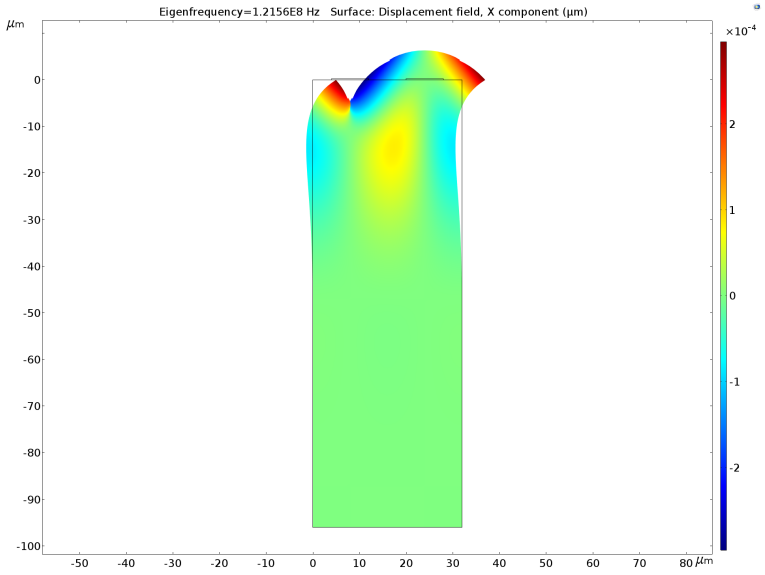

Figure 4.12: Horizontal displacement, X-parallel orientation

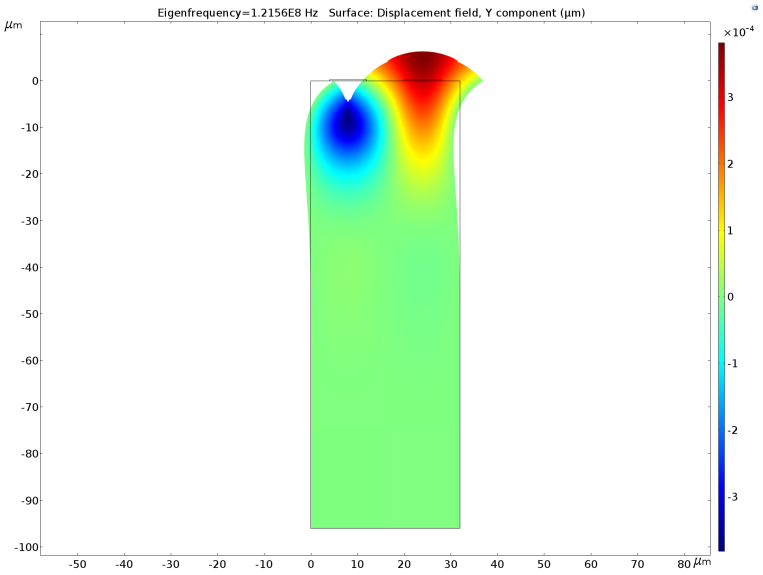

Figure 4.13: Vertical displacement, X-parallel orientation

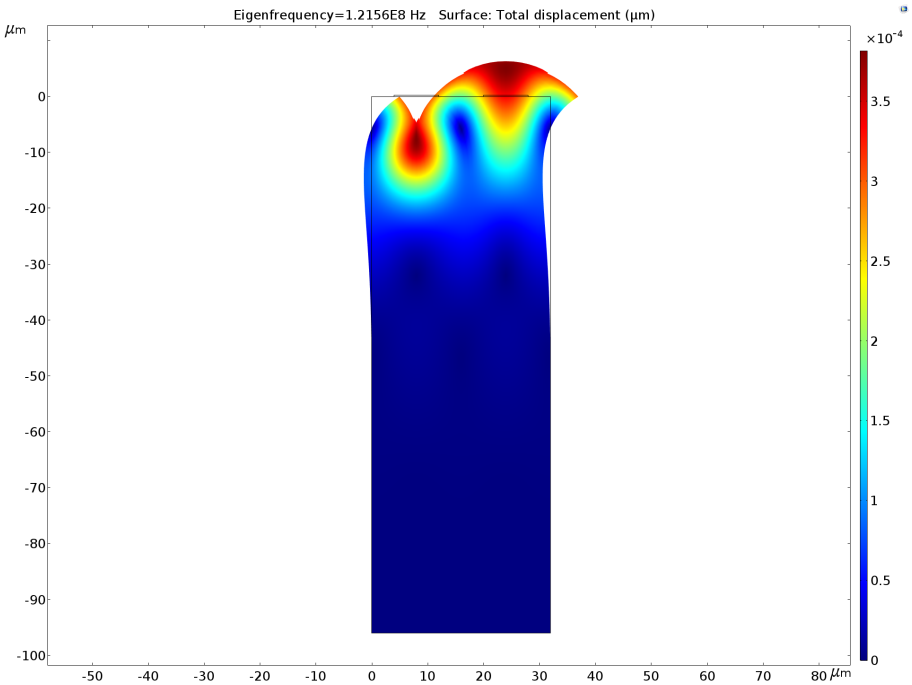

Figure 4.14: Total displacement, X-parallel orientation

4.1.4 Time domain study

Time domain analysis have been performed in order to monitor the time evolution of the system, from the instant in which the input signal starts to the one in which waves reach the receivers and over. They can provide a unique point of view on particular situation which could not be controlled in any other kind of study. For instance it can be visualized the reflections against the walls or the electrodes, with the further possibility to create animations in order to clearly understand critical dynamics.

Time-dependent analysis have been conducted on different structures. Transient simulations allow to use separated study steps to monitor time-varying voltages and mechanical deformations. The time evolution of the models has been observed for different input signals. Although their high complexity, due to the large time interval to be observed and to time stepping requirements, can limit the scope of such analysis.

Initially, the effects of mechanical damping have been investigated. On the dummy delay line, a 4 ns impulsive signal of amplitude 1 V is applied to the transmitter IDT and the received signal on the other IDT is observed. The simulation is performed for three values of damping, $\xi = 0, 0.001, 0.01$.

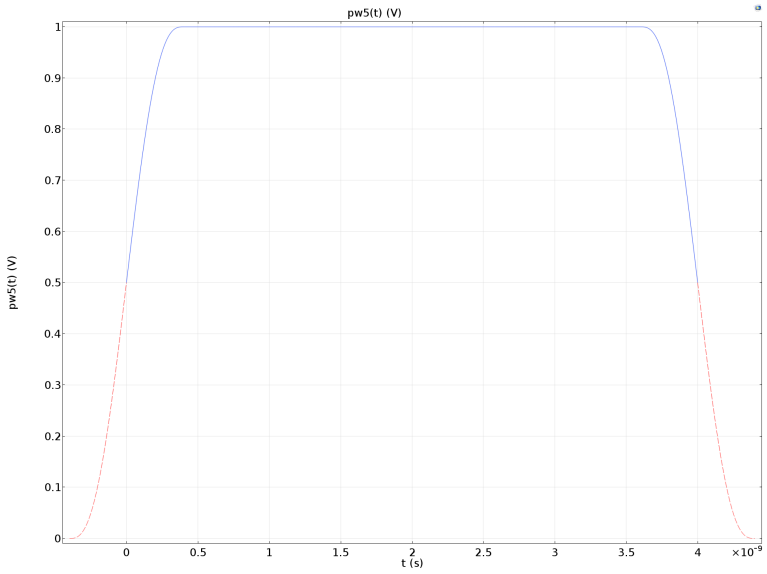

Figure 4.15: Impulsive input signal

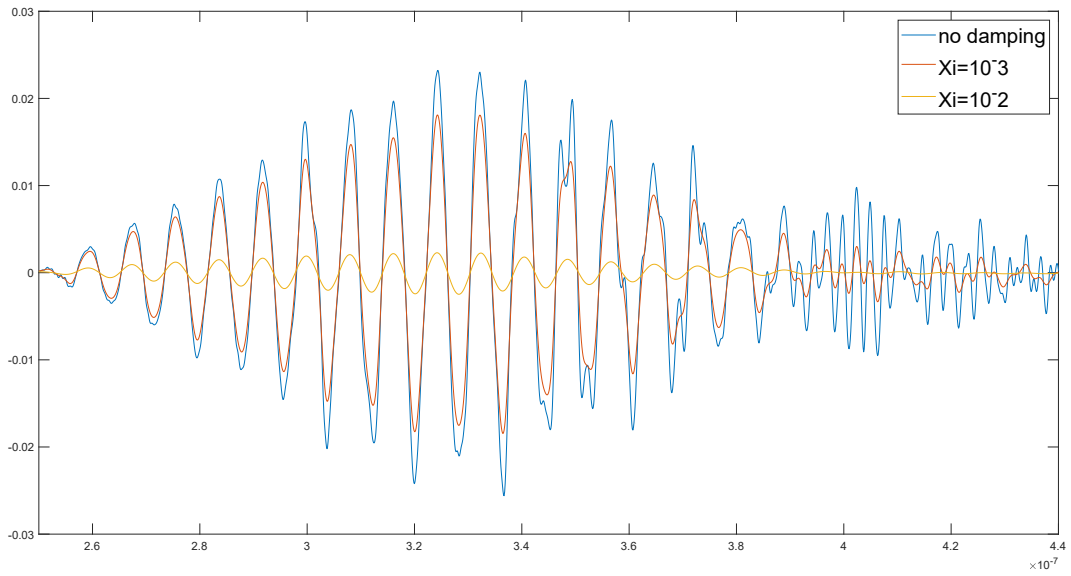

Figure 4.16: Comparison between received voltage signals with different mechanical damping values

From Fig. 4.16 it can be seen that the effect of the different damping value is to reduce the amplitude of the received signal proportionally. A mechanical damping ratio of $\xi = 0.001$ reduces the amplitude by the 21%, while a $\xi = 0.01$ by the 90%. The damping ratio $\xi = 0.001$ has been then adopted in the most of the models of this work.

The effect of the presence of an extra electrode among the IDTs and of the added mass domain built on it, has been then investigated. This should be a rough approximation of the sensing area made up of two electrodes and the MIP or NIP structures. The dummy structure has been implemented with two rectangular blocks of 168 μm length built in the middle of the sensing area, the one modelling the electrode having the same thickness of the fingers while the overlay is 20 nm thick. An added mass feature, defined as 10 times the Gold mass per unit volume, has been assigned to the overlay block to model a mass loading. Simulations have been conducted using input signal in Fig. 4.15, for the void line, the line in presence of the extra electrode and in presence of both the extra electrode and the MIP overlay. Results show an attenuation and a phase shift in both cases. The presence of the electrode makes the signal to be reduced by the 5%, with a shift of 0.6 ns. The added mass instead provokes an amplitude reduction of the 10%, with a time shift of about 3.2 ns.

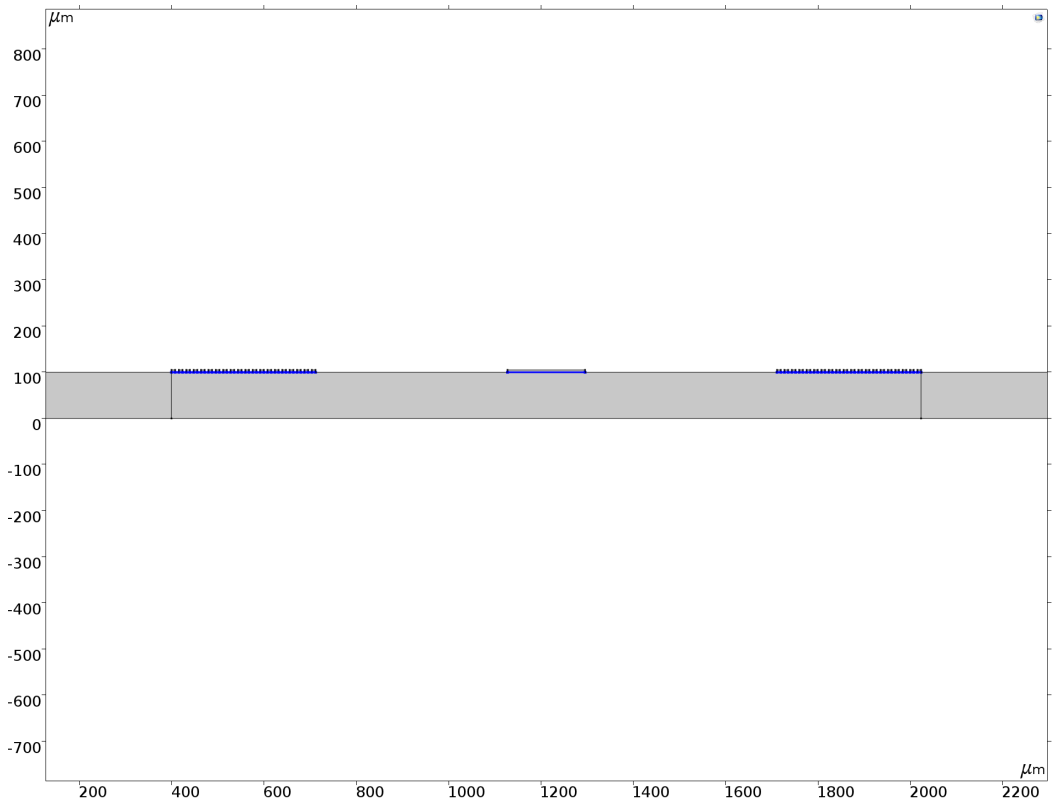

Figure 4.17: Dummy structure with MIP electrode and added mass domain

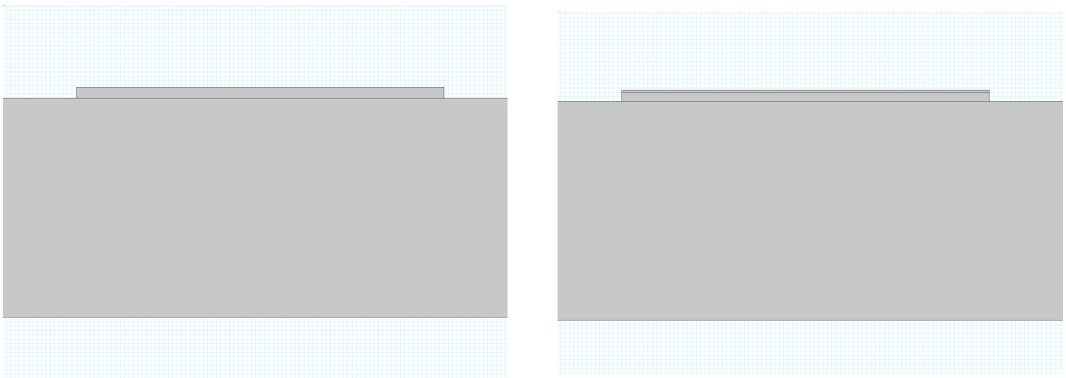

Figure 4.18: Zoom of MIP electrode and added mass domain

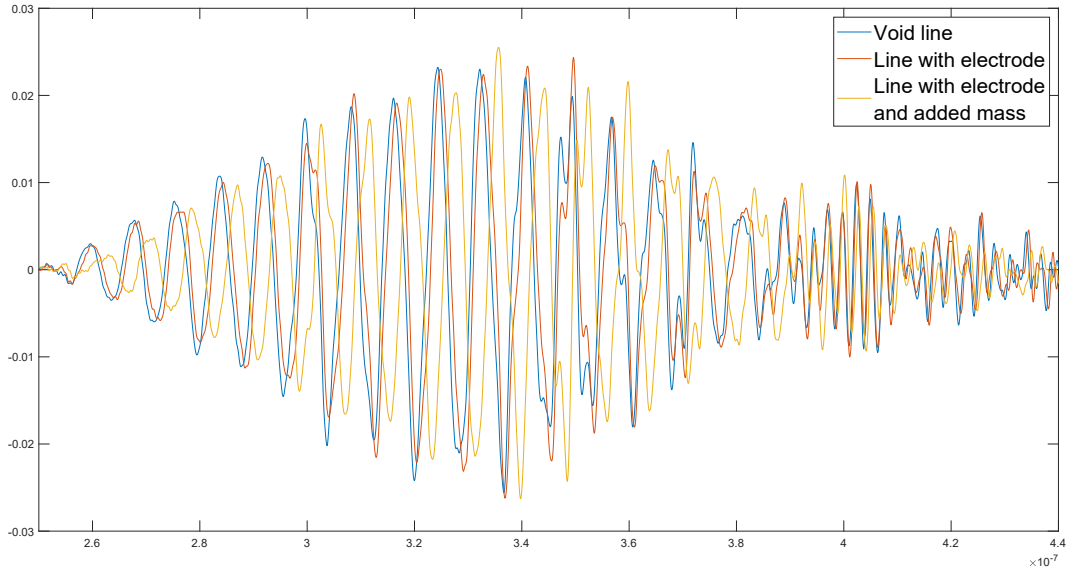

Figure 4.19: Comparison between received voltage signals with different line conditions

Transient analysis have been done on the two IDTs receivers line as well. Initially a 200 ns sine signal at the synchronous frequency of amplitude 1V has been employed as input signal. As it can be seen from Fig. 4.21, received voltages are almost perfectly overlapped. In the first 200 ns, an interference is present in the output signal, due to the electromagnetic feedthrough. When excited, the transmitter fingers radiate an electromagnetic field which is detected from the receivers, which act as antennas. After a time equivalent to the distance between transducers divided by the wave velocity, the output starts to follow the input signal. However the envelope of the output signal is not properly sampled. Moreover, the solution is not acceptable because of its time step dependence. In this simulation the time-dependent solver is allowed to decide the time step freely, which results in the fact that when a geometrical parameter is varied, time step will be chosen differently leading to the solution of the problem under different conditions.

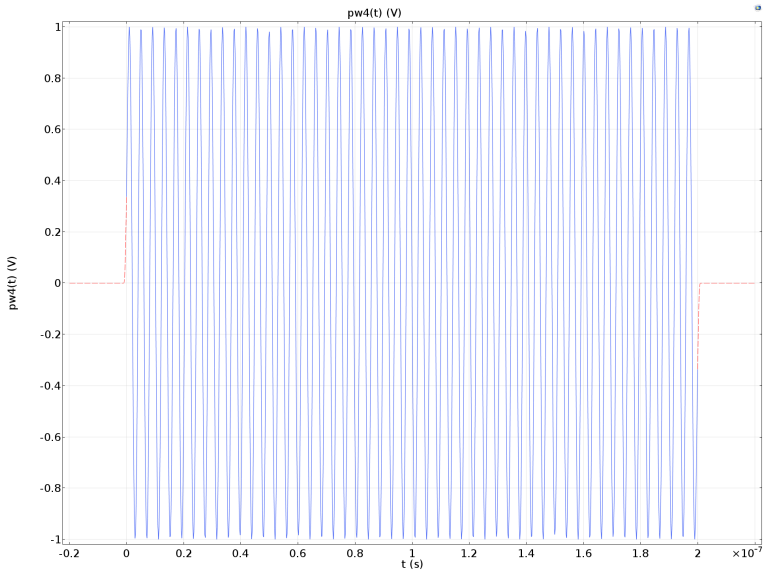

Figure 4.20: Sine input signal

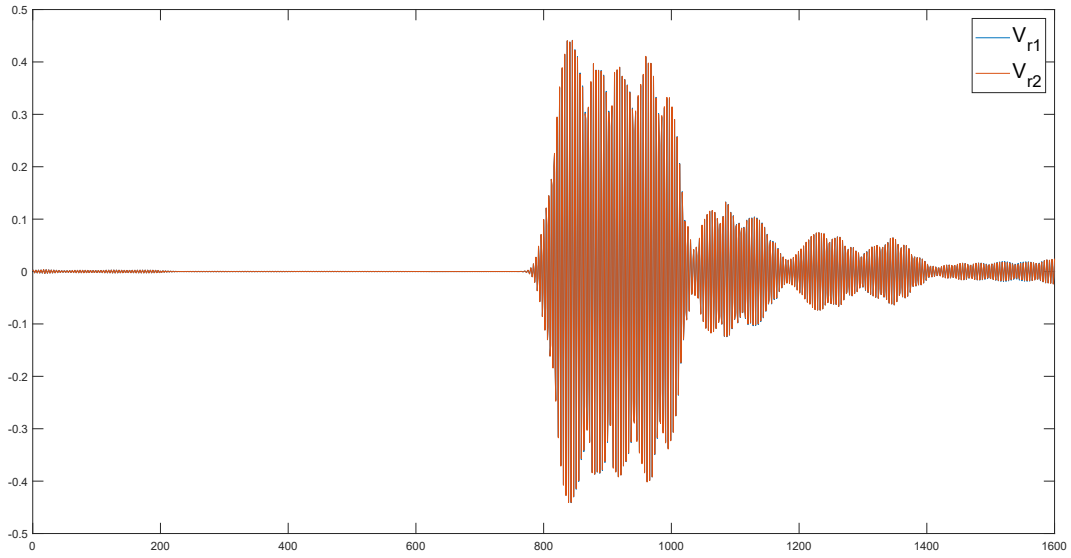

Figure 4.21: Dual line received voltage signal

In the next simulation, the time step is fixed and it is chosen according to the CFD condition [102]. The solver is now forced to take uniform time steps and compute the solution for each of them. The result is shown in Fig 4.22. Here, the envelope is well defined and it has constant amplitude in the central region.

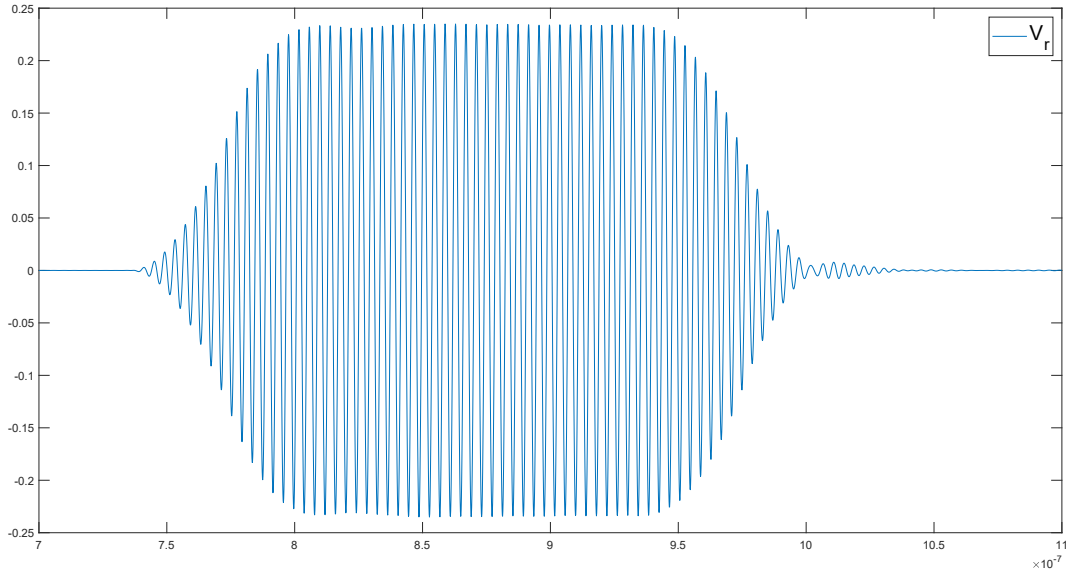

Figure 4.22: Received voltage signal when time step is specified

The surface deformation can be observed in Fig.4.23 and 4.24. Alternated portions of the substrate surface are moving either in the horizontal as well as in the vertical direction, in a Rayleigh wave propagation fashion. It can be appreciate that the displacement matches the horizontal periodicity of the transducer. Moreover waves are confined in a wavelength distance, in 16 μm.

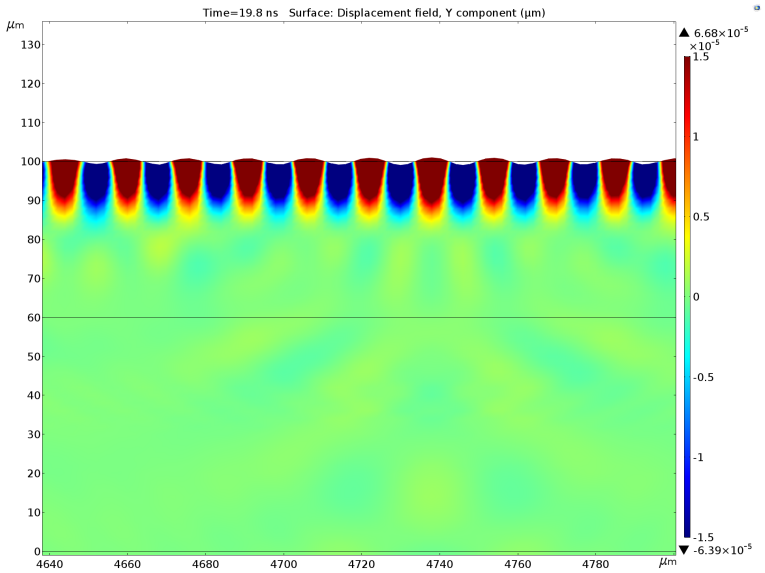

Figure 4.23: Zoom of vertical surface displacement at transmitter IDT

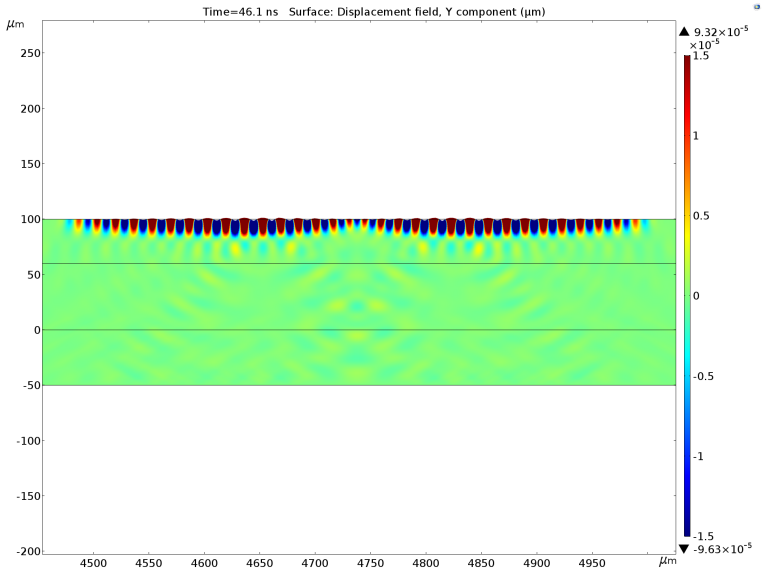

Figure 4.24: Symmetrical vertical surface displacement in opposite directions

Finally the 4 ns impulsive signal has been applied to the single delay line structure, made up of 80 pairs of fingers. Stored data points start from the instant in which the waves reaches the output transducer. This input signal has been chosen to obtain the impulse response of the system. Moreover, it may be provided by a simple control system, eliminating the need of special instrumentation such as network analyzers.

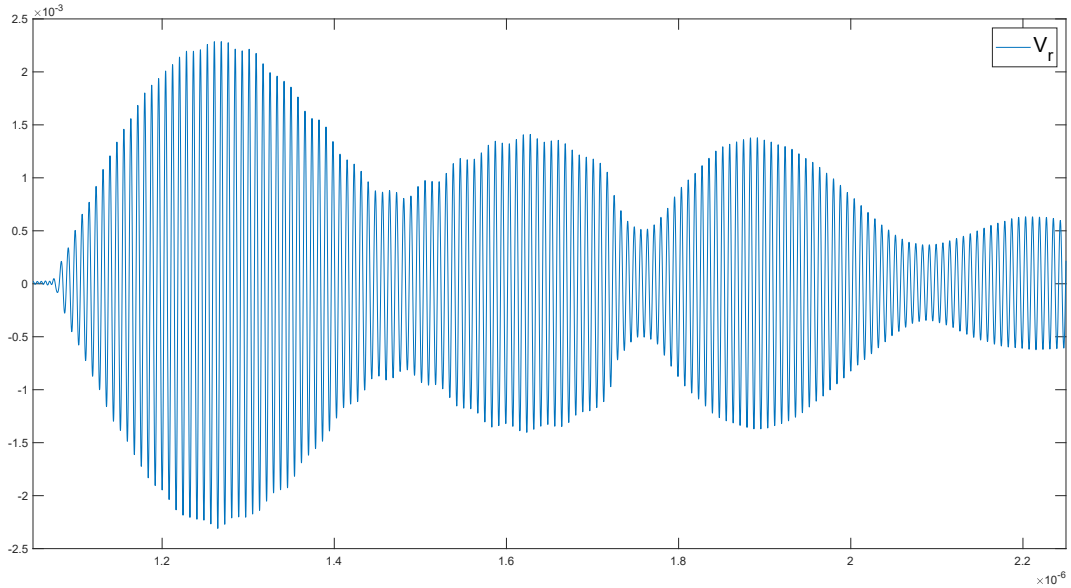

Figure 4.25: Voltage impulse response

It has also been tried to simulate the single delay line structure in presence of an added mass as in Fig.4.17. However, the introduction extra elements between the transducers makes the solver to employ very long time to compute the results and also to stop in some cases.

4.1.5 Frequency domain study

Frequency-dependent analysis have been performed in order to obtain a characterization of the devices that is closer as possible to the one obtained with a measurement instrument such as a vector network analyzer. They provide output in a similar way with respect to the experimental data, making the comparison to be very simple. Moreover, they overcome the issues related to the time consumption from which time domain analysis suffer. Because of their lower complexity, it is possible to simulate elaborated structures that would be not feasible for time-dependent simulation. Frequency domain studies allow to apply to a structure a harmonic excitation and to compute its subsequently response, for particular frequency values. In electromagnetic applications, it can be used to compute transmission and reflections parameters of a model. It allows to obtain as output quantities such as scattering parameters, impedances, magnitude and phase of transfer functions.

In this work, single delay line structures having 80 fingers pairs, with a periodicity of 8 μm have been simulated, for both X-parallel and X-perpendicular directions of the $LiNbO_3$ 128°YX substrate.

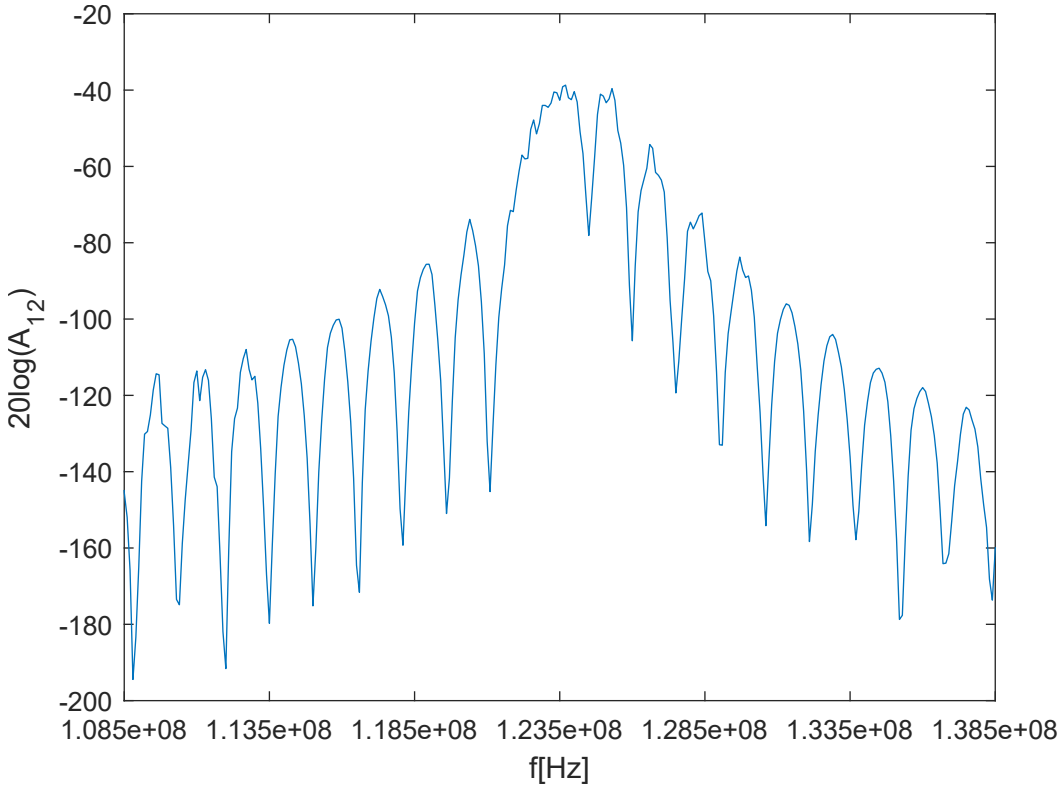

Figure 4.26: X-parallel logarithmic frequency response

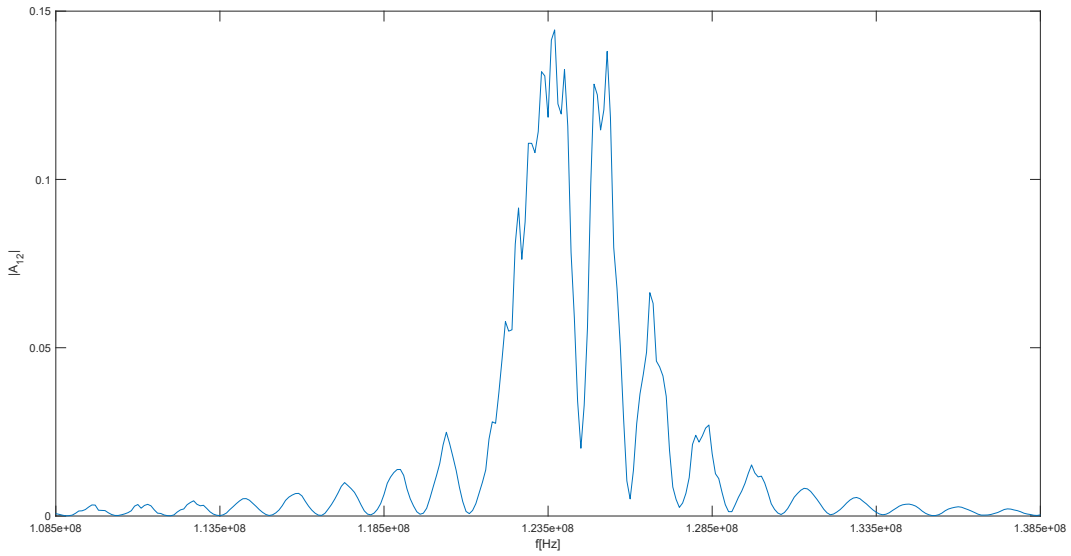

Figure 4.27: X-parallel linear frequency response

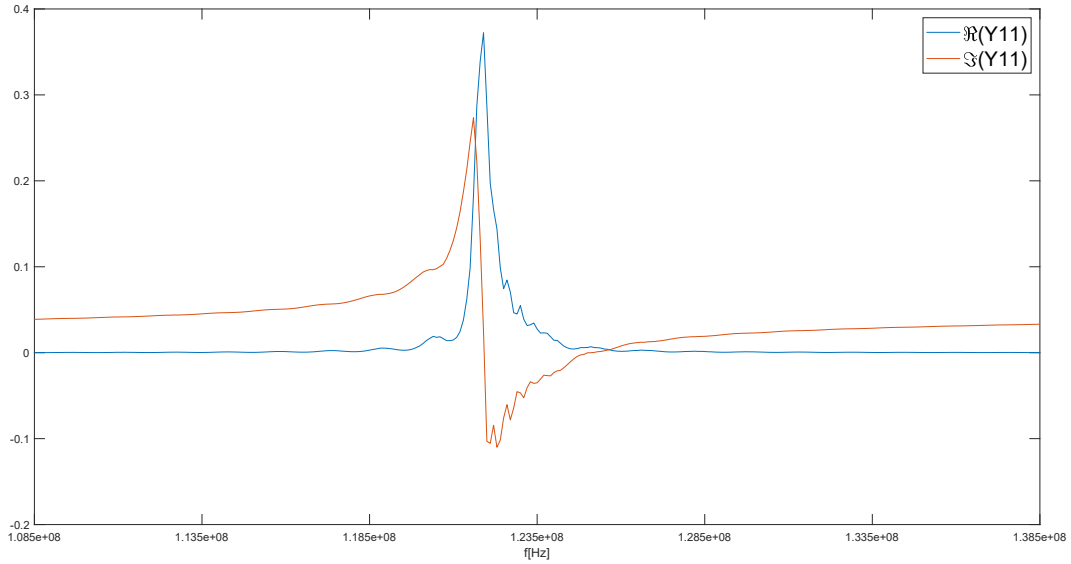

Figure 4.28: X-parallel Real and Imaginary part of impedance Y_{11}

Harmonic excitation sweeping in a range around the theoretical operating frequency is imposed on the transmitter IDT, then impedances are computed with respect to the frequency. These impedances are then combined according to the mathematical model to obtain frequency response of the two-port system.

Peak amplitude are centered at 123.7 MHz in the first case and at 114 MHz in the second case, as predicted. In the X-parallel case, it can be seen a secondary

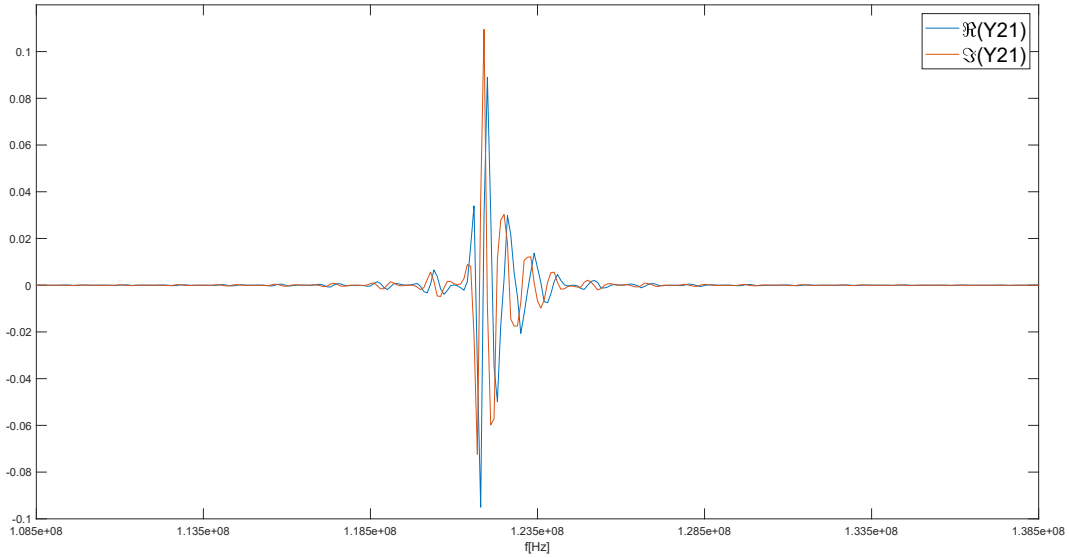

Figure 4.29: X-parallel Real and Imaginary part of impedance Y_{21}

peak due to spurious signals caused by reflection effects, which can be filtered out by windowing the time transform as will be shown in the next chapters. Instead in the X-perpendicular case, a 2.8 MHz bandwidth can be easily recognizable and it agrees with the theoretical predictions.

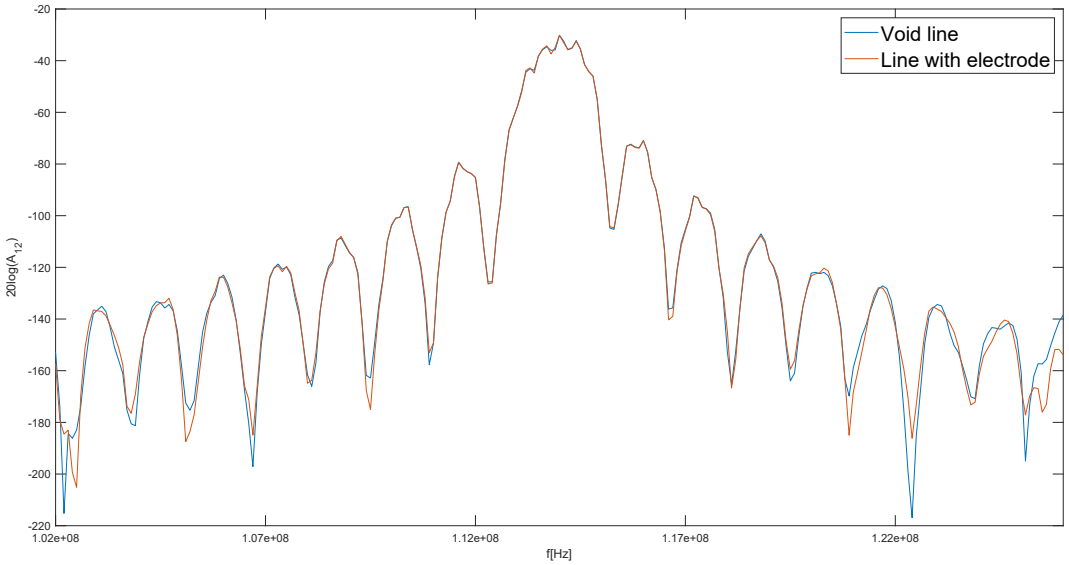

Figure 4.30: X-perpendicular logarithmic frequency response

It has also been tried to simulate the presence of an added mass in the frequency

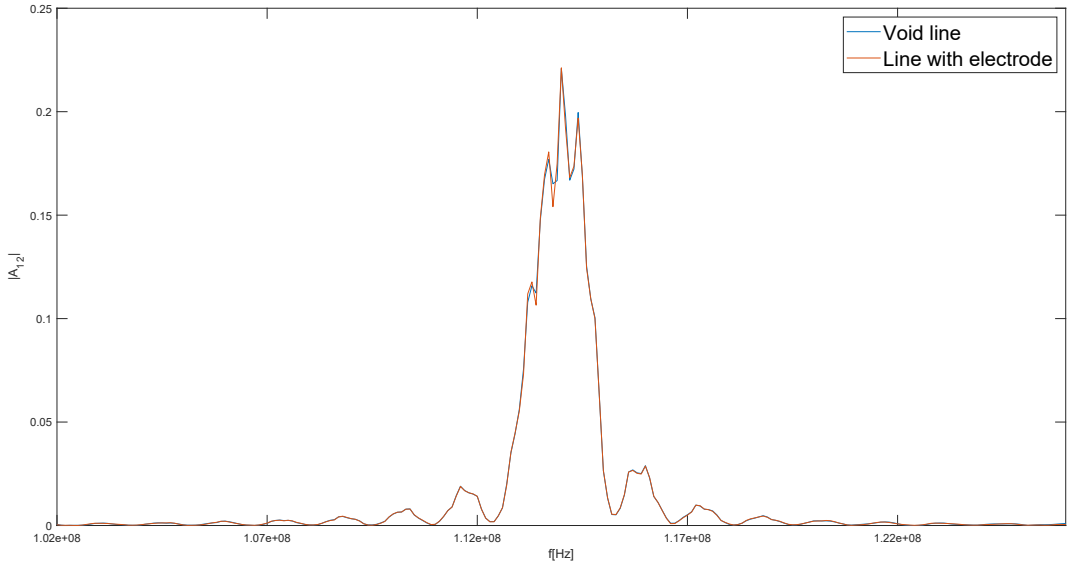

Figure 4.31: X-perpendicular linear frequency response

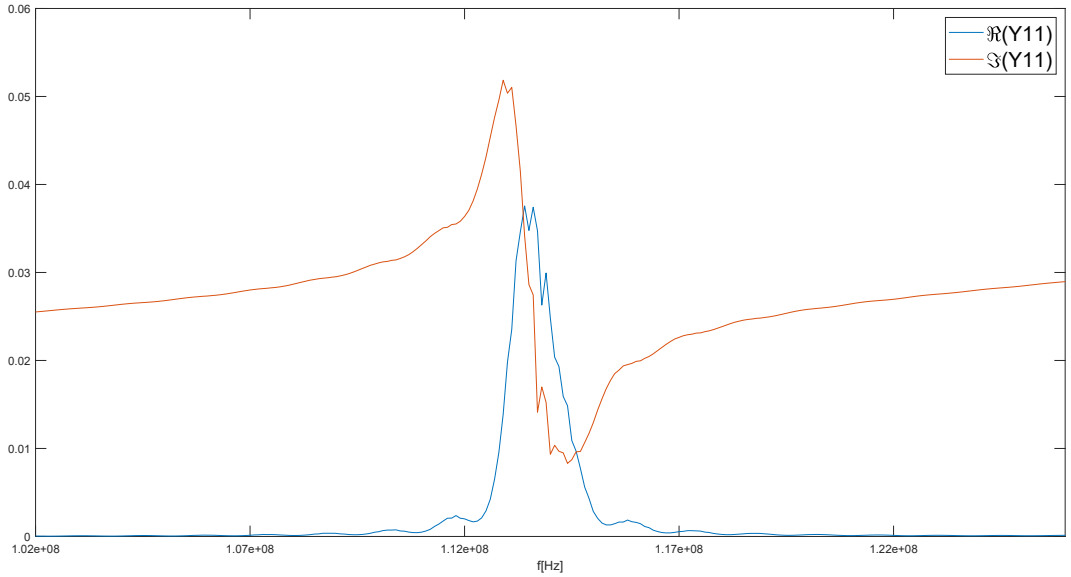

Figure 4.32: X-perpendicular Real and Imaginary part of impedance Y_{11}

domain as in the time domain case, either on the dummy line as well as on the single delay line. However, results were not satisfactory. The amount of mass needed to modify the frequency response was too much, not matching the results obtained experimentally. Reasons could be the lack of proper boundary conditions applied to the load or some other mismatches between the COMSOL model and the real device which has not been found.

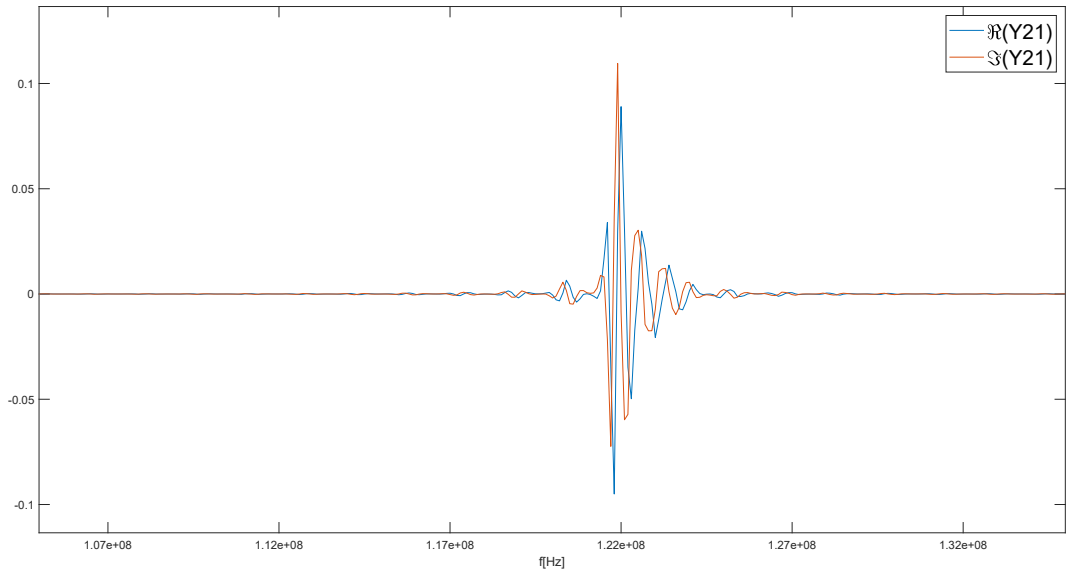

Figure 4.33: X-perpendicular Real and Imaginary part of impedance Y_{21}

4.2 Experimental

4.2.1 Fabrication

Surface acoustic waves delay lines have been realized on $LiNbO_3$ 128°YX wafers, each line consisting of a couple of interdigital transducer. IDTs have been designed with 80 fingers pairs, with a finger width and spacing of 8 μm.

The lithographic process steps are:

- Cleaning: The cleaning of the $LiNbO_3$ substrate was carried out with acetone and it was dried by a N_2 flow. Afterwards, the sample was ultrasonated for 20 minutes, and washed with ultra-pure water. Finally, dehydration was performed on a plate heated at 200°C for 20 minutes in order to remove water residue.

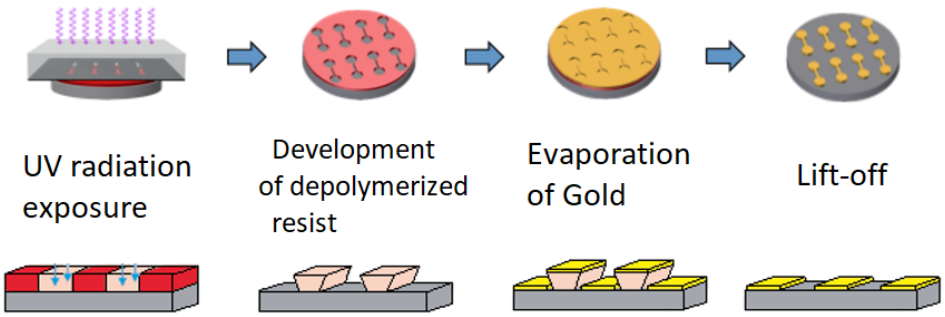

Figure 4.34: Main fabrication steps

- Resist deposition: the resist is a photo-sensitive polymer. Because of its chemical nature, after exposure to UV radiation a series of reactions induce a change in solubility with respect to a developing solvent. Resist thickness can be controlled by setting spin coating parameters. The substrate is anchored to a rotor the liquid resist is poured on the anchored substrate to a rotor, which allows the uniform spreading of the fluid by means of the centrifugal force. Thickness will be determined by speed and rotation time. Before the resist deposition, a primer solution (e.g. hexamethylhexyloxane) is spin coated. It acts as an adhesion layer for the resist, enhancing its bond with the substrate surface. The speed of the spin coater has been set to 300 rpm for 3 seconds and then increased to 4000 rpm for 40 seconds, for both the primer and the resist deposition. The first time step is performed to eliminate the excess liquid Photoresist AZ 5214B, or methoxypropylacetate, was employed to create a

layer of about 1µm on the top of the substrate. Afterwards, the substrate is heated on a plate at 120°C for 2 minutes in order to induce the polymerization.

- Exposure: the IDTs pattern to be transferred on the substrate is previously drawed with CleWin and then loaded on a Mask-less Heidelberg DWL 66fs Laser Writer. The machine impresses the photoresist by depolymerizing it with a diode laser characterized by a wavelength of 405 nm. It is used in clean room and it allows to reach very high performances thanks to a lens system and to the pneumatic control of the work table where the substrate is anchored. The laser beam scans the entire substrate, reaching a resolution up to 600 nm.

- Development: in this phase, the depolymerized resist zones are removed. In order to do this, the sample is immersed for about 20 seconds in a resist development solution called AZ 726 MIF , consisting of $(CH_3)_3NOH$, and then in deionized water to stop the development. Finally, the surface is dried by means of a N_2 flow. During the process the progress of the development is monitored under the optical microscope to avoid the spoiling of the resist layer. If necessary, the process may be repeated by reimmersion in the development solution.

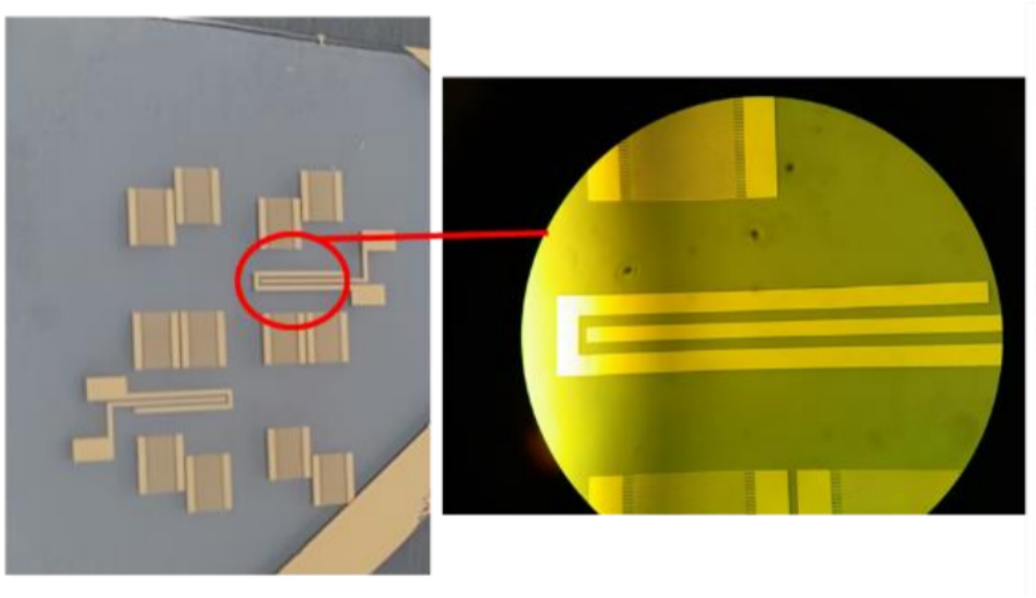

Figure 4.35: SAW devices layout

- Evaporation: during this process a Gold layer is deposited over the substrate by thermal evaporation. The thermal evaporator consists of a bell connected

to a vacuum system. Inside it, Tungsten crucibles electrically connected to the system host powdered or flaked metals, while the substrate is fixed to a holder. The crucibles heated by Joule effect, transfer the heat to the metal powder, which is liquefied and vaporized. The evaporated metal will cover the entire sample, either the resist coated regions as well as the uncoated ones. A Chrome adhesion layer few nanometers thick is previously deposited to promote the bonding. A thickness gauge inside the machine monitors the metal layer and the process ends when the Gold layer reaches the wanted thickness.

- Lift-off: The residual photoresist is removed along with the metal deposited on it. This process consists in submerging the sample in an acetone bath. After this step, only the regions which were not anymore covered with the photoresist remain on the surface, making the pattern to appear.

The MIP sensing element is based on a material called o-phenylenediamine (OPD), that is a functional monomer synthesized by electropolymerization on the surface of a Gold electrode. After the cleaning of the electrodes, the solution made up of 5% acetic acid (CH_3COOH) and the C-reactive proteins (CRP) to be imprinted in 1 μg/ml concentration is placed on it. Cyclic voltammetry is an electrochemical technique which uses a three-electrode arrangement, a working electrode at which the voltage is scanned with respect to the reference electrode and a counter electrode at which the current is measured. 10 cycles of cyclic voltammetry are performed employing an electric potential in a range of -0.2:1 V, that is varied linearly between these values. During the process the conductivity of the polymer is reduced, making the current flowing through the electrodes to decrease. The current is then measured and plotted against the applied voltage, resulting in a diagram called voltammogram [103]. The MIP is then washed in the acetic buffer solution to remove the template molecules. The non-imprinted polymer (NIP) was built by means of the same procedure, without the addition of the imprinting molecules.

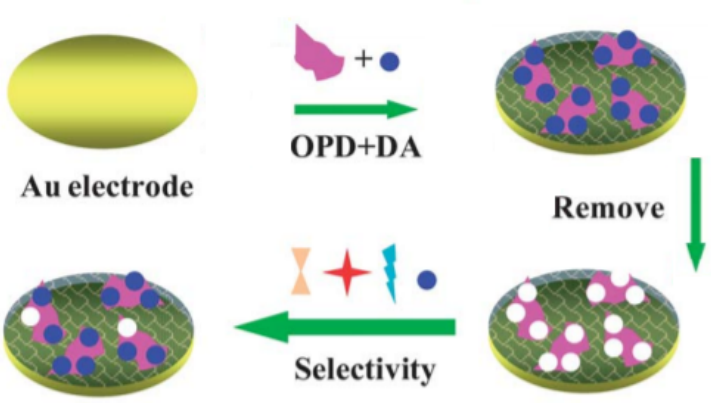

Figure 4.36: MIP fabrication steps

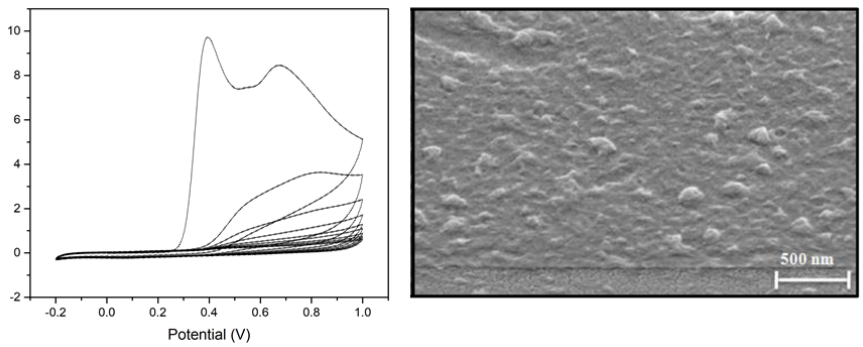

Figure 4.37: Voltammogram and SEM image of the MIP surface

4.2.2 Measurements

SAW devices are generally characterized by their frequency response. These operations are carried out by means of a vector network analyzer (VNA), an electronic instrument able to determine the frequency dependent properties of a device. VNAs operate over a large range of frequencies, from few kHz to GHz and are employed in several applications such as transmission lines measurements, circuit design and material characterization. Electrical properties such as impedance and admittance of the device under test correspond to the ratios of signals, which can be easily expressed in form of scattering parameters, called S-parameters. S-parameters put in relation incident and reflected power waves at ports, allowing the full characterization of a device. These parameters are particularly suitable in RF and microwave regimes because they can be obtained without terminate lines with shorts or opens but rather by employing a proper reference impedance [104].

Any two-port network can be defined as

$$\begin{pmatrix} b_1 \\ b_2 \end{pmatrix} = \begin{pmatrix} S_{11} & S_{12} \\ S_{21} & S_{22} \end{pmatrix} \begin{pmatrix} a_1 \\ a_2 \end{pmatrix}$$

where

$$S_{ji} = \left. \frac{b_j}{a_i} \right|_{a_x=0, x \neq i}$$

are the scattering parameters and a_i and b_i are respectively the incident and reflected waves at port i.

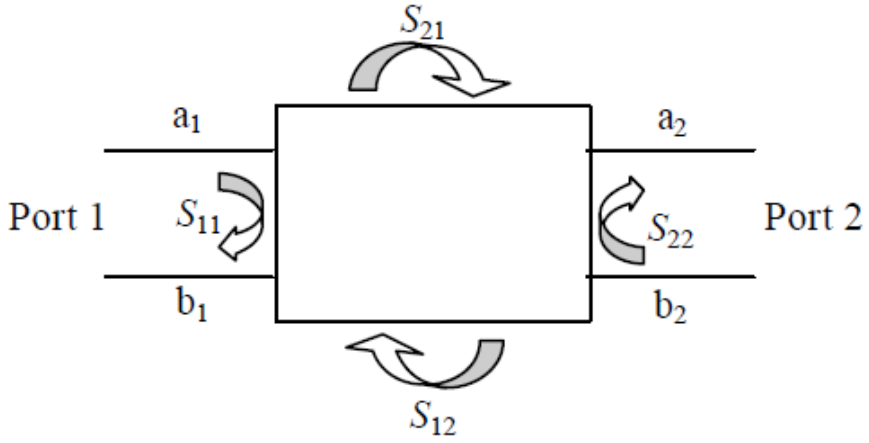

Figure 4.38: 2-port S-parameters

A calibration of the instrument is required before perform the measurements. This operation is done to compensate cable discontinuities which can cause internal

reflections and alterate the results. Subsequently, input and output port of the device are connected to the VNA ports through two cables. Port 1, which is used as RF source, generates the incident voltage wave a_1. The source is a sinusoidal signal whose frequency is swept across a predetermined range. Incident wave produces reflected wave b_1 and transmitted wave b_2, complex quantities measured by the instrument. The ratio between incident and transmitted waves gives the transmission parameter S_{21}, which is the quantity under investigation [105]. However, when transmission coefficient S_{21} is directly measured, acoustic waves which comes from multiple scattering against electrodes and borders affects the spectrum. The major contribution to this effect is the triple transit effect, which is the signal produced by the waves travelling along the line three times. This spurious signal is characterized by being delayed of twice the overall line delay and it can be easily identified observing the time evolution of the propagation. Exploiting

Figure 4.39: Vector network analyzer Keysight E5061B ENA

the duality between frequency and time domain, it is possible to transform the frequency response of the system in its impulse response by means of a Discrete Fourier Transform (DFT), a Fourier transformation which represents the counterpart of the continuous Fourier transform. DFT is a technique largely used in many engineering practical situations, such as signal processing applications, and it can be implemented by numerical methods. Fast Fourier Transform (FFT) is the most known of these numerical algorithms.

Thus, to filter out these unwanted reflection effects, an inverse FFT algorithm is applied to frequency response of the device and its impulse response is obtained. Subsequently a window function is applied to this time domain signal, selecting

only the wanted portion, corresponding to the delay line primary response. By doing so, spurious components of the signal are simply cut out. Many different windows functions can be used, each one having different performances in terms of frequency resolution and amplitude accuracy. Finally FFT is performed on the windowed time domain signal and the filtered transmission spectrum is obtained. The result is a smooth spectrum, in which ripples due to scattering effects are eliminated [106].

Measurements of the devices have been carried out on the void line, on the line combined with NIP, on the line with MIP before the analytes binding, after the binding and after the analytes have been washed from the MIP structure. These operations have been performed by means of a vector network analyzer Keysight E5061B ENA.

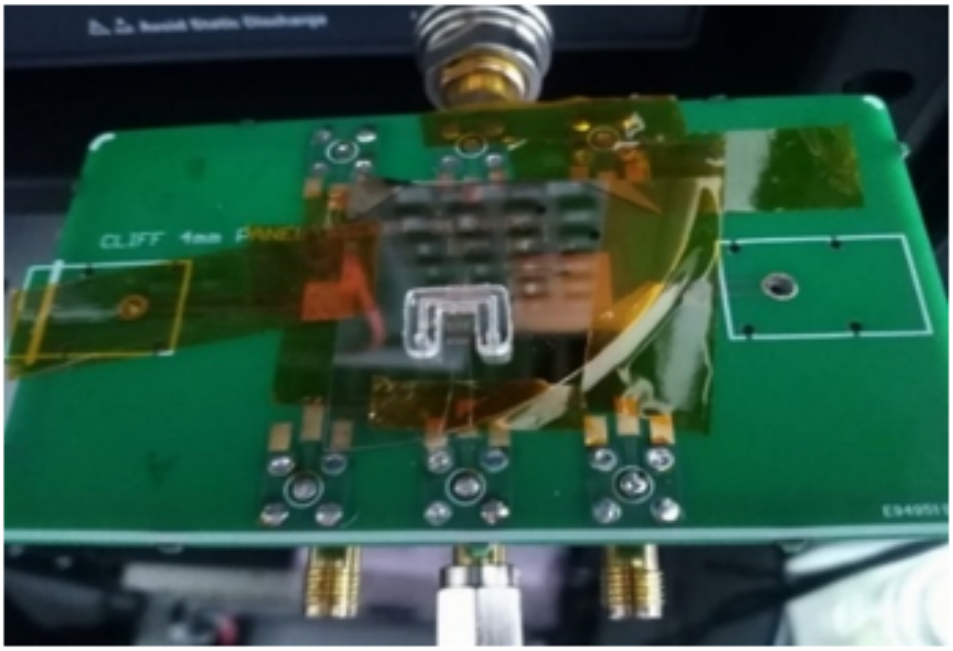

Figure 4.40: Device measurements

4.3 Measurement results and comparison with simulations

In this section, measured data for different sensing elements are showed and compared. Subsequently, frequency simulations obtained from COMSOL models have been compared with the measurement of the homologous model. Delay lines having 80 fingers pairs, with a 8 μm periodicity built on the top of a $LiNbO_3$ substrate, in the X-perpendicular direction are measured by means of a vector network analyzer Keysight E5061B ENA. The reported measurements comes from three structures: one having only the electrode for the MIP growth, one with a synthesized NIP and one with the MIP 1 μg/ml concentration. Data is acquired in a range from 104 MHz to 124 MHz, in steps of 12.5 kHz.

Table 4.1: Peak measurements values

Device	Peak Amplitude	Peak Frequency [MHz]
Only electrode	0.29446	114.144
NIP	0.27799	114.081
MIP 1 (μg/ml)	0.18177	113.994

With respect to the case in which only the electrode is present, NIP structure causes an attenuation of the 5.6% and a frequency shift of 63 kHz. MIP structure instead causes an attenuation of the 38.3% and a shift of 150 kHz.

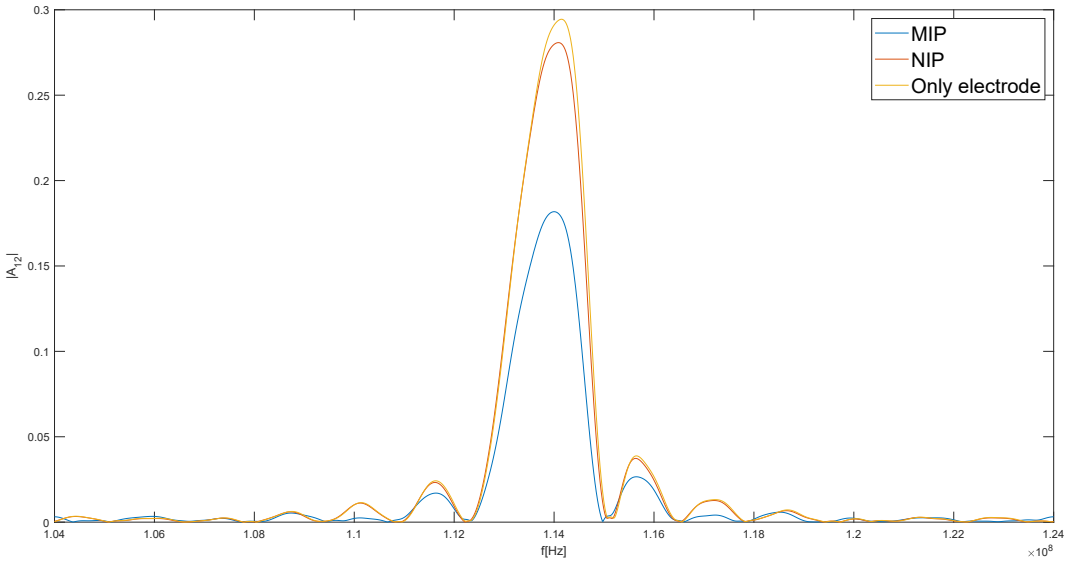

Figure 4.41: Measurements of line with MIP, NIP and only the electrode

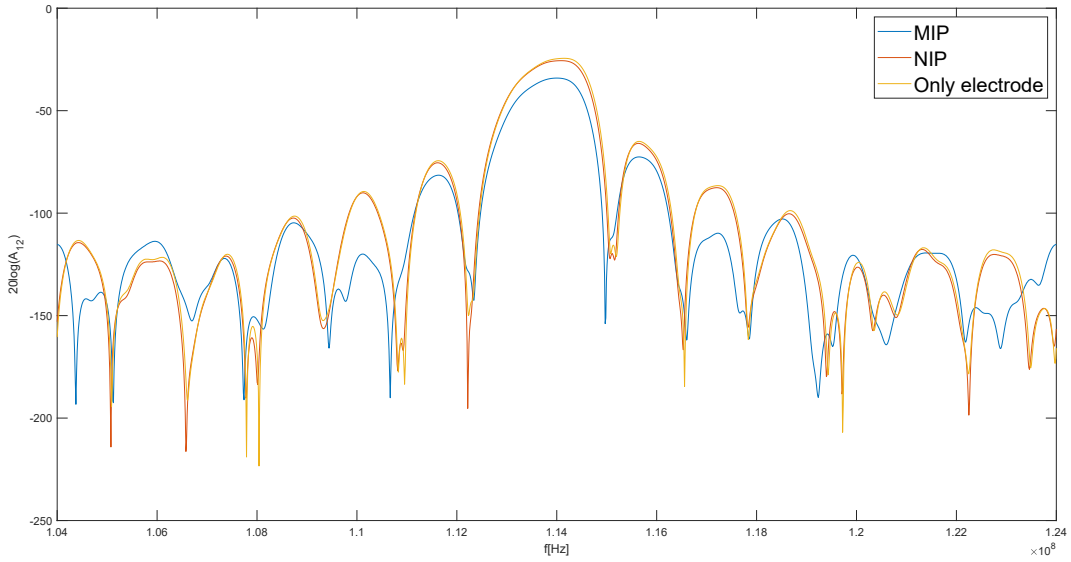

Figure 4.42: Measurements of line with MIP, NIP and only the electrode, in logarithmic scale

After the comparison among experimental data, simulations and measurements are compared. Frequency domain simulation result relative to the single delay line structure, with the presence of the electrode for the MIP electrosynthesis is compared to the experimental measurement of the homologous device. The frequency response obtained from the COMSOL model is characterized by ripples mainly due to reflections which are difficult to eliminate by using absorbing boundaries. A more convenient way is to exploit FFT algorithms to transform the frequency response in time domain, cut the time region of interest getting rid of unwanted reflections and to transform it back in frequency domain. This procedure, that is very similar to the one performed by the network analyzer, has been implemented by means of a Matlab script. Applying an IFFT to the frequency response, data plotted in Fig.4.44 are obtained. The shape of a delay line time evolution can be recognized, where the main envelope is separated from the spurious signals caused by scattered waves. The signal which comes from the main time response is selected and the remaining part of it is discarded. Applying a FFT routine to the selected time domain signal, it is possible to obtain again a frequency response. The resulting spectrum is smooth and regular, according to measured one. The obtained frequency response peak is centered at the same frequency value as the measured one, with a difference of 61 kHz. The peak amplitude of the spectrum is presented a reduction by the 35.5% with respect to the experimental data. This is due to the mechanical damping which has been measured but estimated. The Rayleigh mechanical damping is defined by two coefficients α and β, related respectively to the mass and to the stiffness of the piezoelectric material. The damping ratio ξ can be written in terms

of the sum of these coefficients multiplied by the frequency. After that different values of damping have been investigated, the value $\xi = 0.001$ has been chosen, also according to a work in which this value has been employed in a analogue situation [102].By further optimizing this parameter it should be possible to obtain a model whose frequency behaviour is the same of the experimental devices.

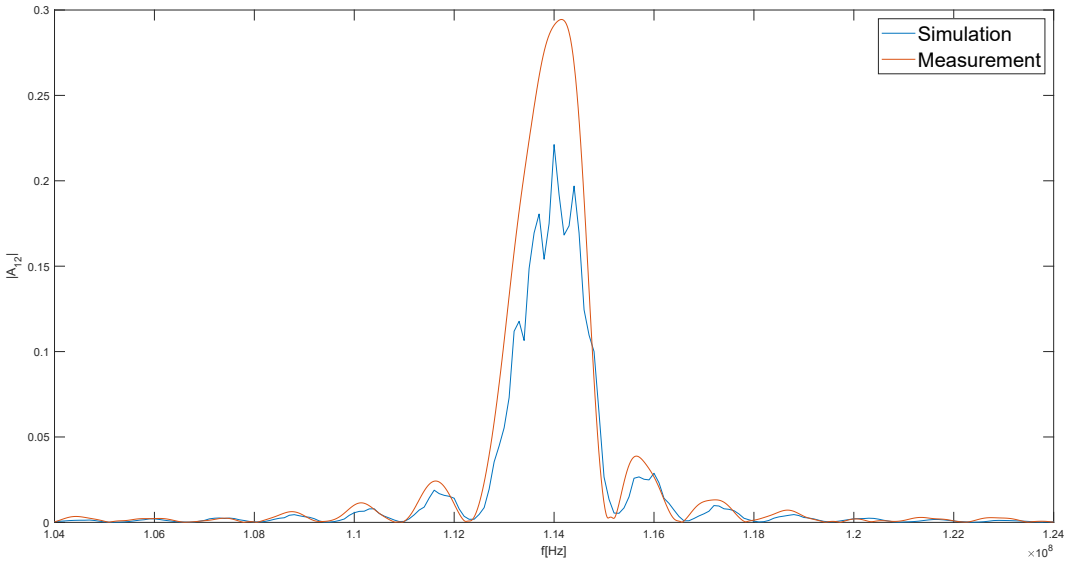

Figure 4.43: Unfiltered simulated frequency response vs. measured one

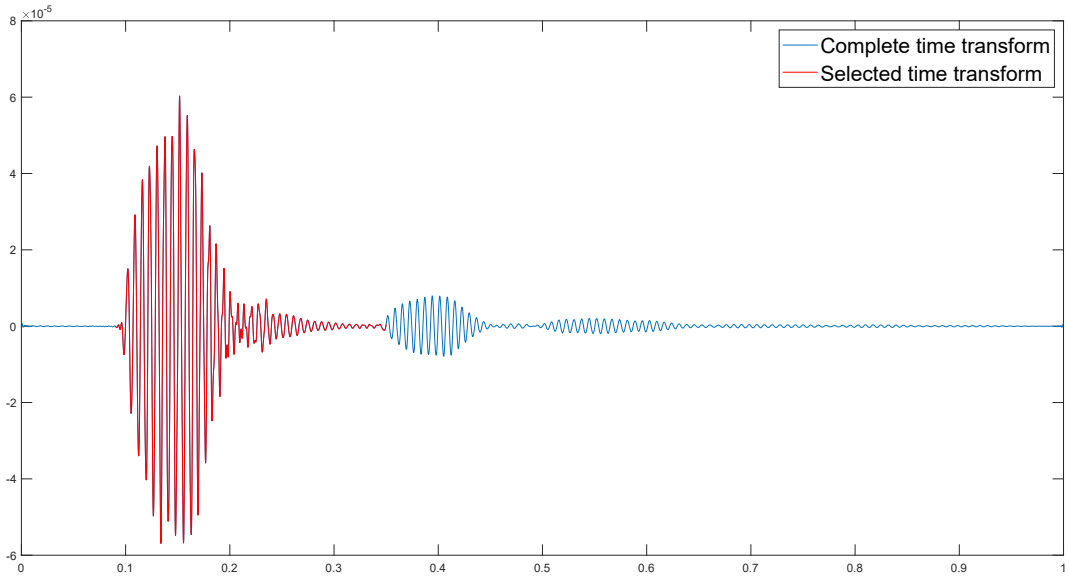

Figure 4.44: Time transform and envelope selection

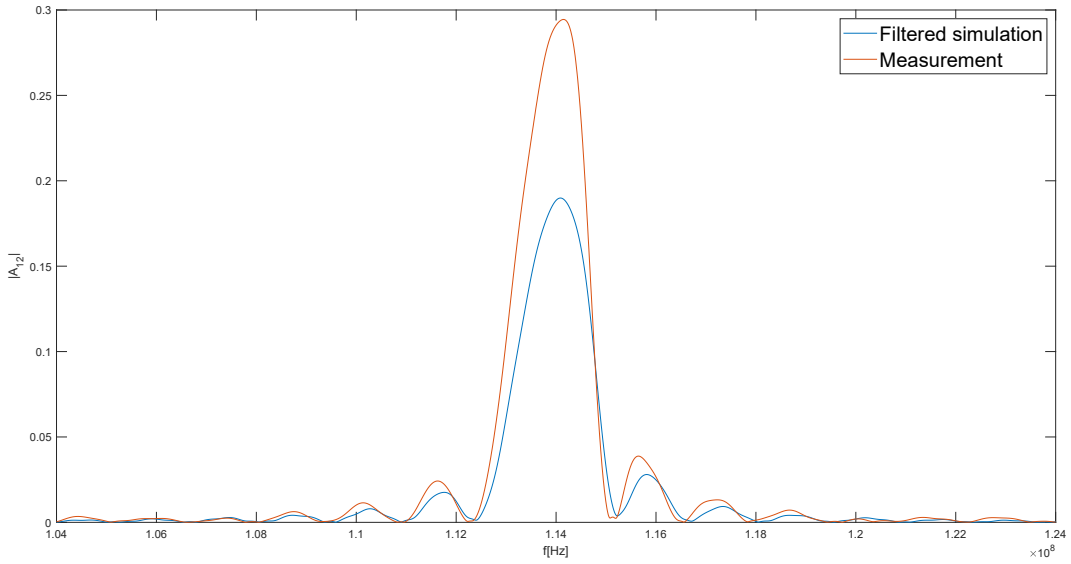

Figure 4.45: Filtered simulated frequency response vs. measured one

Chapter 5

Micropumps control

5.1 System overview

A microfluidic module is going to be integrated above the delay lines, in order to deliver saliva samples to the sensitive areas. Liquids must be pumped into the inlets by means of a controlled micropumping system. The system consists in a STM32 NUCLEO-F303K8 board and in a mp6-QuadOEM driver. The microcontroller receives instructions from a computer, through a graphical user interface which was designed in Microsoft Visual Studio in C# language. A C routine has been written and loaded into the NUCLEO board, which allows it to communicate on the serial line with PC and with the pump driver, by writing proper data in its registers. A NUCLEO-F303K8 development board from STMicroelectronics

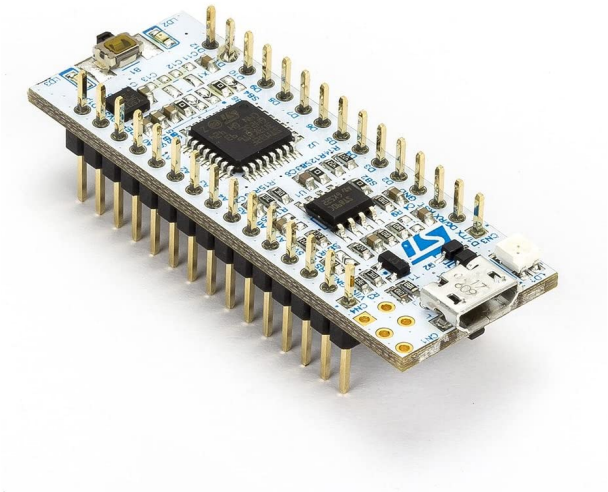

Figure 5.1: NUCLEO-F303K8 board

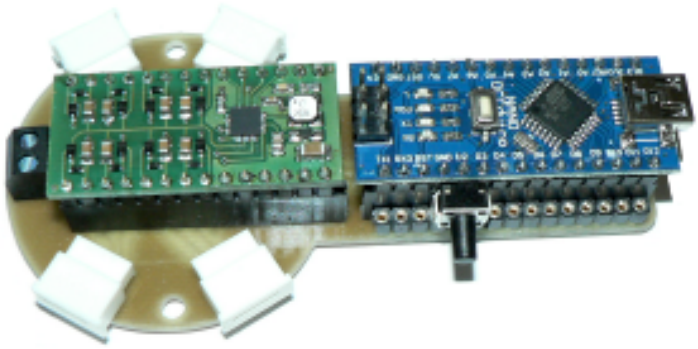

Figure 5.2: mp6-QuadKEY board

Figure 5.3: mp6-liq piezoelectric diaphragm pump

was employed to implement the control system. The microcontroller carries a ARM®32-bit Cortex®-M4 CPU, with 72 MHz of maximum operation frequency. It has 64 KB Flash, 12 KB SRAM, timers, different serial interfaces such as SPI, I2C or USART and many other features [107].

The mp6-QuadOEM is a high-voltage DC-AC converter from Bartels Mikrotechnik, able to drive four mp6 pumps and designed for gas and liquid pumping applications [108]. The device consists in a boost converter and a full-bridge output stage. Moreover, it contains a spread-spectrum oscillator which is employed to reduce the amount of EMI arising from the boost converter. Its voltage input range makes him suitable for any kind of voltage sources and its output can generate up to 250 Vpp. It provides a I2C interface through which the user can set the registers

bits, responsible for the output waveform settings. In particular, peak-to-peak voltage, frequency, ramp-on/-off times, shape, and slope can be programmed by means of the registers. Output waveforms can be full or half wave and they are set by two bits of the signal shape register SHAPE[1:0], while signals slope bits SL[1:0] allow to choose between sine slope, fast slope, faster slope or fastest slope (square wave). An internal oscillator is used to set the desired output frequency, tunable by means of the FO[7:0] register bits. By programming VO1_[4:0], VO2_[4:0], VO3_[4:0] and VO4_[4:0] bits, output peak-to-peak voltages can be varied independently from 0 to 250 Vpp. Finally, the bits RT1_[2:0], RT2_[2:0], RT3_[2:0], RT4_[2:0] of the ramping time registers program the slow fade-on and slow fade-off time feature. It is an I2C-compatible as a slave device, having a 2-wire interface

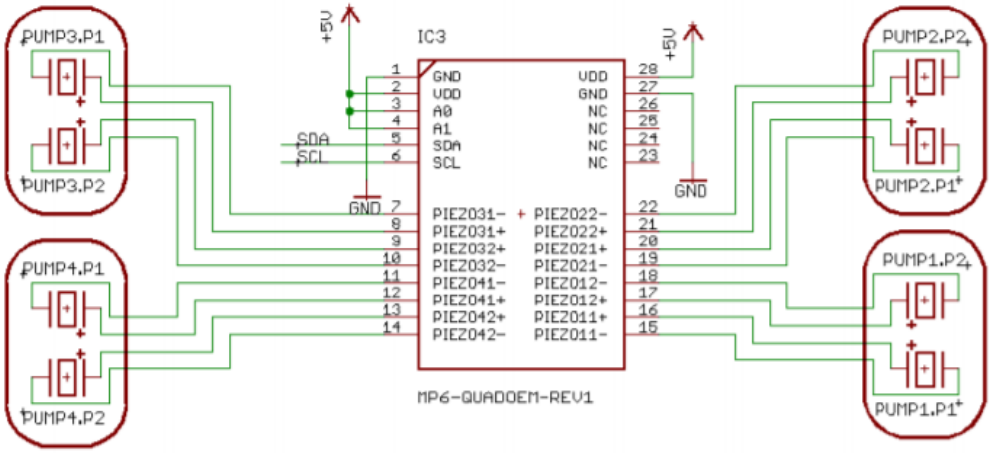

Figure 5.4: mp6-QuadKEY board schematic

made up of two serial lines, reserved respectively for data and clock signals. Firstly the master generates the clock signal, then it starts the data transfer. During the communication, the slave address, the register address and the data bits are transmitted on the line. Each sequence which is transmitted consists in a 8 bit word. The master reads data from the mp6-QuadOEM serial data line synchronized with the serial-clock pulses.

5.2 GUI and codes

A GUI has been designed in Microsoft Visual Studio IDE, in order to control the pumps in a simple and practical fashion.

Microsoft Visual Studio is an integrated development environment created by Microsoft, generally employed to develop web services and applications, computer programs and mobile apps. This IDE exploits software development platforms such as Windows Form to produce code and it supports nearly any programming language. It comes with a code editor, a debugger and visual designers. In particular the Windows Forms designer is used to build graphical user interfaces. This tool allows to model the form layout by means of controls such as textboxes, listboxes, buttons and many others, which can be easily created by dragging them inside the design surface. While the controls are introduced into the graphical interface, the designer automatically generates C# code for the application.

The interface is a Windows Form App, made up of buttons, numericUpDown and comboBox menus. Initially, the available ports are searched and the first one is selected. The "Open/Close Port" button starts and stops a serial communication with the NUCLEO board, it opens the port when it is closed and closes it when it is opened. When the port is opened, the panel is activated. In the panel, numericUpDown menus allows to choose between predefined frequency values (from 100 to 800 Hz, with a 100 Hz stepping) and peak-to-peak voltage channels values (from 0 to 250 Vpp, with a 50 V stepping). Moreover, it is possible to set the waveform shape (between sine, fast slope, faster slope and square) through a comboBox menu. A checkbox labelled as CH1 Master makes every channels voltages equal and dependent to the Channel 1 one. This feature is introduced in order to simplify the case in which all the active channels must be activated at the same voltage level. Finally, when all the parameters are set, the ON/OFF button transfers the codified commands to the microcontroller through the serial connection. All the steps are logged into a textbox.

The code loaded into the NUCLEO board consists in a number of instructions which allow the communication with both computer and pumps driver. A setup function defines a serial communication and writes the reset conditions into the driver registers. In a continuous loop, firstly the microcontroller waits for the data from the computer and read it from the serial line. When the string is arrived, it is properly terminated and it is decoded by another function. Here, according to the encoding, the command is interpreted. Finally, when all the required instructions to define the pumping operation are received, another function writes the corresponding bits into the mp6-QuadOEM control registers and starts the process.

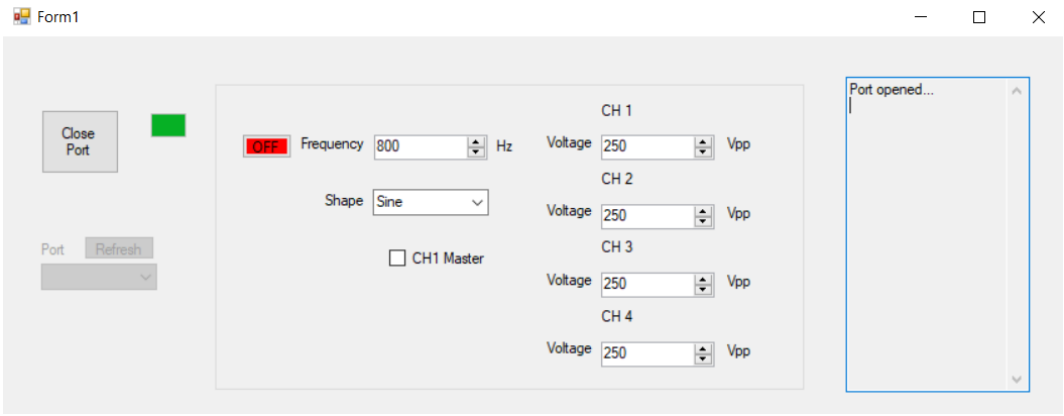

Figure 5.5: Windows Form App GUI

Chapter 6

Conclusions

In this work, devices made up of SAW delay lines and MIP/NIP structure has been investigated in different ways. The purpose of these devices is to detect the presence of the IL-10 biomarker bound to the polymer receptor material. The behaviour of the device has modeled according to the choices of the LiNbO3 128°YX as substrate material, of its X-perpendicular orientation that supports a Rayleigh propagation mode and of the IDTs geometry. The surface wave velocity of the substrate along with the 8 μm fingers width and spacing defines the synchronous frequency to be 114 MHz, and the 80 pairs of fingers of the transducers make the bandwidth of the frequency response to be 2.85 MHz. A mathematical model of the delay line has been implemented in Matlab in which design input parameters has been inserted. The model provided the frequency behaviour of the device, in terms of impedances and frequency response, that allowed to foresee the output characteristics of the system. The devices layout has been drew in CleWin in order to generate a file to be provided to the photolithography machine. A 2D FEM model has been created in COMSOL in different forms: a dummy delay line, a dual delay line and a single delay line. The matrices defining the substrate material orientation have been computed by means of a transformation procedure. Meshes of different shape and size have been investigated in order to obtain results with a good accuracy level. Geometrical parameters of the substrate and of the fingers have been varied, along with different boundary conditions that have been defined. Eigeinfrequency analysis have been carried out on the IDT elementary cell of a wavelength length. Results showed a horizontal and vertical displacement profile compliant with the Rayleigh propagation mode, at the device synchronous frequency, validating the definition of the materials. Time domain analysis have been performed on the structures, investigating mechanical damping effect and mass loading effect. In order to observe the time evolution of the system, different input signal have been employed. It can be noted from the result that the waves travel along the line in a time equal to the ratio between distance of the IDTs and the wave velocity, guaranteeing the

correctness of this latter quantity. Displacement plots and animation showed the correct propagation and confinement of the superficial waves. Moreover by properly tuning the simulation time steps, a well-shaped envelope is obtained, whose center frequency matches the synchronous one. Frequency domain analysis have been conducted on the 80-fingers pairs structure to obtain impedances and frequency response of the line, that well matched the operating frequency and bandwidth specifications. These analysis have been repeated in presence of the electrodes for the MIP electrosynthesis, showing a slight attenuation and time shift. Output data have been postprocessed in Matlab to filter out the spurious components included in the spectra. Devices have been fabricated in clean room at CNR Nanotec facility. A maskless photolithography followed by a Gold deposition defined the IDTs and electrodes structures. MIP and NIP structure have been subsequently synthesized on top of a Gold electrode by means of cyclic voltammetry technique. Devices have been contacted and connected to a vector network analyzer Keysight E5061B ENA. Measurements of the frequency response have been reported for MIP case, NIP case and the void electrode case. These data showed a peak amplitude reduction and a frequency shift according to the mass loading effect. Experimental data of this last case has been compared with filtered frequency domain simulation outputs. From the comparison can be appreciated that the simulated frequency response is in accordance with measurements in terms of shape and synchronous frequency. The simulated peak amplitude is lower in the simulation due to the estimation of mechanical damping factor, which should be tuned in order to perfectly match the measured data. Moreover, a graphical user interface has been developed in Microsoft Visual Studio for a microcontrolled pumping system which will be used to deliver liquid samples to the sensing area.

In the future work, the models will be improved to match even more the real devices. The mechanical damping factor will be tuned through an optimization process, in order to obtain a frequency response with the same amplitude of the measurements. The models have to be modified in order to increase the mass loading effect sensitivity and being able to detect even lower amount of mass. Simulations will then be employed to optimize the system, in order to allow it to be used even in different applications, such as the environmental monitoring. The future intent is to overcome the current project goal and to apply the developed technology and knowledge to the detection of different molecules.

Bibliography

[1] Lord Rayleigh. «On waves propagating along the plane surface of an elastic solid». In: Proc. London Math. Soc., 17 (1885), pp. 4–11 (cit. on p. 1).

[2] A.E.H.Love. «Some problems of Geodynamics». In: (1911) (cit. on p. 1).

[3] L.N.Court. «Microwave acoustic devices for pulse compression filters». In: IEEE Trans., MTT-17 (1969), pp. 968–986 (cit. on p. 1).

[4] W.S.Mortley. «British patent 988,102». In: (1963) (cit. on p. 1).

[5] F.W.Voltmer R.M.White. «Direct piezoelectric coupling to surface elastic waves». In: Appl. Phys. Lett., 7 (1965), pp. 314–316 (cit. on p. 1).

[6] W.R.Jones J.J.Campbell. «A method for estimating optimal crystal cuts and propagation directions for excitation Of piezoelectric surface waves». In: IEEE Trans., SU-15 (1968), pp. 209–217 (cit. on p. 1).

[7] M.G.Holland M.B.Schulz B.J.Matsinger. «Temperature dependence of surface acoustic wave velocity on alpha-quartz». In: J. Appl. Phys., 41 (1970), pp. 2755–2765 (cit. on p. 2).

[8] E.Dieulesaint D.Chauvin G.Coussot. «Acoustic surface wave television filters». In: Electronics Lett., 7 (1971), pp. 491–492 (cit. on p. 2).

[9] E.G.S.Paige F.G.Marshall. In: Electronics Lett. (1999) (cit. on p. 2).

[10] E.G.S.Paige F.G.Marshall C.O.Newton. «Surface acoustic wave multisrip coupler and their applications». In: IEEE Trans., MTT-21 (1973), pp. 216–225 (cit. on p. 2).

[11] H.Sato K.Shibayama K.Yammouchi and T.Meguro. «Optimum cut for rotated Y-cut $LiNbO_3$ crystal used as the substrate of acoustic-surface-wave filters». In: Proc. IEEE, 64 (1976), pp. 595–597 (cit. on p. 2).

[12] E.A.Ash. «Surface wave grating reflectors and resonators». In: IEEE Intl. Microwave Symp. (1970), pp. 385–386 (cit. on p. 2).

[13] R.C.Rosenfeld E.J.Staples J.S.Schoewald. In: (1970) (cit. on p. 2).

[14] K.A.Ingebrigsten H.Engan and A.Tonning. In: Appl. Phys. Lett., 10 (1967), pp. 311–313 (cit. on p. 3).

[15] M.F.Lewis. In: IEEE Ultrasonics Symp. (1977), pp. 744–752 (cit. on p. 3).

[16] M.Tan B.A.Auld J.J.Gagnepain. In: Electronics Lett.,12 (1976), pp. 650–651 (cit. on p. 3).

[17] D.C.Malocha B.P.Abbott C.S.Hartman. In: (1990) (cit. on p. 3).

[18] J.M.Hodè M.Solal. In: (1993) (cit. on p. 3).

[19] W.Ruile J.Machui. In: (1992) (cit. on p. 3).

[20] A.Fischerauer C.Ruppel R.Dill. «SAW devices for consumer applications». In: IEEE Trans. UFCC, 40 (1993), pp. 438–452 (cit. on p. 3).

[21] M.F.Lewis. In: IEEE Ultrasonic Symp. (1982) (cit. on p. 3).

[22] D.P.Morgan. «History of SAW devices». In: IEEE Int. Freq. Symp. (1998), pp. 439–460 (cit. on p. 3).

[23] M.Rapp K.Länge B.E.Rapp. «Surface acoustic wave biosensors: a review.» In: Anal. Bioanal. Chem., 391 (2008), pp. 1509–1519 (cit. on p. 5).

[24] R.Dessy H.Wohltjen. In: Anal. Chem. 51 (1999), pp. 1458–1464 (cit. on p. 5).

[25] G.J.Bastiaan J.E.Roederer. In: Anal. Chem. 55 (1983), pp. 2333–2336 (cit. on p. 5).

[26] J.F.Vetelino J.C.Andle. In: Sens. Actuators, A 44 (1994), pp. 167–176 (cit. on p. 5).

[27] T.Moriizumi S.Shiokawa. «Design of SAW sensor in liquid». In: Jpn J. Appl. Phys., 27–1 (1987) (cit. on p. 5).

[28] C.R.Lowe E.Gizeli N.J.Goddard. In: Sens. Actuators, B 6 (1992), pp. 131–137 (cit. on p. 5).

[29] J.Reichert M.Rapp D.A.Moss. In: 7th Int. Conf Solid State Sensors and Actuators (1993), pp. 538–540 (cit. on p. 5).

[30] G.Harding E.Howe. In: Biosens. Bioelectron., 15 (2000), pp. 641–649 (cit. on p. 6).

[31] D.H.Dinh N.Moll E.Pascal. In: Biosens. Bioelectron., 22 (2007) (cit. on p. 6).

[32] Y.Roh Y.Hur J.Han. In: Sens. Actuators, A 120 (2005), pp. 462–467 (cit. on p. 6).

[33] Y.Roh J.Sakong H.Roh. In: Jpn J Appl. Phys., 46 (2007), pp. 4729–4733 (cit. on p. 6).

[34] R.T.Posaratnanathan V.Crivianu-Gaita M.Aamer. «Acoustic wave biosensor for the detection of the breast and prostate cancer metastasis biomarker protein PTHrP». In: Biosensors and Bioelect., 78 (2016), pp. 92–99 (cit. on p. 7).

[35] A.Grammoustianoua M.Giannelia K.Tsougenib. «Nanostructured PMMA-coated Love wave device as a platform for protein adsorption studies». In: Sensors and Actuators, B 236 (2016), pp. 583–590 (cit. on p. 7).

[36] C.Zerrouki G.Moreaua N.N.Fouratib. «Surface Acoustic Wave Biosensors for the Quantification of TNF-/SPD-304 Interaction». In: Procedia Engineering, 168 (2016), pp. 432–435 (cit. on p. 7).

[37] D. Milioni A.Kordas G.Papadakis. «Rapid Salmonella detection using an acoustic wave device combined with the RCA isothermal DNA amplification method». In: (2016) (cit. on p. 7).

[38] P.Jintao L.Xianhao W.Xiaoyi. «A high performance humidity sensor based on surface acoustic wave and graphene oxide on AlN/Si layered structure». In: (2017) (cit. on p. 7).

[39] H.B.Nemade S.Trivedia. «Coupled resonance in SH-SAW resonator with S1813 micro-ridges for high mass sensitivity biosensing applications». In: Sensors Actuators: B. Chemical 273 (2018), pp. 288–297 (cit. on p. 8).

[40] V.E.Lawson E.R.Gray V.Turbé. «Ultra-rapid, sensitive and specific digital diagnosis of HIV with a dual-channel SAW biosensor in a pilot clinical study». In: npj Digital Medicine 1, 35 (2018) (cit. on p. 8).

[41] R.C.van de Merw J.J.Taylor K.M.Jaedicke. «A Prototype Antibody-based Biosensor for Measurement of Salivary MMP-8 in Periodontitis using Surface Acoustic Wave Technology». In: Nature, 9:11034 (2019) (cit. on p. 9).

[42] Q.Aojie P.J.Jandas L.Jingting. «Highly selective and label-free Love-mode surface acoustic wave biosensor for carcinoembryonic antigen detection using a self-assembled monolayer bioreceptor». In: Applied Surface Science (2020) (cit. on p. 9).

[43] S.J.Martin D.S.Ballantine Jr. R.M.White. «Acoustic Wave Sensors: Theory, Design and Physico-Chemical Applications». In: (1996) (cit. on p. 11).

[44] B.A.Auld. «In Acoustic Fields and Waves in Solids». In: (1973) (cit. on p. 13).

[45] «IEEE Standard on Piezoelectricity 176». In: (1986) (cit. on p. 14).

[46] S.Datta. «Surface Acoustic Wave Devices». In: (1986) (cit. on p. 17).

[47] Á.Montoya-Baides M.Rocha-Gaso C.March-Iborra. «Surface Generated Acoustic Wave Biosensors for the Detection of Pathogens: A Review». In: Sensors, 9 (2009), pp. 5740–5769 (cit. on p. 18).

[48] S.K.Nayak S.Mishra L.Unnikrishnan. «Advances in Piezoelectric Polymer Composites for Energy Harvesting Applications: A Systematic Review». In: Macromolecular Materials and Engineering (2018) (cit. on p. 20).

[49] Z.D.Deng H.Li C.Tian. In: Appl. Phys. Rev (2014) (cit. on p. 20).

[50] A.V.Goltsev A.L.Kholkin N.A.Pertsev. «Piezoelectricity and Crystal Symmetry». In: (2008) (cit. on p. 20).

[51] M.Zgonik M.Jazbinsek. «Material tensor parameters of LiNbO3 relevant for electro- and elasto-optics». In: Appl. Phys., B 74 (2002) (cit. on pp. 21, 22).

[52] H.P.Laba A.S.Andrushchak B.G.Mytsyk. «Complete sets of elastic constants and photoelastic coefficients of pure and MgO-doped lithium niobate crystals at room temperature». In: J. of Appl. Phys., 106 (2009) (cit. on p. 21).

[53] Sofia Nestora. «Molecularly imprinted polymers as selective sorbents for recognition in complex aqueous samples». In: (2017) (cit. on p. 24).

[54] I.A.Nicholls H.S.Andersson. «Molecularly Imprinted Polymers. Man-made mimics of antibodies and their applications in analytical chemistry». In: (2001) (cit. on p. 24).

[55] M.V.Polyakov. In: Zhur. Fiz. Khim. (1931) (cit. on p. 25).

[56] D.H.Campbell L.Pauling. In: Science, 95, 440 (1942) (cit. on p. 25).

[57] F.H.Dickey. In: Proc. Natl. Acad. Sci (1949) (cit. on p. 25).

[58] U.Colombo R.Curti. In: Chim. Ind., 23, 103 (1951) (cit. on p. 25).

[59] P.Anderson A.H.Beckett. In: Nature, 179, 1074 (1957) (cit. on p. 25).

[60] A.Sarhan G.Wulff. In: Angew. Chem., 84, 364 (1972) (cit. on p. 25).

[61] G.Wulff. In: A CS Syrup. Ser., 308, 186 (1986) (cit. on p. 25).

[62] K.Mosbach R.Arshady. In: Makromol. Chem,. 182, 687 (1981) (cit. on p. 25).

[63] K.Mosbach R.Arshady. «Synthesis of substrate-selective polymers by host-guest polymerization». In: Die Makromolekulare Chemie, 182 (1981), pp. 687–692 (cit. on p. 25).

[64] E.Moczko I.Chianella A.Guerreiro. «Direct replacement of antibodies with molecularly imprinted polymer nanoparticles in ELISA—Development of a novel assay for vancomycin». In: Anal. Chem., 85 (2013), pp. 8462–8468 (cit. on p. 25).

[65] A.Turner L.Uzun. «Molecularly-imprinted polymer sensors: realizing their potential». In: Biosensors and Bioelectronics, 76 (2016), pp. 131–144 (cit. on p. 25).

[66] K.Haupt B.Tse Sum. «Molecularly imprinted polymers: synthetic receptors in bioanalysis». In: Anal. and Bioanal. Chem., 398 (2010), pp. 2481–2492 (cit. on p. 25).

[67] M.Resmini. «Molecularly imprinted polymers as biomimetic catalysts». In: Anal and Bioanal. Chem., 402 (2012), pp. 3021–3026 (cit. on p. 25).

[68] A.Belmont K.Haupt. «Molecularly Imprinted Polymers as Recognition Elements in Sensors». In: (2008) (cit. on p. 25).

[69] F.D'Souza P.S.Sharma A.Pietrzyk-Le. «Electrochemically synthesized polymers in molecular imprinting for chemical sensing». In: Anal. and Bioanal. Chem., 402 (2012), pp. 3177–3204 (cit. on p. 26).

[70] X.Zhang G.Zcelikay S.Kurbanoglu. «Electrochemical MIP Sensor for Butyrylcholinesterase». In: (2019) (cit. on p. 27).

[71] R.T.Fenner. «Finite element method for engineers». In: (1975) (cit. on p. 28).

[72] R.W.Clough. «The finite element method in plane stress analysis». In: (1960) (cit. on p. 28).

[73] R.Courant. «Variational methods for the solutions of problems of equilibrium and vibrations». In: Bull. Am. Math. Soc., 49 (1943), pp. 1–23 (cit. on p. 28).

[74] K.Kumar V.Jagota A.P.S.Sethi. «Finite Element Method: An Overview». In: (2013) (cit. on p. 28).

[75] A.C.Cangellaris Y.Zhu. «Multigrid finite element methods for electromagnetic field modeling». In: (2006) (cit. on p. 29).

[76] A.Quarteroni. «The Galerkin finite element method for elliptic problems». In: (2009) (cit. on p. 29).

[77] B.Gupta et al. In: Oncology 2016, 91 (1999), pp. 13–23 (cit. on p. 32).

[78] Y.Cheng et al. In: Clin. Transl. Med (2014) (cit. on p. 32).

[79] M.S.Chiriacò et al. «Optimization of SAW and EIS sensors suitable for environmental particulate monitoring». In: (2018) (cit. on p. 34).

[80] V.Crivianu-Gaita et al. In: Biosensors Bioelectronics, 78, 92 (2016) (cit. on p. 34).

[81] C.Malitesta et al. In: Analytical and Bioanalytical Chemistry, 402 (5) (2012), pp. 1827–1846 (cit. on p. 34).

[82] P.Tang et al. In: Polymers, 10 (5) (2018) (cit. on p. 34).

[83] M.Polz-Dacewicz et al. In: Infectious Agents and Cancer, 11 (2016) (cit. on p. 34).

[84] L.T.Lee et al. In: International Journal of Oral and Maxillofacial Surgery, 47 (6) (2018), pp. 699–707 (cit. on p. 35).

[85] X.M.Ma et al. In: Biosensors Bioelectronics, 87 (2017), pp. 122–128 (cit. on p. 35).

[86] Z.Iskierko et al. In: Journal of Materials Chemistry C, 5 (4) (2017) (cit. on p. 35).

[87] M.S.Chiriacò et al. «Fabrication of interconnected multilevel channels in a monolithic SU-8 structure using a LOR sacrificial layer». In: Microelectronic Engineering, 164 (2016) (cit. on p. 35).

[88] M.S.Chiriacò et al. «Lab-on-Chip for Exosomes and Microvesicles Detection and Characterization». In: Sensors, 18 (10) (2018) (cit. on p. 35).

[89] J.Conway X.Chen M.A.Mohammad. «High performance lithium niobate surface acoustic wave transducers in the 4–12 GHz super high frequency range». In: (2015) (cit. on p. 40).

[90] D.Morgan. «Surface Acoustic Wave Filters With Applications to Electronic Communications and Signal Processing». In: (2007) (cit. on p. 40).

[91] F.Yang A.V.Mamishev K.Sundara-Rajan. «Interdigital sensors and transducers». In: IEEE Proc, 92, 5 (2004), pp. 808–845 (cit. on p. 41).

[92] W.Soluch. «Design of SAW delay lines for sensors». In: Sensors and Actuators, A 67 (1998), pp. 60–64 (cit. on p. 44).

[93] W.Soluch. «Admittance matrix of a surface acoustic wave interdigital transducer». In: IEEE Trans. Ultrasonics Ferroelectrics Freq. Control, 40 (1993) (cit. on p. 44).

[94] H.Engan. «Surface acoustic wave multielectrode transducers». In: IEEE Trans. Ultrasonics SU-22 (6) (1975), pp. 395–401 (cit. on p. 47).

[95] «COMSOL Documentation». In: () (cit. on p. 52).

[96] G.Zhang. «Orientation of Piezoelectric Crystals and Acoustic Wave Propagation». In: (2012) (cit. on pp. 53, 56).

[97] D.Abbott D.W.Dissanayake S.Al-Sarawi. «Modelling and simulation of wirelessly and securely interrogated low-powered actuators for bio-MEMS». In: (2010) (cit. on p. 56).

[98] D.Abbott D.W.Dissanayake S.Al-Sarawi. «Surface Acoustic Wave Based Wireless MEMS Actuators for Biomedical Applications». In: (2014) (cit. on p. 56).

[99] «https://www.comsol.com/support/knowledgebase/1244». In: () (cit. on p. 60).

[100] «https://www.comsol.ch/support/knowledgebase/1118». In: () (cit. on p. 60).

[101] D.A.H.Pennings. «Modeling and characterizing low-frequency impact sound transmission through floor constructions». In: (2017) (cit. on p. 61).

[102] S.Rizzato C.Maruccio M.Scigliuzzo. «Frequency and time domain analysis of surface acoustic wave propagation on a piezoelectric gallium arsenide substrate: A computational insight». In: Journal of Intelligent Material Systems and Structures (2018), pp. 1–12 (cit. on pp. 72, 89).

[103] Li Wu Dan. «Sensitive and selective determination of dopamine by electrochemical sensor based on molecularly imprinted electropolymerization of o-phenylenediamine». In: (2013) (cit. on p. 82).

[104] C.T.Madigan. «Exploring the properties of a combined differential-mode equalizer and common-mode filter». In: (2015) (cit. on p. 84).

[105] Q.Huang J.T.Taylor. «CRC Handbook of Electrical Filters». In: (1997) (cit. on p. 85).

[106] Rohde Schwarz. «Implementation of Real-Time Spectrum Analysis». In: () (cit. on p. 86).

[107] STMicroelectronics. «STM32 NUCLEO-F303K8 Datasheet». In: () (cit. on p. 92).

[108] Bartels Mikrotechnik. «Operating Manual for the Micropump Driver mp6-QuadOEM». In: () (cit. on p. 92).